In-situ investigation of elemental corrosion reactions during the surface treatment of Al-Cu and Al-Cu-Li alloys.

Oumaïma Gharbi

THÈSE DE DOCTORAT DE
L'UNIVERSITÉ PIERRE ET MARIE CURIE

Ecole doctorale de Chimie Physique et Chimie Analytique de Paris Centre

Institut de Recherche de Chimie de Paris / Interfaces, Electrochimie, Energie

In situ investigation of elemental corrosion reactions during the surface treatment of Al-Cu and Al-Cu-Li alloys.

Présentée par

Oumaïma Gharbi

Pour obtenir le grade de

DOCTEUR DE L'UNIVERSITÉ PIERRE ET MARIE CURIE

Soutenue le 7 Décembre 2016

Devant un jury composé de :

Pr. Christine Blanc : Professeur au CIRIMAT, Toulouse	RAPPORTEUR
Pr. Sannakaisa Virtanen : Professeur à l'Université Friedrich Alexander, Erlangen	RAPPORTEUR
Pr. François Huet : Professeur à l'Université Pierre et Marie Curie	EXAMINATEUR
Dr. Lionel Peguet : Chercheur à Constellium, Voreppe	EXAMINATEUR
Pr. Kevin Ogle : Professeur à l'IRCP Chimie Paristech	DIRECTEUR DE THÈSE

IRCP | Institut de Recherche de Chimie Paris

« الذكي يعرف من اجاباته والحكيم يعرف من اسئلته . »

نجيب محفوظ.

« You can tell whether a man is clever by his answers.

You can tell whether a man is wise by his questions. »

Naguib Mahfouz.

ACKNOWLEDGMENTS

L’écriture des remerciements me semble de loin la partie la plus difficile à mettre en forme, car derrière chaque mot, s’entremêle des souvenirs teintés d’une certaine tristesse à l’idée de clôturer toute l’aventure qu’était cette thèse.

Cette aventure n’aurait pas pu avoir lieu sans mon directeur de thèse, Kevin Ogle, à qui j’adresse mes plus sincères remerciements. Je le remercie pour sa bienveillance, ses conseils avisés et pour m’avoir guidé durant ces trois années. Je le remercie de m’avoir accordé cette liberté qui m’a permis d’explorer plusieurs horizons, qui m’ont amené à faire des rencontres et vivre des expériences enrichissantes intellectuellement et humainement.

Ces trois années ont été ponctuées de rencontres déterminantes, et l’une des première qui me vient à l’esprit est celle de Nick Birbilis. Je tiens à lui exprimer ma plus profonde gratitude, pour le temps qu’il m’a accordé malgré les 15 000 km qui séparent la France de l’Australie. Son énergie, son humour et enthousiasme à toute épreuve ont été à mes yeux une source d’inspiration ; son accueil chaleureux et celui de son équipe en Australie m’ont permis de vivre la meilleure expérience Australienne possible. Un grand merci, surtout pour toutes ces anecdotes et petites histoires auxquelles j’ai eu droit, toutes plus drôles les unes que les autres !

Mes plus vifs remerciements s’adressent aux membres du jury pour tout l’intérêt qu’ils ont porté à mes travaux. Je remercie en premier lieu Mr François Huet, pour m’avoir fait l’honneur de présider mon jury, à Mme Christine Blanc et Mme Sannakaisa Virtanen pour avoir accepté d’être les rapporteurs de mes travaux et enfin Mr Lionel Peguet pour avoir participé au jury en tant qu’examinateur.

Je tiens à remercier Constellium pour m’avoir fourni l’alliage d’aluminium 2024 et pour les discussions enrichissantes sur mon projet.

Au cours de cette thèse, j’ai eu la chance de faire d’innombrable rencontres, qui m’ont fait découvrir les multitudes facettes de la recherche. En l’occurrence, je remercie toute l’équipe des TP, et en premier lieu Peggy et Sebastiana pour leur accueil et gentillesse ; mais aussi Sophie Griveau et Fanny D’Orlyé pour m’avoir formé et fait réaliser à quel point j’ai plaisir à faire de l’enseignement. Une pensée pour les autres enseignants : FX, Caroline, Stéphane, Barbara, Olivier…

Comment évoquer ces trois années sans parler de l’équipe I2E ! Une équipe, qui s’apparente à mes yeux plus à une famille, débordante de vie et de convivialité. Je remercie Michel Cassir, pour son accueil et son humanité et pour avoir prodigué un environnement propice aux échanges, au partage et à l’enrichissement personnel et intellectuel. Coté administration, je remercie Elisabeth Brochet et Marjorie Sadaoui pour l’aide administrative, leur efficacité et pour leur capacité à toujours trouver une solution malgré les multitudes d’imprévus que j’ai pu rencontrer. Mes remerciements s’adressent aussi à Polina Volovitch pour sa disponibilité. Coté administration, je remercie Isabelle Duc, Roxanne Hervé, Guy Bichet, Patrick Guezo, Ali et Francine pour leur implication (dans les pots !!), les dépannages du vendredi soir et du samedi matin, et les raclettes et autres déjeuners partagés ensemble.

Je remercie Valérie Albin et Virginie Lair pour les discussions, et les innombrables déjeuner où mon régime alimentaire (de moineau) a été disséqué, et commenté allègrement… ! Je pense que maintenant mon prénom est associé au Quinoa et aux Makrouds (n'est-ce pas Virginie… !)

Comment ne pas remercier Marie-Hélène Chavanne, pour ses blagues improbables (j'en rigole encore !), ses boites de thon, ses Actimels et soupe Royco mais surtout pour avoir été aussi présente et encourageante tout au long de ma fin de thèse. Tu as toujours su trouver les mots pour mettre du baume au cœur et me faire relativiser. Merci !!!

Cette fin de thèse fut sans aucun doute un des plus grands défis personnel et professionnel que j'ai eu à relever. Le chemin vers la fin a été plus difficile que prévu, et la présence d'Armelle Ringuedé m'a maintenu sur les rails et m'a aidé à terminer ce projet en temps et en heure. Je la remercie pour le tout le temps qu'elle m'a accordé, pour son implication et pour m'avoir autant soutenu durant ma dernière année de thèse. Ce fut un vrai plaisir de travailler avec toi. Ta spontanéité (y'a encore du travail hein), nos conversations intellectuelles (le mystère des maisons sans murs n'est toujours pas élucidé), ton soutien et ton honnêteté ont été déterminant et m'ont permis de te connaître et de partager les plus gros fous rires qui font partie de mes meilleurs souvenirs de thèse (et RIP à toutes ces clémentines qu'on a englouti).

Au tour de mes compatriotes les doc, post-doc, stagiaires et autres rencontres, parfois brèves, mais qui jonchent ma mémoire d'anecdotes croustillantes, drôle (parfois moins drôles) et de beaux souvenirs. Je remercie les doctorants du PCS et MS : Marion pour ses sourires et sa douceur, Rémi pour partager la même passion des chats, Shadi, Zuzana, Emna pour les afterworks partagé ensemble ainsi que Stéphanie Delannoy et Cedrik Brozek pour leur gentillesse et le temps passé avec moi sur mes échantillons.

Je remercie Slava pour son aide et pour m'avoir présenté à « Mme ICP » comme il l'aime l'appeler, et m'avoir appris quelques phrases en Russes (pas assez pour survivre en Russie non plus). Je remercie Arturo Melendez alias « McGyver » pour ses réponses à tout, mais surtout pour son délicieux guacamole et pour avoir supporté mes danses incongrues d'après 18h. Je tiens à remercier Noémie Ott pour son aide durant ma première année de thèse et pour toute les suggestions qu'elle a pu faire sur mon montage expérimental.

Combien de fois ai-je ri, débattu et partagé de moments avec Amandine Calmet (Reine des Neiges, Rene des Doctorant, Reine du Drame), Dorra Dallel (avec ses bon petit plats et son humour décapant), Aziz Nechache (le Tanguy du labo), François Lebreau (alias Fanfan l'encyclopédie Larousse/Robert, ne crois pas que je vais laisser passer l'histoire du T-Shirt…), Junsoo Han (le plus drôle des Coréens !), Andrey Grishin (je garderai tes nettoyages frénétiques en mémoire, à se dire que tu pourrais presque te nettoyer à l'eau de javel), Manel Ben Osman alias Mme la Perchée (merci pour ton aide précieuse et tes encouragements, tu es perchée certes, mais tu es la meilleure des perchées !) et Amandine Michot Mignucci (magle, la tata Loza, l'Arabe refoulée que j'ai adoré détester).

Je remercie les stagiaires et autre doctorants, Chloé Alamah, Peng Zhu, Alina Maltseva, Thomas Sanchez, Nour, Karima, Moussa, Cyril Nicard et Perrine Tanguy pour l'aide et leur gentillesse, mais aussi Bradley Da Silva, Olivier Lesage pour les encouragements.

Je remercie mes amis, qui pour certains m'ont encouragé et d'autres m'ont inspiré à suivre ce parcours pour lequel au départ je ne m'étais pas destinée. Une pensée pour Magali Quinet qui m'a ouvert les portes du monde de l'électrochimie et de la corrosion (une vraie révélation !!), André Ouwanssi (Dédé le Toulousain Camerounais de Bretagne), Isabel Arroyo et Mary Shaffer. Je remercie infiniment la famille Hachaïchi et la famille Hasnaoui pour le soutien, leur présence et leur implication dans mon parcours.

Une pensée à ceux chez qui j'ai toujours pu retrouver du réconfort, mes deux petits chats Soussou et Tigrou qui, avec toute leur innocence et leur nonchalance qui caractérisent si bien les chats, m'ont permis de me réfugier dans un monde d'insouciance, de ronron et de douceur le temps de quelques minutes (oui oui, j'ai bien remercié mes chats).

Mes remerciements les plus profonds s'adressent à ma famille sans qui rien de tout ceci n'aurait pu arriver. Je remercie mes deux petits (petit d'âge mais pas de taille) frères, Bassem et Yousri, pour leur amour et humour vache, et leur soutien. Je suis très fière de ce que vous êtes devenus. Je remercie du fond du cœur mes parents, à qui je dédie cette thèse. Bien que la vie n'ait pas été toujours très clémente à votre égard, vous n'avez jamais cessé d'irradier le foyer d'amour et vous m'avez toujours été d'un soutien indéfectible. Je suis très fière de vous avoir comme parents et sachez que je vous admire pour votre force, votre patience et votre générosité.

TABLE OF CONTENTS

LIST OF ACRONYMS & SYMBOLS

AESEC: Atomic emission spectroelectrochemistry

LDR: Linear dynamic range

ICP-AES: Inductively coupled plasma atomic emission spectrometer

ICP-MS: Inductively coupled plasma mass spectrometer

OCP: Open circuit potential

ORR: Oxygen reduction reaction

GRSL: Grain refined surface layer

GP: Guinier Preston zone

IGC: Intergranular corrosion

SCC: Stress corrosion cracking

SHT: Solution heat treated

PFZ: Precipitate free zone

SSSS: Super saturated solid solution

RDE: Rotating disk electrode

RBS: Rutherford backscattered

SEM: Scanning electron microscopy

EDXS: Energy dispersive X-ray spectroscopy

FIB: Focused ion beam

TEM: Transmission electron microscopy

GDOES: Glow discharge optical emission spectrometer

XRD: X-ray diffraction

XPS: X-ray photoelectron spectroscopy

ATR-IR: Attenuated total reflectance infrared spectrometer

WE: Working electrode

RE: Reference electrode

CE: Counter electrode

FIV: Flow injection valve

SHT: Solution heat treated

LDH: Layered double hydroxide

A: Surface area of the working electrode

C_M: Concentration of dissolved elements

V_M: Dissolution rate of dissolved metal

n: Number of electron(s)

M: Molar mass of atom

t: Time

F: Faraday's constant

c: speed of light

h: Max Planck's constant h = 3.336 x 10^{-11} s cm^{-1}

k: Boltzmann's constant

h(t): transfer function or residence time distribution

$\beta \; and \; \tau$: parameters of the transfer function h(t)

λ: wavelength

$C_{2\sigma}$: detection limit

Q_M^{ins}: Quantity of insoluble species

j_e: Total current measured by the potentiostat

j_a: Anodic current

j_c: Cathodic current

v_M: Dissolution rate

C_M: Concentration

LIST OF FIGURES & TABLES

CHAPTER I: INTRODUCTION & STATE OF THE ART

« إذا كنت تدرى فتلك مصيبة وإن كنت لا تدرى فالمصيبة أعظم. »

بهاء الدين الإخميمى.

"If you know then it is a disaster, and if you don't know then it is a greater disaster."

Baha El-Din Al-Ikhmaymi.

1. INTRODUCTION

Aluminum is a light, silvery-white metal and mostly the third most abundant metal in the Earth's crust. It is also one of the most common elements in use today, but it has not always been the case. Etymologically, alumina (and by extension aluminum) comes from the Latin word "alumen", term used to designate potassium alum $KAl(SO_4)_2.12H_2O$ during the Roman times.

In 1821, Pierre Berthier discovered aluminum ore, called bauxite because he found it near the village of Les-Beaux-de-Provence in southern France. It was not only in 1854 that pure aluminum was successfully extracted by a French chemist, Henri Saint-Claire Deville who saw the potential and the future impact of this metal in our daily life.

Alumina is considered to be one of the most stable oxides and its reduction to produce pure aluminum (Al) is very difficult (ΔG = -1582 kJ mol^{-1}). Throughout much of the 19th century, aluminum was considered as a very precious metal, as pure aluminum metal was harder to extract from nature than gold or silver. The first kilogram of aluminum manufactured in 1856 was more expensive than silver. As indication of its value, the Emperor Napoleon III had a special aluminum set for his important guests and in 1858, his infant was offered a rattle made of aluminum.

Following the development of cost effective production processes, in less than a century aluminum became one of the most popular structural materials in the world. Today it is used in diverse range of applications in the automobile, construction and packaging industries. In the recent decades, aluminum alloys such as AA2024-T3 (Al-Cu-Mg) have been used in aerospace application for their excellent strength-to-weight ratio. The recent emphasis on developing lighter structures suggest that Al use will increase in the future.

The difficulty with Al is the optimization of mechanical properties with corrosion resistance. It is well-known that the alloying elements control the microstructure, and enhance remarkably the mechanical properties. However, they also lead to a highly heterogeneous surface chemistry leading to a decrease in corrosion resistance. One way to overcome this problem is to protect the aluminum alloy surface by coatings; the most efficient ones are Cr^{VI} based coatings. However, Cr^{VI} based formulations for surface treatments are CMR (carcinogenic, mutagenic, reprotoxic) and they have to be progressively removed from the market. Consequently, the focus of research has shifted to finding different alternatives to supersede Cr^{VI}. To date, no suitable candidates has been found.

Surface treatments were extensively studied through a large variety of *ex situ* characterization methods, in view of developing and studying new processes and formulations. The literature describes the use of various techniques such as the scanning electron microscopy, X-ray photoelectron spectroscopy, weight loss measurements or ICP (Inductively coupled plasma) analysis of electrolyte baths to routinely monitor and assess the effectiveness of the surface treatment. It is commonly accepted that parameters such as surface topography, chemical distribution of the alloy, selective dissolution or dissolution rate ("etch rate") determine the efficacy of the surface treatment. Obviously, the ultimate goal of these

characterization techniques is to be able to determine accurately the reactivity of very complex microstructure during the course of the surface treatment. Ideally, this knowledge should help tailoring new Cr^{VI} free formulations that will ensure excellent corrosion protection. In this context, the AESEC (atomic emission spectroelectrochemistry) would correspond to the ideal analytical tool for the *in situ* analysis of Al alloys reactivity in nearly industrial conditions. This method can give access to quantitative analysis of elemental dissolution rates at open circuit conditions. In addition, it can provide accurate measurement of etch rate, dissolution kinetics for about 30 elements or follow selective dissolution and enrichment mechanisms in real time. This is one of the specific interests of AESEC compared to the *ex situ* techniques mentioned above. Furthermore, AESEC contribution could be extended to the study of new formulations or alloys and give significant insights pertaining to the mechanisms involved during these surface treatments processes.

The first part of this research was focused on the development of this methodology for our specific application. The AA2024 alloy has been extensively studied in a similar context and it therefore seemed to be the best reference for the optimization and the validation of our methodology, along with the modifications of our analytic procedure. The use of this combination provided answers about the reactivity of the alloy during an industrial pretreatment sequence. It furthermore enabled the determination of dissolution kinetic, the specific observation of the detachment of intermetallic particles and the selective dissolution mechanism in real time. This methodology could be used on a daily basis as a powerful characterization tool. In the long term, this would help to tailor formulations as a function of the substrate and accelerate the development of more environmental friendly coatings.

In a second part, this study was expanded to include the new Aluminum – Copper – Lithium alloy AA2050. Lithium addition proved to be beneficial, as it improves weight reduction and enhances the mechanical properties. However, because it is very light, Li is very difficult to analyze with most of the usual characterization techniques. As a result, unlike the AA2024, no information exists about Li reactivity during surface treatment or about the underlying mechanims. This methodology appears to be the only one that can provide information about the behavior of Li during a complete surface treatment sequence.

This PhD dissertation is organized into 5 chapters:

- Chapter I gives a literature review of Al alloys: their manufacture, corrosion susceptibility, general microstructure, with a specific focus on the 2XXX series, AA2024 and AA2050 which are the two alloys studied within the scope of this research project.

Chapter II to V will cover in details the results of the dissertation, and each chapter will be presented as a standalone paper, as the majority is or will be published individually.

- Chapter II will present the main methodology used during this PhD and its development, the experimental procedure and the materials studied.

- Chapter III will be devoted to the presentation of the results on the AA2024-T3 alloy, allowing us to optimize and validate our approach.
- Chapter IV will focus on the new Al-Li AA2050-T3 alloy and present the results dealing with the *in situ* analysis of the corrosion product
- Chapter V will be devoted to the surface characterization of the AA2050-T3 after pretreatment and potentiodynamic polarization, in order to provide new data in terms of corrosion product formation mechanisms and its structure.
- The preliminary studies and conclusion part will summarize the different results and give the perspectives of this thesis. In addition, some preliminary results on the reactivity of single phases illustrated by the S-phase, and an introduction to the use of statistics applied to the particle detachment during the pretreatment will be given.

2. STATE OF THE ART

2.1. Generalities on Aluminum

Aluminum consumption has constantly increased since the 19th century and has become the second most used metal just behind steel. It is widely used for automotive, aerospace, packaging but also building and construction applications. The main benefits of using Al are its low volumetric mass density (2.7 g cm^{-3}), low thermal conductivity (equivalent to 60 % of copper thermal conductivity), and its good corrosion resistance [1]. Moreover, Al is easily recyclable which is a very important factor in the context of recycle friendly politics.

The Pourbaix diagram of Al in water at 25°C is given in **Fig. 1**. [2] This diagram gives an overview of the thermodynamic stability of Al as a function of potential and pH. This diagram shows that the corrosion of Al is pH - dependent as in acidic and alkaline media (below pH 4 and above 8), a general dissolution of Al will occur to form Al(III) species and generate hydrogen during the reaction:

$$Al + 3H^+ \rightarrow Al^{3+} + {}^3/_2\ H_2 \qquad \text{(Acid)} \qquad (1)$$

$$Al + H_2O + OH^- \rightarrow AlO_2^- + {}^3/_2\, H_2 \qquad \text{(Alkaline)} \qquad (2)$$

Between these two ranges, Al appears to be kinetically stable by forming a thin film of $Al_2O_3.nH_2O$ approximately 1 nm thick which protects the metal by forming a barrier between it and the environment. The immunity however is not accessible at potentials below 9, as at this domain, water is no longer stable. The nature of the protective oxide film varies according to the temperature, pH of the electrolyte and immersion time. When Al is exposed to nearly boiling water, relatively thick and amorphous barrier oxide layer, called boehmite can form ($Al_2O_3.H_2O\ \gamma$). At lower temperature however, the bayerite form is predominant aluminum trihydroxide ($Al(OH)_3$) but other forms of Al oxides can form such as gibbsite $Al(OH)_3$ or hydrargilite ($Al_2O_3.3H_2O$) during the aging of boehmite [2].

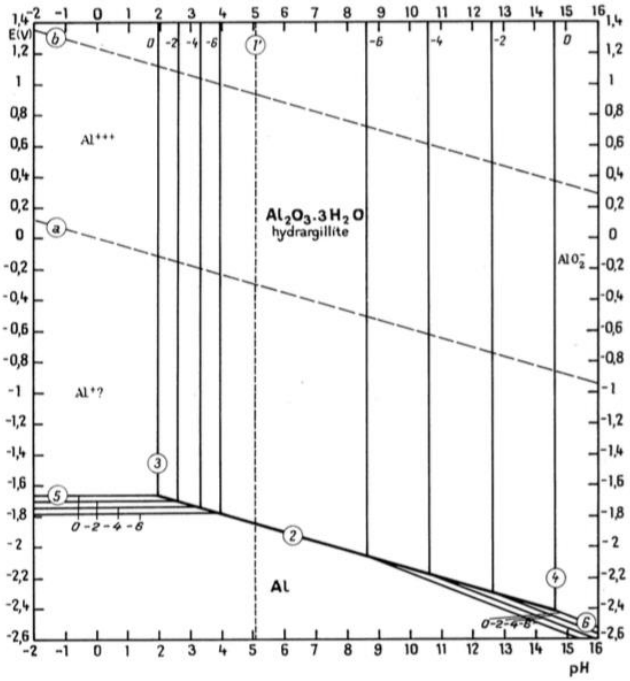

Fig. 1. — Diagramme d'équilibres tension-pH du système aluminium-eau, à 25°C.

Figure 1: Pourbaix diagram of Aluminum in water at 25°C [2].

However, pure Al does not meet the mechanical properties requirements of the market (transport, civil engineering, heat exchangers…[1]), and has to be alloyed with different elements such as copper, magnesium, zinc, lithium or manganese. An International Alloying Designation System was introduced in the 1970s allowing the distinction between alloy series to facilitate their identification between the countries. This designation provides to each alloy a four number series, as the first number refers to the main alloying element present. They have been divided from the AA1XXX series to the AA8XXX series. **Table 1** gives the specifications of the different series relative to Aluminum alloys [3][4].

Table 1: Specifications of the different Aluminum Alloy series reported in the literature.

Series	*Main alloying elements present in the alloy*
1XXX	Pure Al (99.9%) Al
2XXX	Al-Cu, Al-Cu-Mg and Al-Cu-Li alloys
3XXX	Al-Mn and Al-Mn-Mg alloys
4XXX	Al-Si alloys
5XXX	Al-Mg alloys
6XXX	Al-Mg-Si alloys
7XXX	Al-Zn-Mg and Al-Zn-Mg-Cu alloys
8XXX	Other(s)

2.2. Age hardening and thermal treatment.

The age hardening takes a fundamental place in the alloy processing as it defines the microstructure and influence the mechanical and corrosion properties of the alloy. Of all the wrought alloys presented above, only the 2XXX, 6XXX and 7XXX series are heat treatable [5]. These alloys are designed by a letter T and a number which corresponds to specific heat treatment conditions. This designation follows the 4 number series attributed to each alloy. On the other hand, 1XXX, 3XXX, 4XXX and 5XXX are non-heat treatable and their mechanical properties are associated with strain hardening. They are usually alloyed with zinc, iron, chromium or magnesium whereas heat treatable alloys contain higher concentration of copper. Their mechanical properties increase with phase precipitation during the heat treatment. Generally, the age hardening is defined by three steps [6]:

- The solution treatment, generally at 460 - 565°C, where the soluble alloying elements are dissolved in the Aluminum solution.
- The quenching, where the solution is rapidly cooled -usually at room temperature- to obtain a supersaturated solid solution (SSSS) of the alloying element in the Aluminum matrix.
- An age hardening to form from the SSSS the fine precipitates in the Aluminum matrix. The aging parameters (time and temperature) will have an impact on the precipitates size and distribution. Usually the aging temperature is between 115-195°C.

The mechanical properties of the 2XXX series Al alloys are determined by the thermomechanical treatment. Usually, the alloying elements form clusters coherent with the matrix, called Guinier-Preston (GP) zones. These zones are ordered, and they are only one or two atoms planes in thickness. As they grow with temperature and time in the α(Al) solid solution phase, they become incoherent with the lattice. In the case of the Al-Cu phase diagram, the formation of the θ phase (Al_2Cu) follows this precipitation sequence:

$$\alpha_{SSSS} \rightarrow GP\ zone \rightarrow \theta'' \rightarrow \theta' \rightarrow \theta(Al_2Cu) \quad (3)$$

On the other hand, the nucleation of Al-Cu-Mg precipitates is determined by the Al-Cu-Mg ternary diagram:

$$\alpha_{SSSS} \rightarrow GP(Cu, Mg)\ zone \rightarrow S'' \rightarrow S' \rightarrow S(Al_2CuMg) \quad (4)$$

The copper in solid solution will segregate as clusters and then precipitate as GP zones to form very rapidly as rods along the $< 100 >_\alpha$ direction. This is followed by the formation of the S' precipitates as laths in $\{210\}_\alpha$ planes along $< 001 >_\alpha$ direction. They are semi-coherent and nucleated at dislocations. **Fig. 2** represents a section of the ternary Al-Cu-Mg phase diagram at 460°C and 190°C [6].

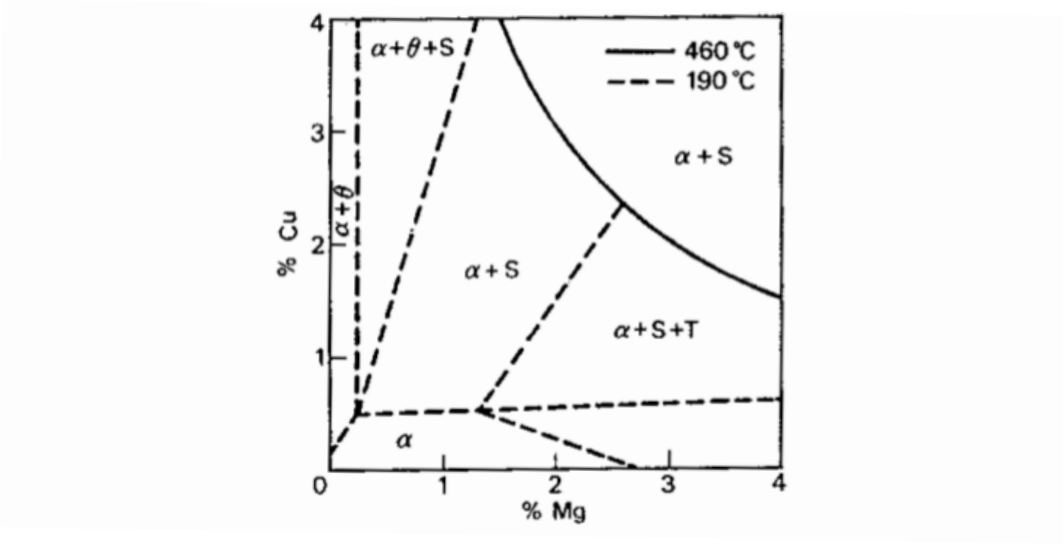

Figure 2: Section of ternary Al-Cu-Mg phase diagram at 460°C and 190°C (estimated). θ= Al_2Cu, S= Al_2CuMg, T= Al_6CuMg_4

2.3. Aluminum 2024-T3: microstructure

In the past few years, alloy development has been continuously progressing to meet the requirements of the aircraft industry. Al-Cu alloys also referred as the 2000 series aluminum alloys are widely used as they provide an excellent strength to weight ratio, high damage tolerance and fatigue resistance. In the case of the AA2024-T3, an aluminum-copper-magnesium alloy, the addition of Cu and Mg considerably increases the mechanical properties. The enhanced mechanical properties are the consequence of the alloying elements addition with the effect of a heat treatment which allows the control of the alloy features without affecting its weight. **Table 2** gives the general composition of the AA2024-T3 used for this study.

Table 2: Chemical composition of AA2024-T3 used during this PhD (wt %)

2024-T3	*Al*	*Cu*	*Mg*	*Mn*	*Fe*	*Si*	*Zn*	*Ti*	*Cr*	*Ni*	*Zr*
wt %	bal	4.21	1.38	0.48	0.13	0.066	0.12	0.023	0.0051	0.0059	0.0138

The heat treatment takes a fundamental place during the alloy manufacture, as the mechanical properties improve with the precipitation of the alloying elements into intermetallic compounds [5]. Recently, Boa et al. reported that these intermetallic particles represent approximately 2.83 % of the total surface [7]. The literature refers to three categories of intermetallic particles which exhibit specific characteristics. *Hardening precipitates* start by clustering in the matrix and the grain boundaries from the solid solution as a called Guinier-Preston zone and they grow by segregation as a function of the temperature and aging time. Their sizes usually vary between 50 nm and few microns and they participate to the

mechanical properties. In the case of the 2000 series Aluminum alloys, the S phase-Al_2CuMg- or the θ phase- Al_2Cu- are examples of hardening precipitates, furthermore as needles or rods [8].

Dispersoids are the finest intermetallic particles as their sizes do not exceed 500 nm. They form during the homogenization of the ingot by solid state precipitation. Their main role is to prevent the recrystallization process and to control grain growth. They are highly insoluble, as once formed, they are not affected by age hardening and they are usually associated with Titanium, Zirconium, Manganese or Chromium. For example, $Al_{12}Mn_3Si$, Al_3Zr, Al_3Ti or $Al_{20}Cu_2Mn_3$ typical dispersoids are found in Al-alloys [3,6].

Constituent particles (also called coarse intermetallic compounds) are the largest intermetallic particles and they generally do not affect the mechanical properties. One group, usually formed from impurities, is present in the solid solution during the solidification of the initial ingot and they generally do not respond to the heat treatment process. Common constituent particles reported in the literature of this group are Al_7Cu_2Fe, $Al_6(Fe,Mn)$ or $Al_{12}(Fe,Mn)_3Si$ [6,7]. The second group however, also called soluble constituent particles, are composed of the main alloying elements and Al_2Cu, Al_2CuMg or Mg_2Si are typical examples and can be dissolved during the ingot homogenization [6]. The Al-Cu-Fe-Mn-(Si) particles are irregularly shaped [9], they possess a high hardness [10] and their average size is between 1 to 20 µm. However, their size is considerably reduced (0.5 to 10 µm) during the fabrication of cast ingot where they are fractured and become aligned. **Table 3** gives a list of most of the intermetallic particles and their characteristics in 2000 series Al alloys.

Table 3: List of the intermetallic particles found in 2XXX series Al alloys reported in the literature.

Name and stoichiometry	*Size*	*Characteristics and role*
S-phase Al_2CuMg	50 nm to 5 µm spherical [9]	Hardening precipitate or Constituent particle
θ phase Al_2Cu	~ 1 µm	Hardening precipitate
Al_7Cu_2Fe *Al_3Fe* *Al-Cu-Mn-Fe-Si* *Al_6Mn* *ß phase Mg_2Si*	~5-20 µm Large and irregularly shaped [9]	Constituent particle Do not participate to the mechanical properties Detrimental effect on the corrosion resistance [6].
Al_3Zr	0.05 to 0.5 µm	Dispersoid Control grain growth Retard recrystallization [6]
$Al_{20}Mn_3Cu_2$	Rod shape, ~ 100 nm [3,8]	

2.4. Alloy processing and effect of rolling on the surface microstructure

During alloy processing, the final step consists in a mechanical shaping of the alloy to achieve a semi-fabricated form [6]. The ingot passes through two sets of steel or copper rolls that rotate in opposite directions. As a consequence, the slab undergoes a severe deformation reducing its thickness to usually 16-20 mm and up to 1800 mm in width [6,11]. This process, causes a considerable modification to surface and generates a new surface layer, induced by the breakdown of the intermetallic particles, their coverage by an aluminum oxide layer and their redistribution on the surface. This phenomenon has been mentioned in the 1980s and is increasingly studied in the context of corrosion susceptibility and surface treatment of Aluminum alloys. The rolling process will create a new surface layer approximately 3 to 5 µm thick, characterized by a high porosity, fine grain structure [12] and incorporated oxides including γ-Al_2O_3 and MgO [13] (**Fig. 3**). The mechanism of the surface modification reported by Fishkis et al. [13] involves three steps:

- Formations of surface depressions by plowing, adhesive wear, delamination wear or transverse surface cracking,
- Filling of the cavities with wear debris which include oxide, metal and lubricants,
- Coverage of the cavities with a thin metal layer during the rolling process creating a "shingled" surface appearance.

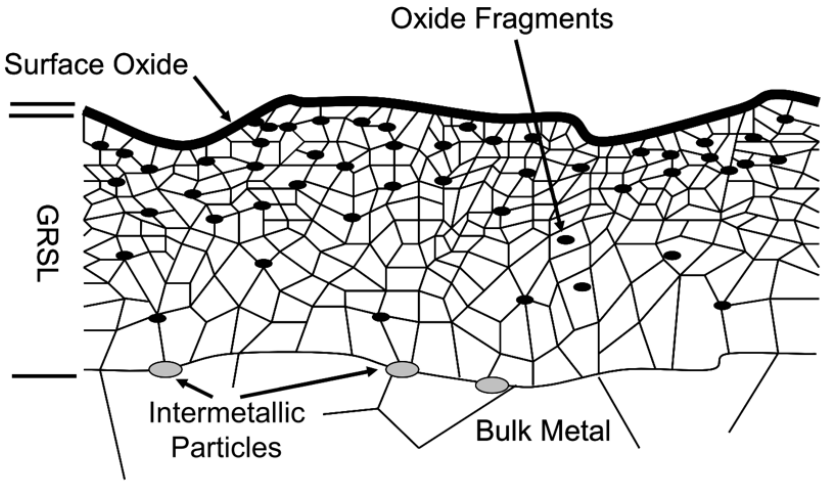

Figure 3: Schematic of the modified structure called Grain Refined Surface Layer (GRSL) resulting from mechanical processing. This zone is characterized by the presence of oxide particulates and a recrystallized structure [14].

This modified surface layer was defined by Leth-Olsen as the Grain Refine Surface Layer (GRSL); its composition depends on the alloy [15].

Previous studies mentioned an alteration on the particles distribution and reported an increase of the intermetallic particles (Al-Cu and Al-Cu-Mn-Fe) density on the alloy surface after the rolling process [7], accompanied with decrease of their sizes by approximately one third. Moreover, Lunder and

Nisancioglu [16] reported that after rolling, the constituent particles were covered by the Aluminum matrix.

However, alloying elements enrichment can also be explained by other theories. Indeed, it has been shown by Textor and Amstutz that elements such as magnesium, lithium or silicon segregate readily to the alloy surface [17]. This surface enrichment was determined by two major mechanisms: a) bulk diffusion which can occur during the heat treatment process and b) grain boundary segregation process [17].

In summary, the complexity of the Al alloy surface and its singular microstructure reveal that parameters such as mechanical processing, storage environment or alloy composition need to be controlled and must be taken into account when considering the application of a surface treatment to the alloy.

2.5. The corrosion behavior of AA2024-T3

The electrochemical reactivity of AA2024-T3 is controlled by the highly heterogeneous microstructure, and more precisely by the second phase particles as they exhibit a different electrochemical behavior regarding the aluminum matrix [18–24]. It has been shown that Cu as well as the impurities are the main cause of corrosion failure as they create local sites where a micro-galvanic coupling between the particle and the matrix occurs [8,9,25–28]. Over the years, the reactivity of AA2024-T3 has been extensively studied to understand the mechanisms and determine the factors involved during the corrosion process. In this chapter, only the most common corrosion mechanisms along with the contribution of different intermetallic particles will be presented.

2.5.1. The pitting corrosion of Aluminum

Pitting is considered to be the most common mechanism of corrosion propagation for pure aluminum and high strength Al-alloys. The different steps involved during the pitting process were extensively studied and reported in the literature [29–34] **(Fig. 4**.): a) the film breakdown b) metastable pitting c) pit growth and d) pit stifling or death. The pit initiation - propagation is also facilitated by the presence of halides such as chloride ions in solution. These ions are very-well known to be aggressive to aluminum oxide as they will adsorb at the surface of the oxide film. Then adsorption of Cl^- on the oxide occurs, preferentially localized on the irregularities of the film.

Secondly, the Cl^- ions migrate through the film, creating a defect which exposes the bare metal to the solution. This will induce a pit propagation through the metal, nevertheless, a majority of the pits will not propagate and rapidly passivate. Those pits which initiate and grow only for a limited period before being passivated are called metastable pits. Indeed, the growth and propagation of pit requires very specific conditions such as local acidification and a high chloride concentration which is not always the case. At the bottom, the pit initiation is determined by the Aluminum oxidation and water hydrolysis:

$$Al \rightarrow Al^{3+} + 3e^- \quad (5)$$

$$Al^{3+} + H_2O \rightarrow Al(OH)^{2+} + H^+ \quad (6)$$

followed by chloride hydrolysis:

$$Al(OH)^{2+} + Cl^- \rightarrow Al(OH)Cl^+ \quad (7)$$

$$Al(OH)Cl^+ + H_2O \rightarrow Al(OH)_2Cl + H^+ \quad (8)$$

where this reaction will generate a net gain of H^+ ion, involving a pH decrease.

On the other hand, on the surface, the cathodic reactions will take place with the oxygen and water reduction reactions. As a consequence, a decrease of the pH will occur leading to the dissolution of the Al matrix:

$$H_2O + e^- \rightarrow OH^- + {}^1/_2\, H_2 \quad (9)$$

$$O_2 + 2H_2O + 4e^- \rightarrow 4OH^- \quad (10)$$

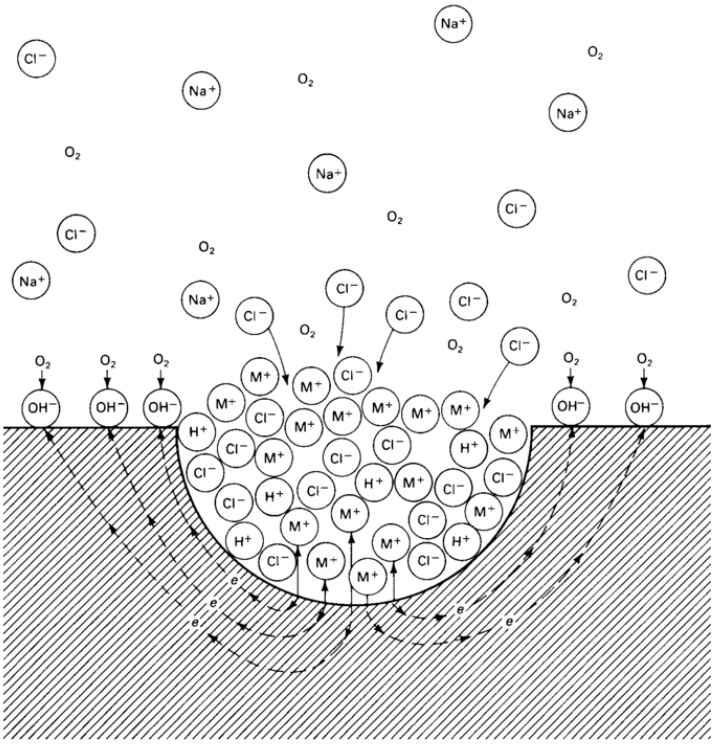

Figure 4: Autocatalytic process occurring during the propagation of a pit in aerated NaCl solution. The metal M undergoes active dissolution at the bottom of the pit, while oxygen reduction takes place at the surface [35].

Several studies focused on the effect of the intermetallic particles on the pitting corrosion behavior of Al-Cu alloys. For example, Buchheit and more recently Birbilis and Buchheit collected the electrochemical potential of various intermetallic particles in chloride containing solutions [18,19,36]

(**Table 4**) as an attempt to predict their electrochemical behavior regarding to the matrix. Depending on the intermetallic composition, the particle can act anodically or cathodically with respect to the matrix and affect the pit initiation or morphology [37]. For example, particles such as Al_2Cu, Al_7Cu_2Fe or Al_3Fe act as cathodic site and promote the pit initiation at the periphery of the particle [9,38–41]. In such case, the attack is mainly localized on the matrix leaving the particle non attacked as reported by several researchers [42,43]. However, if the particle is active, this may cause selective dissolution, also reported as a dealloying effect. In this case, the pits are found to be in the particle and are in this case usually deeper.

Table 4 : Corrosion potential of various intermetallic phases reported in the literature.

Phase	*E_{SCE} (V)*	*Environment*	*Aeration*
Al_2Cu	-0.7	0.5 M NaCl	Air [19]
	-0.695	0.6M NaCl	Not stated [18]
Al_7Cu_2Fe	-0.654	0.6 M NaCl	Not stated [18]
Al_3Fe	-0.910	0.5 M NaCl	N_2 [19]
	-0.566	0.6 M NaCl	Not stated [18]
Al_2CuMg	-0.920	0.5 M NaCl	Ar [19]
	-1.061	0.6 M NaCl	Not stated [18]
Al_3Zr	-0.625	0.5 M NaCl	N_2 [19]
	-0.801	0.5 M NaCl	Not stated [18]
Al_6Mn	-0.913	0.6 M NaCl	Not stated [18]
Al_2CuLi	-1.096	0.6 M NaCl	Air [19]
$Al_{20}Cu_2Mn_3$	-0.617	0.6 M NaCl	Not stated [18]

2.5.2. Intergranular corrosion

The intergranular corrosion propagates along the grain boundaries and can rapidly propagate into the bulk material. As a consequence, the mechanical properties can be seriously affected by the formation of cracks that could, in long term, cause the breakdown of the material. The intergranular corrosion behavior is systematically related to the distribution of Cu in the solid solution. This is usually caused by the heat treatment, which promotes the precipitation of Cu-rich phases such as Al_2Cu along the grain boundaries, subsequently creating a favorable environment for a galvanic coupling between the matrix and the grain boundary. Several studies highlighted the link between pitting corrosion and intergranular corrosion: Zhang and Frankel [44] showed for AA2024-T3 during potentiodynamic polarization, the presence of two breakdown potentials corresponding respectively to the S-phase dissolution and the initiation/propagation of intergranular corrosion. These two breakdown potentials were previously reported by Galvele et Micheli and Guillaumin and Mankowski [8] for high Al-Cu alloys. Galvele and Micheli [45] attributed the first breakdown to the dissolution of Cu-depleted zone and the second to the

pitting of grain bodies shown in **Fig. 5** (this mechanism will be described in details later). On the other hand, Guillaumin and Mankowski suggested that the first breakdown was caused by the dissolution of the anodic S phase and the second to the precipitate free zone around the particles.

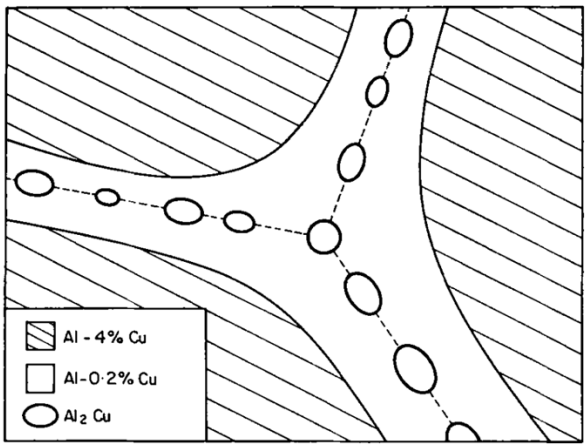

Figure 5: Representation of a grain boundary zone where the θ phase is found at the grain boundaries, surrounded by a Cu-depleted zone and the α-Al matrix [45].

2.5.3. The effect of the S-phase particle (Al_2CuMg)

The S phase is a particle specific to Al-Cu-Mg containing alloy and they represent approximately 60 % of the intermetallic surface area [46]. This particle exhibits a significantly less noble potential regarding the aluminum matrix and undergoes active dissolution [23,24,46]. Most of the time, pits initiate at the periphery and on the particle. Many tried to understand the corrosion mechanisms involved with the S-phase and its effect on the corrosion of surface finishing. Several theories were discussed in the literature, for example, Buchheit suggested a corrosion process through dealloying (**Fig. 6**). First, Buchheit, Guillaumin and Mankowski detailed that the magnesium contained in the particle will dissolve, leaving a typical sponge-like shape on the surface [8,47]. The Cu left on the surface will lead to an increase of the particle potential. This Cu rich sponge will then act as a cathode and generate the dissolution of the surrounding matrix showed by characteristic trenches around the particles. Contrastingly, other studies observed the presence of Copper deposits at the periphery of the particles and presented a different mechanism. Buchheit et al. suggested that during the dealloying of the S-phase particle, some Cu-rich clusters will be transported in the solution through a non-faradaic process [47–50]. The metallic copper, which is no longer in electrical contact with the matrix, will be oxidized by the oxygen present in solution and precipitate as copper oxide. In summary, the major difference between these two theories is that one dissolution mechanism is only driven by a galvanic coupling switch between the particle and the matrix, and the second however, involves a particle detachment/redeposition process. The role and the importance of the S-phase in the Cu enrichment and redistribution process has been also highlighted by the work of Vukmirovic et al. [51], who

demonstrated a significant increase of Cu by comparing a commercial AA2024 and a synthetic AA2024 after 0.5 M NaCl exposure.

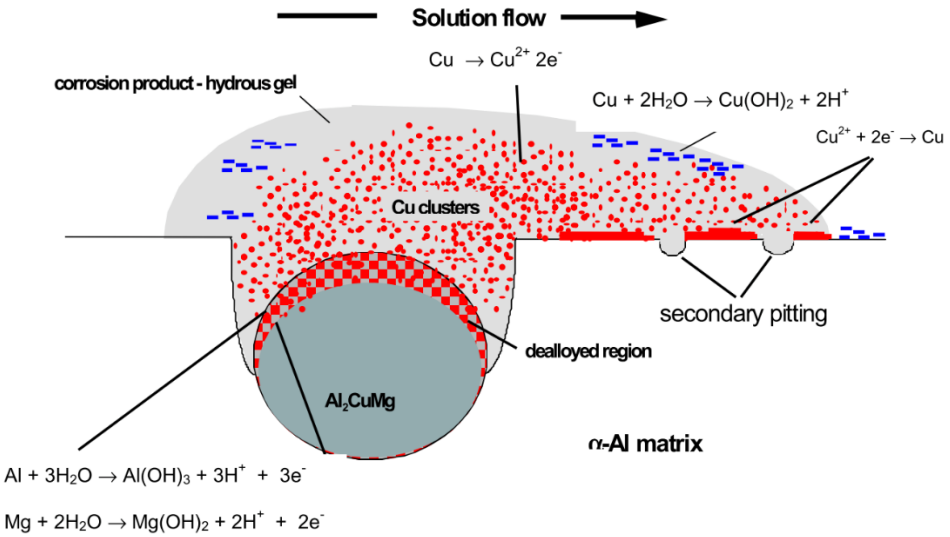

Figure 6: Dealloying process of a S-phase particle. Al and Mg dissolve and form a hydrous gel around the particle. As a result, Cu clusters detach from the intermetallic and are oxidized. They may be redeposited at the periphery of the particle [47].

On the contrary, Zhu et Van Ooij [52] presented a mechanism involving a pH increase at the periphery of the S-phase as a result of the oxygen reduction reaction. When the S-phase is exposed to the solution, the selective dissolution of the magnesium and aluminum contained in the particle will occur. As the particle undergoes dealloying, the copper content will increase, leading to an increase of the cathodic surface area which promotes the formation of a significant amount of hydroxyl ions, generated by oxygen and water reductions. Once the pH of the environment surrounding the particle reaches a value above 9, the aluminum in contact with the particle may dissolve. Consequently, in the opposite to the other mechanism, the dissolution of the matrix is not a result of the galvanic switch occurring between the particle and the matrix but is induced by a local alkalization caused by oxygen and water reduction (**Fig. 7**).

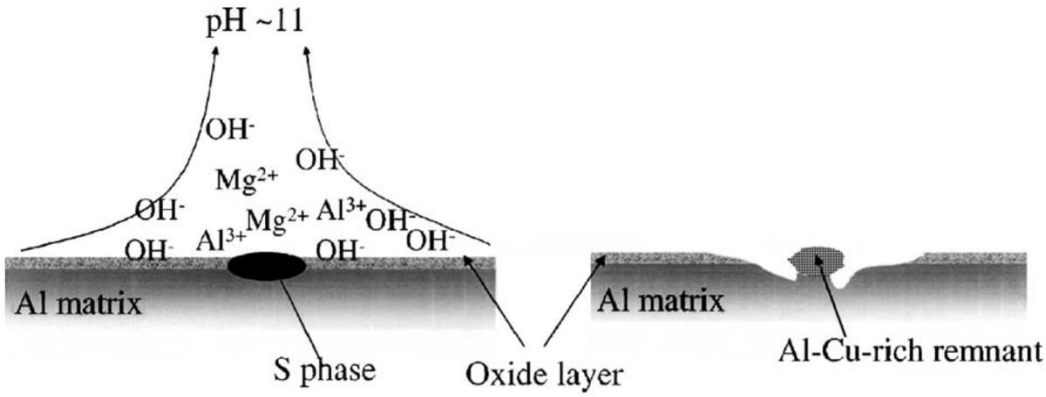

Figure 7: Dealloying phenomena of a S-phase particle. Al and Mg dissolve and leave Cu remnant on the surface which increase the cathode area and oxygen reduction. The formation of OH- induce a local alkalization and the dissolution of the α-Al matrix [52].

Additional results have been proposed by Jorcin et al. [27] corroborating the idea of a matrix dissolution driven by a local pH increase. They demonstrated, by using a pH indicator (bromothymol blue), that the Al/Cu interface sustains high ORR (oxygen reduction reaction) reactions.

2.5.4. The effect of the θ phase (Al_2Cu)

The corrosion process involved with the Al_2Cu has also been extensively studied, mainly in chloride containing environment, and is determined to be driven by a dealloying process. It has been found that this particle acts as a local cathode as its corrosion potential is more noble than the aluminum matrix (corrosion potential). Lebouil et al. demonstrated by AESEC the Cu build-up on the surface of the particle during anodic polarization [53]. Nevertheless, the current densities supported by the Al-Cu intermetallic particles were shown by Lacroix et al. to be 10 times lower than the Al-Cu-Mg intermetallic particles [28]. Moreover, Buchheit et al. also noted the generation of copper ions when the particle is cathodically polarized demonstrating its major role during the corrosion process of Al alloys [47].

2.5.5. The effect of Al_7Cu_2Fe and Al-Cu-Fe-Mn particles

The Al-Cu-Fe-Mn containing phases represent roughly 40 % of the constituent particles found in the AA2024-T3 alloy. The effect of Fe-containing intermetallic particles such as Al_7Cu_2Fe on the corrosion behavior of Al alloys was for a long time not well documented. Fe usually comes from impurities and form the coarse precipitates known also as constituent particles which usually act as cathodic site [23,24,54]. The particles are irregularly shaped, sometimes break into pieces during the rolling process and the particles parts align along the rolling direction. Although the presence of this particle has been noted in AA2024, the electrochemical behavior and the role of Al_7Cu_2Fe have only been investigated recently by Ilebevare et al. [55] and further by Birbilis et al. [56]. For example, Birbilis showed that Al_7Cu_2Fe supports ORR (oxygen reduction reaction) at high current densities over a different range of Cl^- concentration and pH (between 20 μA cm^{-2} and 2 mA cm^{-2}) and the rates were sometimes about 3

times higher than Al_2Cu [56]. Moreover, in 0.1 M NaCl solution, they observed matrix dissolution at the edges and peripheral pitting by FIB (focused ion beam). Similar results were reported by Chen et al.,[42] and Liao et al. [10] in their study of the role of constituent particles in the corrosion of AA2024-T3 alloy. They reported that Al-Cu-Mn-Fe particles act as local cathodes in 0.5 NaCl and were associated to pitting corrosion and the breakdown of the oxide was found at the periphery of the particle.

2.6. Aluminum-Lithium alloys: microstructure

The addition of Li in Al alloys started in the 1920s as the interest of Lithium addition is because of its high solubility in aluminum (maximum solubility of Li in Al is 4.67 % at 596 °C), and its most effective addition to reduce weight, which made it a good candidate for alloying [1] [57]. However, it is only in the 1950s that the effect of Lithium addition was documented. Indeed, Al-Li alloys raised interest in the aeronautic industry as for each percent of lithium added, an increase of the Young modulus (approximately 6 %) was observed as well as a noticeable weight reduction (3 %) [3,58].

The first Al-Li generation was introduced in the 1950s and produced by Alcoa as the 2020 alloy. That time, they noticed an increase of the mechanical features such as the elastic modulus. However, this alloy suffered from several mechanical failures caused by the high amount of impurities such as iron and silicon. During the thermomechanical processing, these impurities would precipitate as constituent particles (Al_7Cu_2Fe or $Al_{12}(FeMn)_3Si$), causing crack initiation as well as ductility issues. Moreover, the Mn addition was revealed to have a detrimental effect on the ductility as it can form coarse intermetallic particles ($Al_{12}(FeMn)_3Si$) instead of forming dispersoids ($Al_{20}Cu_2Mn_3$) which control the grain structure.

The second Al-Li generation took over in 1970s, in order to suppress the mechanical failures encountered with the previous generation. Thus, the Li concentration was reduced but was still more than 2%, the copper content increased (2% or more) and the decrease of impurities concentration was conducted in order to increase the ductility and the toughness. In addition, manganese was replaced by zirconium to control grain structure. These alloys were used in secondary structures on aircraft such as C17 cargo transport of the A340. Although some improvement was noted, this alloy generation still exhibited ductility issues, fracture toughness and delamination during the manufacturing process.

Finally, when the third Al-Li generation was developed in the late 1980s, the lithium content was reduced to less than 2 %. In order to improve the corrosion resistance, zinc was added in solid solution to decrease the potential difference between the grain boundary and the matrix [59–62]. In addition, silver and magnesium were added to accelerate phase nucleation of the hardening precipitate T_1 (Al_2CuLi)[61]. The alloy could reach a strength of 700 MPa with a uniform distribution of T_1 on the matrix. This last generation is currently used and AA2050-T3 belong to this category. **Table 5** gives the chemical composition of the alloy 2050-T3 also used in this dissertation.

Table 5: Chemical composition of the AA2050 used during this PhD (in wt %)

AA2050	*Al*	*Cu*	*Li*	*Mg*	*Mn*	*Fe*	*Si*	*Zn*	*Ag*	*Cr*	*Ni*	*Ti*	*Zr*	*Sr*
wt %	bal	3.30	0.77	0.32	0.39	0.06	0.1	0.02	0.17	>0.01		0.03	0.08	<0.001

The microstructure of aluminum-lithium alloys displays a large number of precipitates which can also be separated into three categories: hardening precipitates, dispersoids and the constituent particles. Amongst the various types of intermetallic particles, which can form during the precipitation, the hardening precipitates are known to play a major role on the alloy strength. For example, Li and Cu can form two different strengthening precipitates: The Al_2Cu phase (θ') or the Al_2CuLi phase (T_1). The θ' phase was preferentially found in Al alloys with low Li content (> 0.6 wt%), as T_1 is usually the major phase in alloys with a Li content between 1.4 and 1.5 wt%. The T_1 formation is also promoted by the addition of small amounts of Mg and Ag as they accelerate its precipitation [63]. Several studies reported the preferential nucleation of this phase at the grain boundaries [60,64]. In addition, Li can be associated with Al to form the coherent phase Al_3Li (∂'). This hardening precipitate is found in high Li containing alloys (>1.4-1.5 wt %); however, its contribution in hardness is less important than T_1 phase and also can have a detrimental effect on toughness. Interestingly, Crookes and Starke [65] reported that the addition of small amount of Mg (0.5 – 1.0 wt %) also stops the formation of the ∂' phase to promote the nucleation of the S' phase (Al_2CuMg). The beneficial effect of Mg on the corrosion resistance was also reported by Niskanen et al. in their study where they noted an inhibition of ∂' phase nucleation in the case of Al-Li alloys. The latter induced an improvement of the corrosion resistance caused by the formation of the Al_2MgLi phase [66]. On one hand, numerous studies investigated the complex relationship between the precipitation reactions in Al-Cu-Mg alloys and Cu:Mg ratio. Three equilibria have been determined: In high Cu content alloys ∂' forms preferentially; when the Cu:Mg ratio is less than 3:1, S' was found to be the major phase; and finally when Cu:Mg ratio was higher than 3:1, the formation of T_1 phase seemed to be favored. **Table 6** reports the effect of the alloying elements on the corrosion and mechanical properties of Al-Cu-Li alloys.

Table 6: Effect of the alloying elements on the mechanical and corrosion properties of Al-Cu-Li alloys.

Element	*Effect*
Li	Increases lightness Increases Young's modulus
Cu	Decreases Li solubility and promotes Li phases precipitation Enhances the mechanical properties by the formation of hardening precipitates Increases the corrosion susceptibility
Zn	Improves the corrosion resistance by decreasing the potential difference between grain boundary and matrix.

Ar	Accelerates phase precipitation of T_1 phase.
Mn	Improves corrosion resistance Controls texture Plays a role in grain size control and retard recristallization
Mg	Promotes T_1 formation by decreasing Li solubility Increases lightness Stops the formation of ∂' phase and promotes the nucleation of the S' phase. Decreases corrosion susceptibility by the formation of the Al_2MgLi phase.
Zr	Controls grain structure by forming Al_3Zr Prevents recrystallization Enables homogenization and improves the mechanical properties. Has a beneficial effect on toughness and stress corrosion cracking resistance.
Fe, Si	Reduces fracture toughness Increases corrosion susceptibility Reduces the amount of alloying elements available for hardening precipitates.

On the other hand, Zr addition was shown to be effective in controlling grain structure by forming the coherent Al_3Zr phase [67]. Besides preventing recrystallization, this phase offers sites for the nucleation of the ∂' phase and enables homogenization which improves mechanical properties. Zr has also a beneficial effect on the toughness and enhances the resistance to stress corrosion cracking [68]. One other typical dispersoid found in AA2050 is the $Al_{20}Cu_2Mn_3$.

Constituent particles are mainly formed from insoluble impurities such as Fe or Si. They reduce fracture toughness and increase the corrosion susceptibility of Al-Li alloys [69]. Moreover, Cu-rich constituent particles reduce the amount of alloying elements available for the hardening precipitates. **Table 7** gives a list of the intermetallic particles found in AA2050 and reported in the literature [60] and **Fig. 8** illustrates the distribution of the intermetallic particles within a grain boundary in second and third generation of Al-Li alloys..

Table 7: List of the intermetallic particles reported in the literature, found in Al-Cu-Li alloys.

Name and stoichiometry	*Size and shape*	*role*
S' Al_2CuMg	Needles, laths, incoherent phase: 0.1-0.2 µm.	Hardening precipitate, found in alloys with Li> 1.3 % [60]
δ' Al_3Li	Coherent with the matrix. Spherical, > 300 nm.	Found in alloys with Li > 1.3% Metastable precipitate
T_1 Al_2CuLi	Rod, plate: 0.05-0.2 µm	Significant effect on strength. Major phase in alloy with medium Li content (<1.4-1.5%)[59,64]. [60]
T_2 Al_6CuLi_3	Plate, between 0.1-0.2 µm	
ß Al_3Zr	Spherical, ~ 100 nm	Dispersoid, prevent recrystallization [64,70].
$Al_{20}Cu_2Mn_3$		
θ Al_2Cu	plate	Precipitate, found in alloys with low Li content.

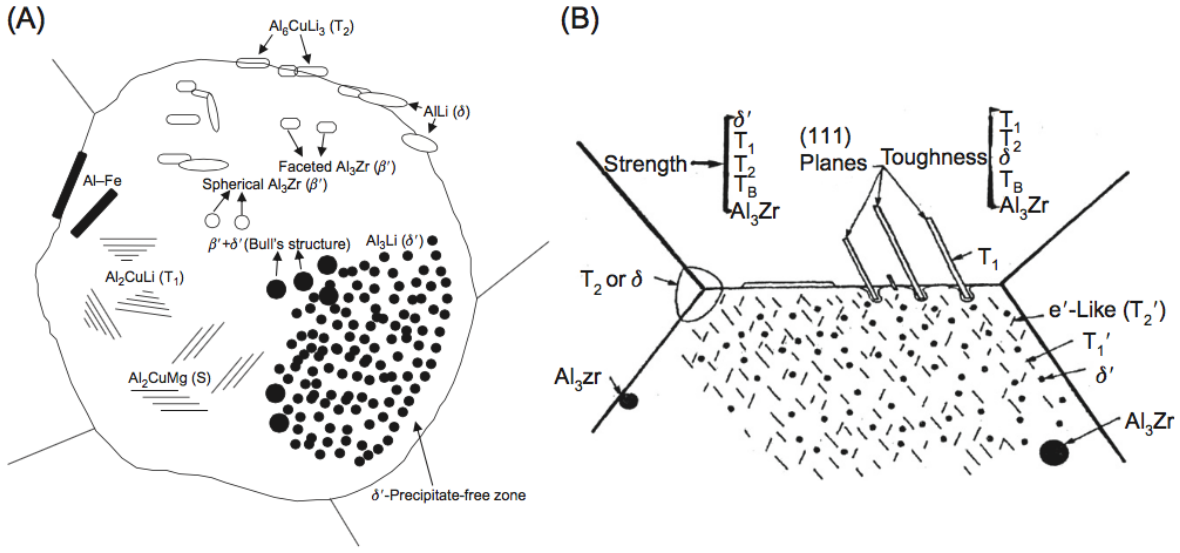

Figure 8: Schematic of the microstructure and intermetallic distribution within a grain boundary in the second (A) and the third (B) generation Al-Li alloys [59].

2.7. The corrosion behavior of AA2050-T3

The development of new light weight Al alloy with improved mechanical properties and corrosion performances gained a considerable interest. However, Al-Li alloys also suffer from localized corrosion and particularly from intergranular corrosion (IGC) and stress corrosion cracking (SCC). Interestingly, unlike 7XXX series Al alloys, the intergranular corrosion and stress corrosion cracking susceptibility of Al-Cu-Li was decreasing in the peak aged conditions. The studies realized on corrosion susceptibility of Al-Li alloys agreed on the fact that the microstructure affects the electrochemical behavior of the alloy [66]. In this section, the relationship between the alloy microstructure, IGC and SCC corrosion along with the mechanisms proposed in the literature will be presented.

2.7.1. Intergranular corrosion (IGC)

Intergranular corrosion is usually defined by a galvanic corrosion between the grain boundary and the adjacent matrix. In the case of Al-Cu-Li alloys, it was not well established how this phenomenon occurs, however, the literature lists three mechanisms:

- The galvanic couple theory based on the dissolution of precipitates located at the grain boundary and the surrounding matrix
- The precipitate free zone model taking into account the Cu depletion caused by the nucleation of precipitates at the grain boundary
- The combination of both models suggesting the anodic dissolution of the precipitates at the grain boundary.

The galvanic couple theory was based on the reactivity of T_1 phase at the grain boundaries. This theory has been introduced in the context of Al-Li alloys by Rinker [71]. It has been suggested that these particles exhibit a less noble potential than the adjacent matrix, promoting the formation of a galvanic couple between the particle and the matrix. Buchheit et al. [72] studied the electrochemical behavior of a synthetic T_1 phase in 0.6 M NaCl, and determined that the corrosion potential of these precipitates was more cathodic than the AA2090 matrix (-1.10 V / ECS for T_1 and -0.72 V / ECS for AA2090). These active phases which are known to nucleate preferentially at the grain boundaries, act as local anode causing their selective dissolution and subsequently, intergranular corrosion. Recently, Luo et al. [73] studied the localized corrosion of Al-Cu-Li alloys in NaCl solution and suggested that the pitting bottom, initiated by the coarse intermetallic particles fallout, acts as an opening for further dissolution. The pit will grow beneath the Al matrix and when grain boundaries are reaching T_1, the Li contained in the phase will selectively dissolve.

The precipitate free zone model (PFZ). This notion has been introduced by Galvele and Di Micheli [45] when the galvanic couple theory could not explain why the presence of Cl^- ions was necessary to get intergranular corrosion in Al-Cu alloys. They supported that the intergranular corrosion was induced by a difference in breakdown potential of the different phases in the grain boundaries and not by a difference in potential between them. In their study, they synthesized three phases found in the grain

boundary area: Al-4% Cu, Al_2Cu and Al-0.2% Cu representing respectively the matrix, the precipitate and the Cu depleted zone. They determined their electrochemical behavior by realizing a series of anodic polarization in NaCl solution. From the results, they concluded that the breakdown potential of the Cu-rich phases was about 100 mV higher than the specimens with lower Cu content. Moreover, the pitting potential of the Al-4%Cu was found to be similar to the Al_2Cu specimens. On the other hand, the Al-0.2% Cu representing the Cu-depleted zone exhibited a similar pitting potential to high purity Al. In addition, they studied the effect of heat treatment and the nature of the environment and they were able to determine the following conditions in which intergranular corrosion will occur:

- A Cu-depleted zone has to be present in the alloy,
- The aggressive medium has to be able to break the passive film,
- The breakdown potential of the depleted zone needs to be lower than the matrix
- The corrosion potential needs to be above the breakdown potential of the depleted zone and lower than the matrix breakdown potential.

Later, Kumai et al. [74] investigated the role of the PFZ and the Cu distribution on the IGC of 2090 Al-Cu-Li alloys. To this end, they prepared two different alloys, one with a similar composition to the 2090 (Al-2.37%Li - 2.49% - 0.13%Zr called B) and a second with the same Li and Zr concentrations but not Cu (called A). The alloy A exhibited a fairly uniform distribution of δ' throughout the grain except at the periphery of the high angle grain boundaries where a PFZ was found. On the other hand, the microstructure of alloy B revealed a heterogeneous dispersion of Cu containing phases. A copper depleted zone and a PFZ were found along the high angle grain boundaries. In addition, Cu containing phases, presumably T_1 or θ were found on the sub-grain boundary, but also intragranularly leading to a Cu-depleted zone along the sub-grain boundary. They demonstrated that the Cu containing alloy, experienced intergranular corrosion whereas the Cu free Al-Li alloys did not show intergranular corrosion. Although both alloys had PFZ along the grain boundaries, they highlighted the importance of the nature of the precipitate around PFZ in the intergranular corrosion of this alloy (**Fig. 9**).

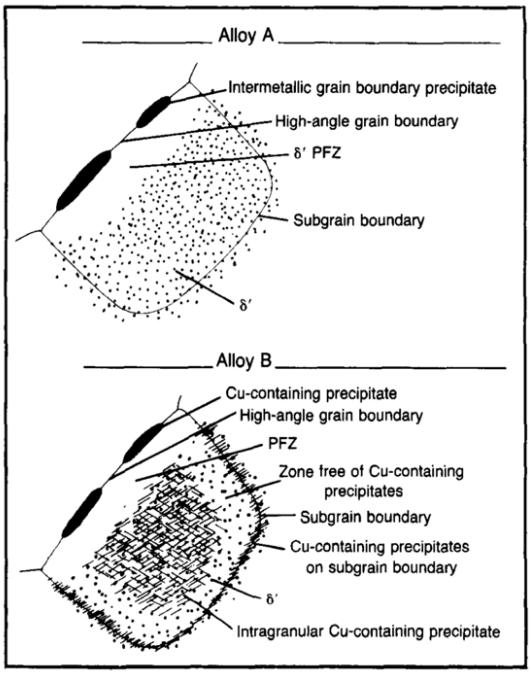

Figure 9: Schematic illustration of the phase changes occurring within Alloys A and B as a result of SHT (solution heat treated) and aging at 200°C [74].

In order to evaluate the theory suggested by Kumai et al, Buchheit et al. [72] studied the effect of the T_1 phase in the corrosion of AA2090. To that end, they prepared an artificial T_1 phase to represent the grain boundary, a Cu-depleted specimen (they used pure Al) and used a AA2090 to simulate the matrix. They realized corrosion potential (E_{corr}) and anodic polarization measurements in 0.6 M NaCl and determined that T_1 was the most active phase - with a very high dissolution rate (10^{-4} A cm^{-2} at E_{corr}) - followed by the Cu-depleted zone and then the α-Al matrix (> 10^{-6} A cm^{-2} at E_{corr}). Moreover, they determined that subgrain boundary attack was controlled by the selective dissolution of T_1, which is not in agreement with Kumai theory. Indeed, unlike the other 2XXX series Al alloys, Buchheit et al. suggested that the potential difference between the PFZ and the grain boundary in Al-Cu-Li (which is T_1 rich [60]) leads to the preferential attack of T_1. Moreover, they explained this as resulting from the creation of a locally acidified environment leading to a continuous attack of the α-Al matrix, exposing more T_1 phase which make the process repeat itself.

On the basis of the precipitate free zone model and the galvanic couple theory, Li et al. [75] investigated the mechanism of IGC in the Al-Li alloy 2195 in 4% NaCl solution. The methodology was identical to Buchheit's research as T_1, θ' phases and the α- Al matrix were manufactured to simulate subgrain, grain boundaries and PFZ respectively. Their electrochemical behavior was characterized individually by potentiodynamic testing. The specimens were then coupled and immersed in NaCl during 10 days and potentiodynamic testing was carried out. The results demonstrated that at the beginning of the immersion test, the T_1 phase is more active than θ' and α- Al matrix which corroborates with Buchheit's results. On the contrary, the θ' phase was found to act as a cathode in the alloy. However, they noticed a change

of T_1 potential towards more positive values due to the dealloying of Li from T_1, leaving Cu on the surface. As a result, the α- Al matrix becomes anodic leading to the dissolution of the PFZ. Consequently, Li et al. suggested a mechanism which involves first the dissolution of the Li contained in the T_1 phase which results in a Cu enrichment at the surface. The potential of the dealloyed particle will progressively become more noble than the PFZ, causing the dissolution of the PFZ. The dissolution of this PFZ will expose more T_1 phases that dissolve continuing the process **Fig.10**.

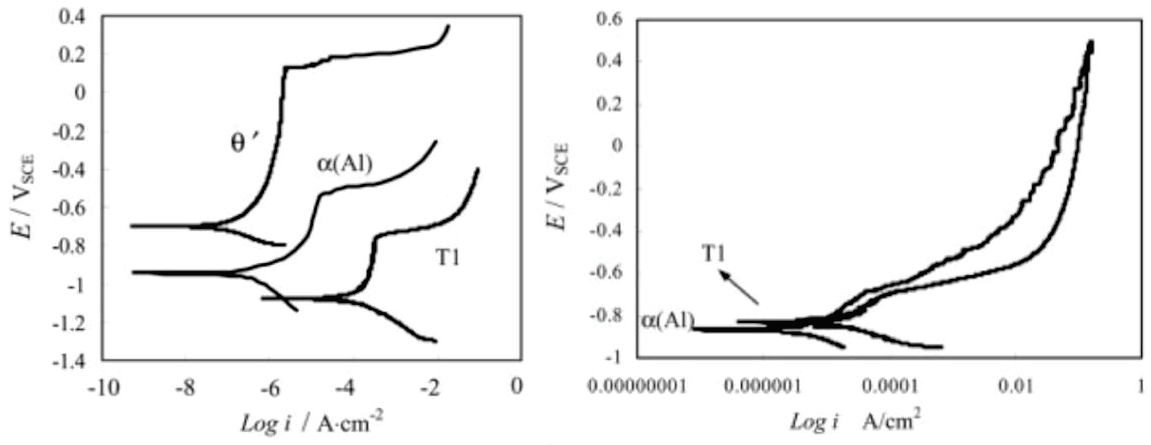

Figure 10: Potentiodynamic polarization curves of different phases T_1, θ and the α-Al matrix in NaCl A) after direct immersion B) after 10 days of immersion [75].

In summary, in spite of the controversy surrounding the mechanism involved in the intergranular corrosion in Al-Cu-Li alloys, it is commonly accepted that the T_1 phase as well as the PFZ play a major role in the intergranular corrosion susceptibility of Al-Cu-Li alloys.

2.7.2. Stress corrosion cracking (SCC)

The mechanisms involved in SCC are controversial. Two theories were developed in the literature: the first theory explains that SCC is driven by the anodic dissolution of T_1, T_2 and δ'phases on the grain boundaries [76], or is activated by the Cu depleted zones along the grain boundaries [60,69,76]. The second theory however considers the possibility of hybrid generation promoted by Li, causing hydrogen fracture in the alloy. As a matter of fact, several studies suggested that the cathodic pre-charging of Al-Li-Cu-Mg alloys with hydrogen induces the loss of mechanical properties [77]. The experimental data suggest that the crack initiation and the propagation could be triggered by two different processes. The anodic dissolution process seems to stimulate the crack initiation and the propagation could also be induced by a hydrogen related process.

2.7.3. The effect of age hardening on the corrosion properties

Several studies demonstrated a net correlation between the heat treatment and the corrosion morphology of Al-Cu-Li alloys. Three different aging conditions are deployed in industry: under-aged, peak-aged,

over-aged. Singularly, the Al-Cu-Li alloys exhibit a maximum IGC/IGSCC resistance in the peak-aged conditions [71][78].

In the underaged condition, it was suggested that this intergranular corrosion was generally attributed to the distribution of T_1 and Al-Cu-Mn intermetallic particles, regularly found in Al-Cu-Li alloys. Moreover, Henon and Rouault [79] reported a "desensitization" in the peak aged conditions explained by the effect of the aging temperature and time on the distribution of T_1 precipitates at the grain which significantly decreases the potential difference between the grain boundaries and the matrix, and reduces the selective dissolution of grain boundary precipitates. This desensitization window has been mentioned by Connolly et al., for AA2096 and AA2090 alloys and they determined an increased SCCC susceptibility in the underaged and overaged conditions [80]. In contrast, in the overaged conditions, it was reported that the aging time would promote the formation of larger T_1 at the grain boundaries and favor the development of strains. Moreover, the aging time also favors the precipitation of θ' or S' on the grain boundaries creating what is called precipitate free zone (PFZ). These phenomena will accentuate the potential difference between the grain boundary and the matrix and favor micro-galvanic coupling leading to intergranular corrosion.

3. THE SURFACE TREATMENT OF AL-ALLOYS

The corrosion of Aluminum has to be controlled before they are introduced in service. It is commonly accepted that surface conditioning is extremely critical to maintain an optimum corrosion resistance of coated aluminum alloys [81,82]. The surface conditioning of aluminum alloys usually involves:

- Surface pretreatment
- Chemical coating
- Anodizing and sealing
- Painting.

The surface, as mentioned previously, suffers from surface defects caused during the manufacturing process. The rolling, the storage environment, the natural oxide or other contaminations need to be removed before the coating application. The particularity of the surface microstructure in terms of elemental composition and distribution has been described previously. It has been pointed out that the surface microstructure has an impact on the corrosion properties of the alloy but also can have a detrimental effect on the subsequent chemical coating [81,83–85]. The purpose of the pretreatment is to provide an electrochemically homogeneous surface to prevent localized corrosion induced by the micro-galvanic coupling between the intermetallic particles and the matrix. Numerous studies also highlighted the impact of surface conditioning on the quality of the coating [81,86]. These observations lead to the establishment of specific requirements for every metal finishing process to meet aerospace standards for corrosion resistance.

3.1. Solvent cleaning

Solvent cleaning has been used to eliminate oils and greases applied on the surface during the transport. However, this step is progressively removed from the surface finishing processes. Trichloroethane, trichloromethane or trichloroethylene are examples of degreasers used in industry. In contrast, the majority of the research laboratory use ethanol or acetone which shows the significant opposition between the metal finishing industry and the research laboratories in the choice of cleaning procedures or operating parameters. For example, the effect of acetone on the surface of AA2024 after polishing has been studied by Chidambaram and Halada [87], who reported the presence of carboxyl groups on the surface. They suggested that this carboxyl group may form acetic acid on the surface and support the formation of copper-chloro complexes which stimulate corrosion [88]. In addition, several issues have been pointed out when using trichloroethane in vapor degreasing. For example, it has been reported that HCl could be formed and attack the Al matrix [82]. Further investigations using XPS conducted by Hughes et al. [89] showed the presence of surface chlorine within the Al oxide confirming the theory of a corrosion process triggered by HCl.

3.2. Alkaline cleaning

Alkaline cleaners are regularly used in industry to dissolve the natural oxide film, the Al matrix, as well as oils and greases found on the surface. Usually, two types of alkaline cleaners are used in industry:

- The carbonate based cleaners
- The sodium hydroxide based cleaners

The effect of alkaline cleaners, particularly on the quality of the subsequent conversion coatings and anodizing, has been extensively studied [90,91]. Numerous studies evidenced an enrichment in alloying element as a results of the dissolution of the Al. Indeed, during the NaOH immersion, the selective dissolution of Al occurs and the insoluble alloying element such as Cu, Fe [54], Mn, Mg or Si remain on the surface as a film [92]. For example, Hughes et al. [89] observed an increase of Cu, Fe and Mn after alkaline degreasing, demonstrating the film build up on the surface. The mechanism of Cu buildup and nanoparticles generation during alkaline etching in Al alloys have been studied in details by Liu et al. [93] in a simulated θ phase (Al-30% at Cu alloy). They monitored the formation of the Cu enriched film by RBS (Rutherford backscattering), XPS (X-ray photoelectron spectroscopy) and TEM (transmission electron microscopy) and suggested that Cu enrichment occurs beneath the Al oxide film, then clustering of copper atoms, followed by their occlusion caused by the formation of hydrated alumina around [94]. On the other hand, Lunder and Nisancioglu studied the behavior of Al-Cu-Mn-Fe constituent particles during the etching in alkaline solution [16] and found selective dissolution of Al within the particle and the enrichment of Fe and Mn. Moreover, they determined an increase of the corrosion susceptibility for different alloys. Additional results concerning the dealloying of S-phase particle in alkaline media were reported by Dimitrov et al. [95]. Nevertheless, with the apparition of new Ce-based conversion coating, NaOH based cleaners appeared to cause defects and corrosion failure in the coating [96] and carbonate base cleaners were shown to enhance the quality of the coating. The silicate and carbonate based cleaners exhibit a lower etch rate, however several researchers observed a Mg, Zn and Si enrichment at the surface after immersion in a silicate based alkaline cleaner [89,97,98].

3.3. Acid deoxidizer (acid pickling)

Subsequently, the acid deoxidizer is used to dissolve the intermetallic particles and the Aluminum oxide left after the alkaline cleaning. More generally, the deoxidation has been described as a three step process [98–100]:

- Stage 1: Upon immersion, a preferential dissolution of component of the oxide left after alkaline cleaning. These elements include Mg, Zn oxides and Si-containing phases. The majority of deoxidizers with a low etch rate do not go beyond stage 1.
- Stage 2: The oxide left after alkaline cleaning is dissolved and begins the attack of the underlying matrix. This process involves the dissolution of a large variety of alloying elements

and each of them must reach an equilibrium between accumulation and dissolution. Thus, in this intermediate stage the dissolution of Al leaves behind an enrichment of alloying elements.

- Stage 3: The alloying element dissolution process reaches an equilibrium between dissolution and accumulation. However, the equilibrium between surface oxide formation and dissolution appears to move towards dissolution while a thin oxide layer remains on the surface.

The use of Cr-based formulations appeared to remove successfully the S-phase particles and the Al-Cu-Fe-Mn containing particles. Several formulations were developed and are currently used in industry such as Chromium and sulfuric acid based deoxidizing agents. The HF/Cr/HNO_3 deoxidizer has also been effective for the S-phase and Al-Cu-Mn-Fe particles removal. However, over the past few years, considerable efforts have been made to use environmental friendly formulations.

In this context, the development of Cr-free chemical pretreatment formulations gained through the years a considerable interest. Depending on the requirements, the composition can contain HF to increase the etching rate. In the case of Al alloys with high Cu content, the use of HNO_3 base deoxidizer is recommended, sometimes with HF addition [101,102]. Nevertheless, Nelson et al. [99] demonstrated a decline of the corrosion resistance of the subsequent chemical coating when a simple HNO_3/HF deoxidizer was used. The results evidenced the enrichment of certain alloying elements such as copper on the surface. In addition, Hughes et al. studied the effect of various deoxidizing agents, like nitric acid (HNO_3), sulfuric acid (H_2SO_4), phosphoric acid (H_3PO_4) or hydrofluoric acid (HF) using *ex situ* surface characterization – scanning electron microscopy (SEM), transmission electron microscopy (TEM), X-ray photoelectron spectroscopy (XPS) and Rutherford back scattering (RBS) - and concluded that only the HNO_3 treatment combinations produced a surface free of copper-rich smut [103]. However, Liu et al. [104] observed copper enrichment after HNO_3 immersion via RBS and TEM analysis, similar to the extent obtained from NaOH immersion. Using XPS, Moffit et al. [97] measured a thin residual copper layer beneath an Al oxide film after pretreatment in a nitric acid based oxidizer. Other Cr-free deoxidizers have been studied in the literature including HNO_3/BrO_3^- [86] and HNO_3/HF with the addition of oxidants such as Fe^{3+} [98,105,106]. Hughes et al. reported that ferric ion based deoxidizers exhibited a lower etch rate compared to Cr-based deoxidizers, however, an effective removal of the S-phase and a severe attack of Al-Cu-Fe-Mn coarse particles was seen [106].

Recently, rare earth - based deoxidizers have been considered as an alternative to Cr [84,98,107]. For example, Hughes et al. studied the effect of a HF/Ce based deoxidizer for a AA2024-T3 alloy and noticed the dissolution of S-phase and partial removal of the Al-Cu-Fe-Mn particles with the addition of fluoride ions. However, a thin copper film of approximately 200 nm in size was found on the surface after the treatment [108] but was effectively removed by the addition of oxidants such as H_2O_2 and $K_2S_2O_8$ [109]. Recently, Gordovskaya et al. [84] investigated the effect of $CeCl_3$ and $CeCl_3/H_2O_2$ deoxidizers on the intermetallic particles removal and their impact on the anodizing behavior and the corrosion resistance. Their results demonstrated a significant impact of $CeCl_3$ containing deoxidizer on the S, θ and Al-Cu-Fe-Mn-(Si) particles, and the improvement of the corrosion resistance of the

anodized alloy has been noted. It appears that the final chemistry of the alloy is dominated by the deoxidizing step which leaves a more or less protective oxide film on the surface [89].

4. MOTIVATION AND OBJECTIVES OF THE THESIS

Although considerable advances have been made towards a better understanding of Al alloys reactivity during a surface treatment process, the main difficulty encountered in research and development is the significant contrast between the metal finishing industry and the research lab work. As an example, the different procedures routinely used in a "corrosion lab" usually involve immersion tests, polarization measurements, corrosion current analysis or surface analysis such as optical microscopy or scanning electron microscopy. The major limitation of these tools, if we consider the case of the surface treatment process at OCP, are a) they do not provide information on the dissolution kinetics and corrosion rates, b) cannot distinguish the reactivity of multiple elements c) cannot identify in real time selective dissolution processes. However, these data would be very valuable for research formulation, particularly because the necessity of the replacing Cr^{VI} becomes imperative.

To date, the data reported in the literature regarding the effect of the pretreatment concern only the reactivity of Al-Cu or Al-Zn alloys. In addition, the information is provided by *post mortem* analysis which does not enlighten their surface reactivity during the metal finishing process. Although the synergetic effect of Li and the alloy temper on the corrosion of Al-Cu-Li alloys has been extensively documented, the reactivity of Al-Cu-Li alloys during a pretreatment is not thoroughly reported. Particularly, we would like to understand how the relationship between the Li distribution, the microstructure and the elemental reactivity affects the quality of the pretreatment. This knowledge should be considered essential as the 2024 or 7075 Al alloys are progressively replaced by this new generation which at this time undergoes the same surface treatment process.

To achieve this objective, this work was separated into three parts:

- The first part consists of the development of the AESEC methodology to provide a quantitative analysis of elementary dissolution kinetics in near industrial conditions. This implies high electrolyte temperatures, high dissolution rates and the use of aggressive solutions, much more extreme conditions than have been previously used with the AESEC technique, as well as the rapid change of electrolytes. This methodology will be based on the AESEC technique with several experimental modifications to optimize the results.
- The second part concerns the validation of this methodology using the well-known AA2024-T3. The results will be compared to the data provided in the literature and to conventional *ex situ* techniques (scanning electron microscopy, optical profilometry).
- The final part is devoted to the application of the methodology on the Al-Cu-Li-Mg alloy AA2050 to characterize the surface composition and morphology of the AA2050 after pretreatment. The goal is to highlight the role of Li during the surface treatment and isolate its

impact on the corrosion properties and eventually predict the durability of pretreated or coated AA2050.

CHAPTER II: MATERIALS & METHODS

"La simplicité est la réussite absolue. Après avoir joué une grande quantité de notes, toujours plus de notes, c'est la simplicité qui émerge, comme une récompense venant couronner l'art. "

"Simplicity is the final achievement. After one has played a vast quantity of notes and more notes, it is simplicity that emerges as the crowning reward of art."

Frédéric Chopin.

1. INTRODUCTION

The measurement of corrosion rates under laboratory conditions is a necessary but challenging endeavor. Conventional electrochemical methods are widely used as tools to study corrosion mechanisms, metal dissolution, kinetics and corrosion inhibition [110–112]. However, their application to complex reaction processes such as the dissolution of multi-element and multiphase alloys is fraught with difficulty. It is easy to measure electron transfer, have a high degree of precision and dynamic range, however it is much more difficult to know precisely how the electrons are being distributed amongst a variety of possible chemical reactions. Therefore, it has been of considerable interest to couple the electrochemical technique with other forms of analysis that yield insight into the chemical transformations that occur during electron transfer. Common techniques include UV-Visible, infrared or Raman "spectroelectrochemistry" and coupling with a quartz micro balance [113]. A "classical" example of such a coupled technique is the rotating disk electrode (RDE) or flow jet-cell, designed to investigate the reactions involving the formation of products [114]. With these methods, it is possible to detect electroactive species formed at the working disk electrode downstream at the ring electrode. In this way, the rate of production may be quantified. The major difficulty with this technique is that only a limited number of ions may be detected "downstream" at the ring depending on their electrochemical properties. During the last decades, several experimental techniques have been developed involving the coupling of electrochemical flow cells with different downstream spectroscopic tools such as the inductively coupled plasma atomic emission spectrometer (ICP-AES), also referred as the atomic emission spectroelectrochemistry (AESEC) [111,115–120], inductively coupled plasma mass spectrometer (ICP-MS) [121,122].

The AESEC is a methodological tool used in a similar manner as the RDE or flow jet cell. With AESEC, we replace the downstream electrochemical detection with ICP-AES so as to yield a quantitative elementally sensitive analysis of dissolution on an element by element basis. This yields a direct measurement of the elemental dissolution rate during the reaction of material with an electrolyte [111] as shown in **Fig. 11**. The main idea of this technique is to understand how a surface behaves in terms of elementary dissolution reactions during any electrochemical test or even at open circuit conditions.

This chapter will focus on the AESEC technique, the data calculations and the different set-up modifications. Furthermore, surface analytical techniques will be described, used to give deeper insights to the chemical and microstructural changes that occurred during the corrosion processes. For example, surface topography, and chemical distribution of the alloy were determined by scanning electron microscopy coupled with EDS analysis. Different vibrational spectroscopy methods such as infrared and Raman spectroscopies were utilized and combined with X-ray diffraction (XRD), to investigate the chemical nature of corrosion products. Moreover, when in-depth resolution was required, glow discharged optical emission spectroscopy (GDOES) or X-ray photoelectron spectroscopy (XPS) were

used to have access to the surface and bulk composition. These methods will be explained in more detail hereafter.

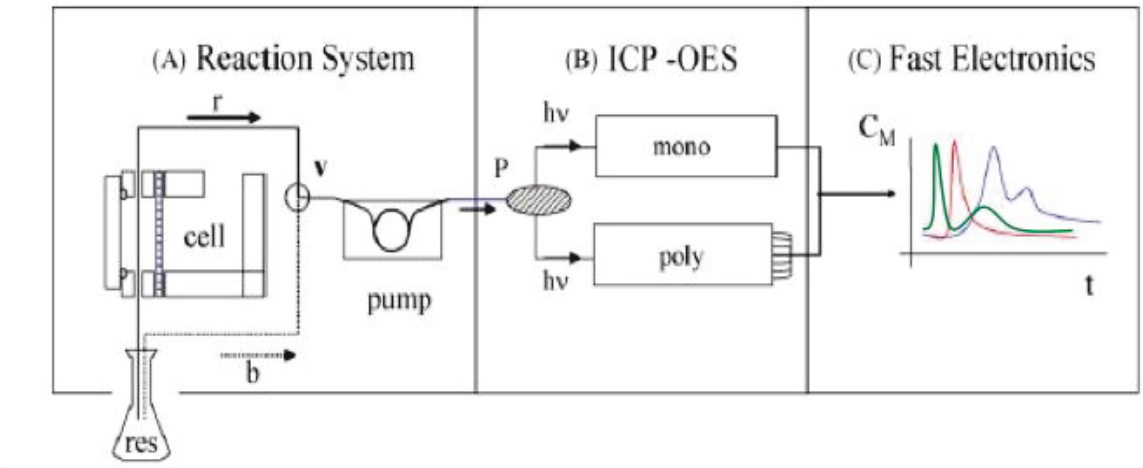

Figure 11 : Schematic of the AESEC method referring to the coupling of an electrochemical flow cell and the ICP-OES [111].

2. MATERIALS & METHODS

The AESEC method was the main experimental technique used during this PhD thesis. However, the difficulties encountered during some preliminary experiments led to several modifications of the general set-up shown in **Fig. 11**. As such, and for more clarity, the AESEC instrumentation and its modifications were separated into three different parts: the first part will describe the electrochemical flow cell and the different functionalities of the flow injection valve. The second part will give more details on the ICP-AES and finally, in the third part, the data treatment and element quantification will be explained.

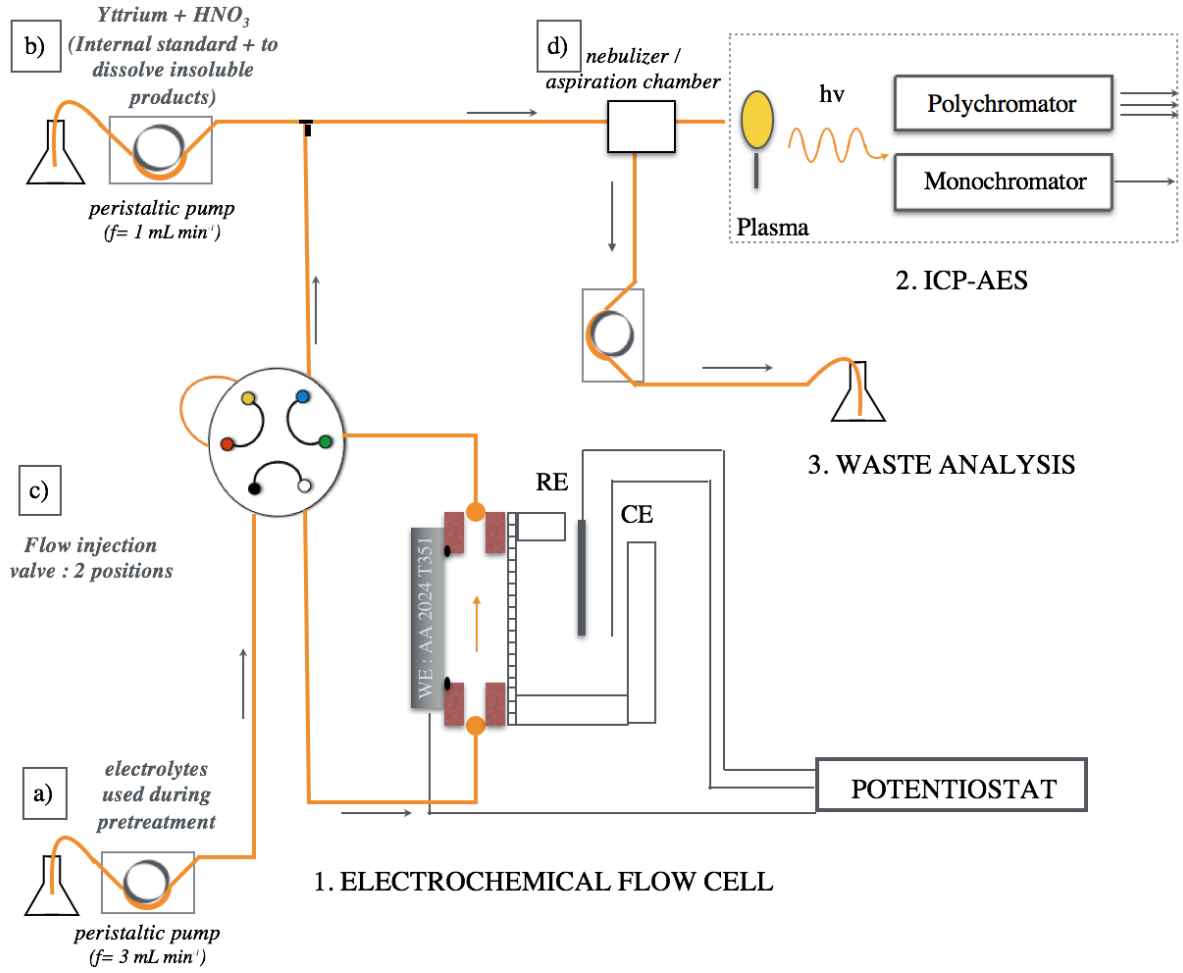

Figure 12 : Schematic of the final experimental set-up showing: the electrochemical flow cell, two pumps with their electrolyte reservoir a) and b), a flow injection valve c) connected to the electrochemical flow cell. The ICP-AES collects the electrolyte to measure the dissolution rates and the potentiostat follows the electrochemical data. b) Injects, after the flow cell, 2.8 M HNO_3 with 15 ppm Y at 1 mL min $^{-1}$. d) represents the nebulizer and aspiration chamber system which collects ~ 5 % of the electrolyte to inject it in the plasma. The remaining 95 % were collected downstream. A recirculating temperature controlled water bath and a hollow copper block (not shown here) were used to maintain the electrolyte and the sample at a constant temperature (60 °C).

2.1. Part A: The flow cell and electrolyte transportation.

2.1.1. The electrochemical flow cell

The first part of the system is a three electrode electrochemical flow cell composed of two compartments separated with a cellulose membrane: the first one is in contact with the working electrode (WE) and has a geometric surface area of 0.51 cm^2. The surface is defined by an O-ring and the sample is maintained at a constant pressure against the O-ring to ensure a reproducible exposed surface area. The second contains the reference electrode (RE: Ag/AgCl) and the counter electrode (CE: Pt sheet) filled with electrolyte (**Fig. 13**.). The cellulose membrane allows the current transfer between the working and counter electrode without bulk mixing the electrolytes between the two compartments (**Fig. 14**).

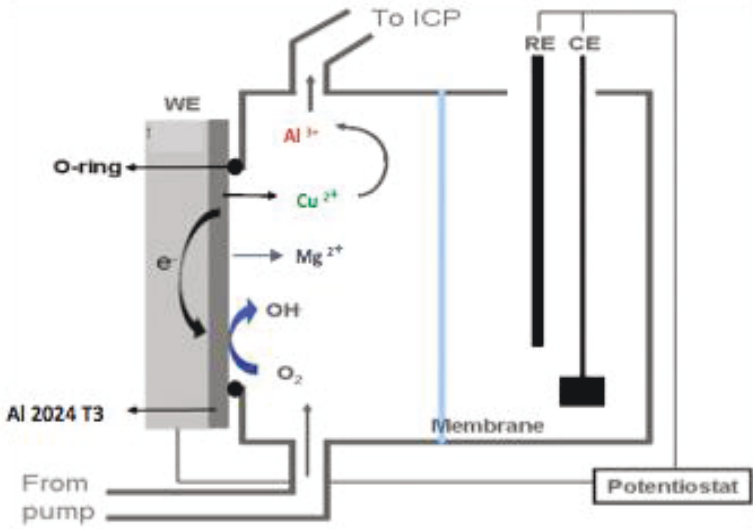

Figure 13 : Detailed schematic of the electrochemical flow cell showing the compartment with the flowing electrolyte reacting with the WE, separated from the second compartment by a cellulose membrane where there is the RE and CE (not to scale).

The electrolyte is transported at a constant flow (3 $cm^3\ min^{-1}$) through the first compartment (0.20 cm^3), reacts with the sample and flows continuously to the second system: the ICP-AES. The small volume of the compartment prevents any possible electrolyte accumulation during the experiment and gives a real time analysis of the reactions. The electrolyte input and output are respectively at the bottom and the top of the cell, in order to avoid bubble accumulation that may be generated during the course of the experiment.

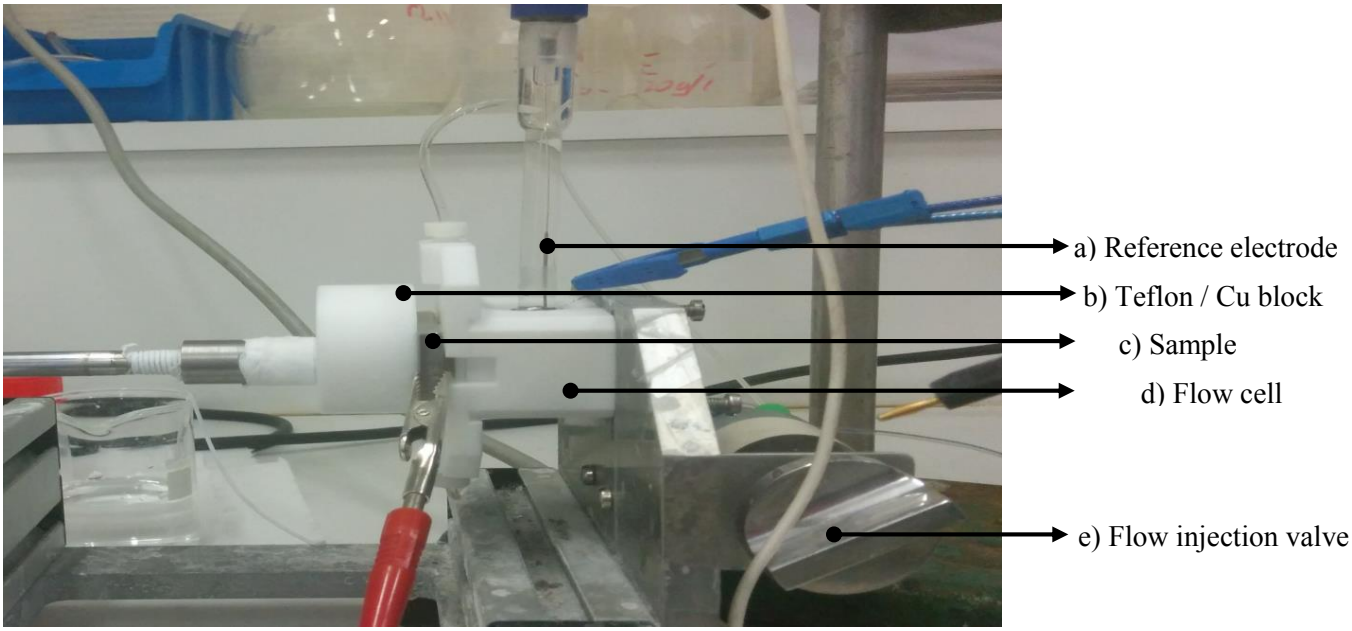

Figure 14 : Picture showing the electrochemical flow cell with the compartment containing a) the reference electrode, b) a Teflon block (changed to a Copper block if working at high temperature is needed) maintaining the sample c) at a constant pressure, against the flow cell d) and e) the flow injection valve.

A Gamry Reference 600™ potentiostat from Gamry Instrument is used for the electrochemical experiments. The analog potential and current signals are routed into the ICP-AES data acquisition circuit to guarantee an equivalent time scale between both measurements.

2.1.2. Flow injection valve system

For the calibration procedure and background measurement, the flowing electrolyte is directly introduced to the ICP-AES without going through the electrochemical flow cell. The flow injection valve has two positions: (1) as shown in the diagram, the electrolyte is transported through the cell to the ICP-AES or (2) the electrolyte bypasses the cell and is transported to the ICP-AES. A valve developed for flow injection analysis (FIA from FIALab) was made from Kel-F(CTFE)™ for the stator material and Valcon M™ for the rotor, materials chosen for their good chemical resistance to nitric acid (**Fig.14**).

2.2. Part B: The inductively coupled plasma atomic emission spectrometer (ICP-AES)

The inductively coupled plasma atomic emission spectrometer is a well-known technique, regularly used in analytical chemistry and is sensitive to the majority of the elements in the periodic table. The ICP method relies on the excitation/ionization of atoms by a high source of energy- the plasma- to produce the emission of radiations at specific wavelengths for each atom.

2.2.1. Electrolyte introduction system

The electrolyte transport is realized by a peristaltic pump with Tygon™ capillaries. In this work, a 3 mL min^{-1} flow rate was used unless otherwise stated. The sample introduction in this system consists of a

pneumatic nebulizer and a cyclonic spray chamber as represented in **Fig. 15**. The pneumatic sample introduction is the most common method used to inject an analyte into the plasma. Through the end of the nebulizer, the argon gas flows at a high speed rate to create a fine aerosol. The small size of the nebulizer orifice ensures the good stability and reproducibility of the analysis. Nevertheless, the tip could sometimes be obstructed if the solution has more than 0.1% dissolved solids. Depending on the application and the electrolyte used, different nebulizers and spray chambers are provided. For this PhD thesis, a Meinhard® K3 concentric nebulizer was used, specifically designed for concentrated solutions having solid contents. Moreover, an argon humidifier was used during the experiments in order to prevent salt deposits in the introduction system by humidifying the argon before it enters in contact with the analyte.

Once the aerosol is produced, the cyclonic spray chamber collects all the droplets and selects by inertia effect only the ones with a diameter less than 10 µm (approximately 5 %) to transport them to the torch. The remaining 95% is evacuated from the system by the peristaltic pump downstream. It is noteworthy to mention that the intensity of the signal generated is directly correlated to the quantity of elements analyzed by the ICP-AES. Usually a surface treatment induces a high quantity of dissolved elements. However, if these amounts are higher than the linear dynamic range – LDR- (between 10^6 to 10^9 times the detection limit for each line [123]), the electronic signal cannot be correctly quantified and may lead to the saturation of the detector. In our experiments, it was important to reduce the amount of droplets injected to the plasma. Consequently, a specific cyclonic spray chamber with an internal glass tube was used, to significantly decrease the quantity of analyte introduced to the torch and improve the ICP-AES analysis.

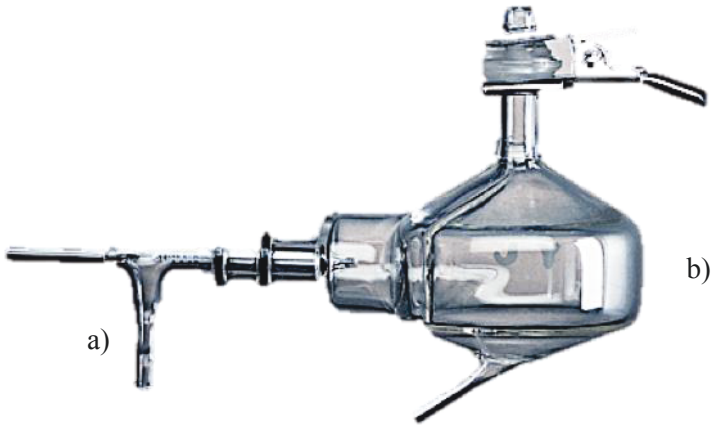

Figure 15 : Picture of the electrolyte introduction system involving a) the nebulizer and b) the cyclonic spray chamber.

2.2.2. Internal standard and second peristaltic pump

During a surface treatment process, the reactivity of a sample to an aggressive electrolyte can lead to massive dissolution. However, if the material has a complex microstructure –like the AA2024-T3- the surface may react differently depending on its composition. For example, in an alkaline environment,

the Al matrix is highly soluble [2] and the reaction produces hydrogen gas. However, a majority of the alloying elements included in the intermetallic particles are not soluble. Consequently, there will be particle detachment and release in the electrolyte. Moreover, the hydrogen evolution can interrupt the electrolyte flow and cause signal fluctuations.

It is well known that some of the intermetallic particles found in the A2024-T3 have a size larger than 10 µm [5,6]. Consequently, if one of these detaches from the surface and is released in the system, it has probably no chance of being injected into the plasma. (cf 3.2.1.). A second peristaltic pump, injecting a 2.8 M HNO_3 solution was hence added to the system to dissolve, or at least significantly reduce, the size of those large insoluble products that could form during the alkaline exposure of the alloy. The introduction was realized by a "Y" connection after the output of the cell and before the electrolyte introduction to the nebulizer. The flow rate was fixed at 1 mL min^{-1} (a higher flow rate leads to signal perturbations into the introduction system) and the pH was controlled at the output of the spray chamber. Usually, during an ICP-AES analysis, an internal standard is added to the solution to correct signal perturbations caused by pump fluctuations, gas bubbles, or the presence of particles that could block the capillaries. The choice of the internal standard relies on two important conditions: the element has to be absent from the analyzed solution, and should not induce interferences with other elements. The Yttrium was, in our case, used to control the course of the experiment as it allowed the distinction between signal perturbations and fluctuations resulting from bubble formation. The latter was injected downstream the flow cell by the second pump in addition to the 2.8 M HNO_3 solution.

2.2.3. Plasma: excitation source of the ICP-AES

The plasma is created by introducing Argon gas into a quartz torch and applying a radio frequency power (between 700 and 1500 Watts) at a frequency of 27 or 40 MHz. The magnetic field and the RF current will be created through two copper coils where in the middle is placed the end of the torch. The latter is composed of two quartz tubes, one injector in alumina and has three inlets (**Fig.16**):

- One at the bottom where the analyte is introduced through the injector,
- A second called "argon flow", located in the outer channel, where the argon gas spirals tangentially around the chamber as it goes upwards at a rate of 7-15 L min^{-1}.
- A third inlet called "auxiliary flow", where a gas is sent between the injector and the inner quartz tube to make the sample introduction in the plasma easier. The flow rate is usually about 1 mL min^{-1}

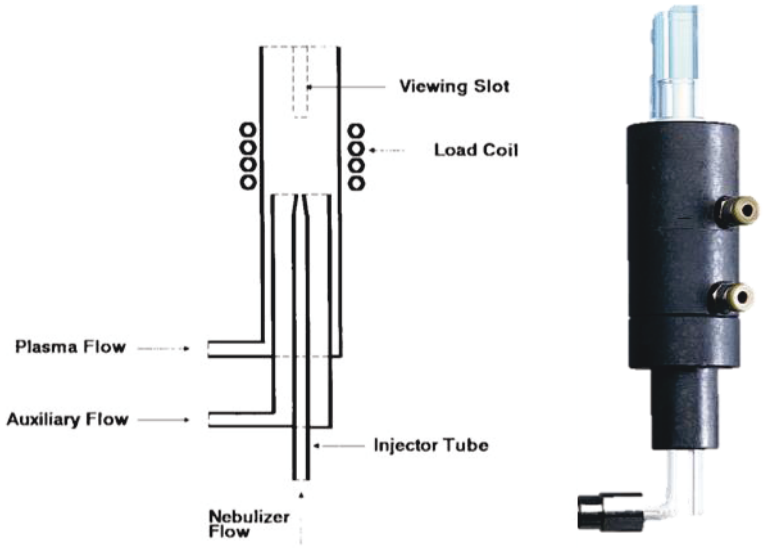

Figure 16 : Picture and schematic of the plasma torch, adapted from [123].

When the plasma is initiated and the analyte is carried through the center of the torch, the high temperatures (6000 – 10000K) will desolvate, leaving microscopic salt particles. Follows the particle decomposition into gas molecules called vaporization and finally the atomization where the molecules are dissociated into individual atoms.

Once all molecular bonds are broken, the excitation occurs. When an atom absorbs the electromagnetic radiation, one electron surrounding the nucleus will be promoted from its ground level to a higher energy state. Some elements will undergo ionization as well, the energy absorbed by the electron is sufficient so that the electron is ejected from the atom leaving behind a positively charged ion. Following the excitation process, the atom is not stable and will tend to go back to its ground level by emitting through this process a characteristic photon. The energy difference between the ground state and the higher energy level is directly correlated to the frequency of the radiation through Max Planck's equation:

$$E = h\nu \tag{3}$$

where E is the difference between the two energy levels ($E = E_{\text{excited state}} - E_{\text{ground state}}$) represented in **Fig. 17**, h the Max Planck's constant (h = 3.336 x 10^{-11} s cm^{-1}) and ν the frequency of the radiations. The wavelength λ is then easily determined by using the relationship with the speed of light [124,125]:

$$E = {}^{hc}/_{\lambda} \tag{4}$$

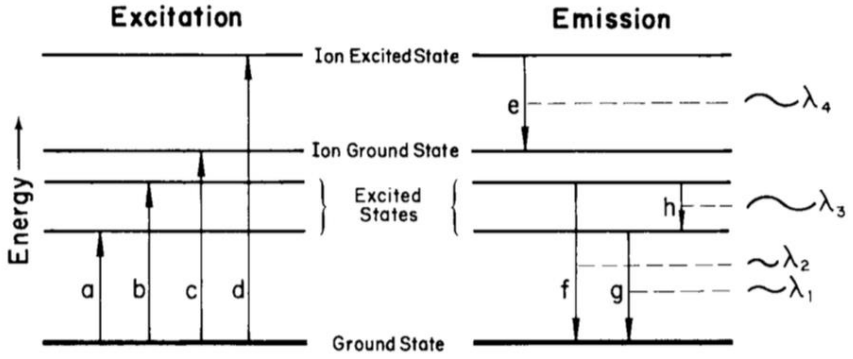

Figure 17 : Energy level diagram describing the energy transitions (related to E= $E_{excited}$ - E_{ground}) were a) and b) represent excitation, c) ionization, d) ionization/excitation, photon emission by e) ion and f) g) and h) atom [123].

The radiations, energy levels and wavelengths are characteristics to each element in the periodic table. Thus the intensity of each line is given by relation (5):

$$I = EnP \tag{5}$$

with P as the probability of the transitions per unit of time and n the initial population of electrons. On the other hand, the relationship between the initial population and the total population N of the considered ionization state is expressed by Boltzmann's law:

$$n = {gNe^{-E/kT}}/{Z} \tag{6}$$

Z is the partition function, E the excitation energy, g the statistical weight of the considered level, k the Boltzmann's constant (k= 1.38064852 x 10^{-23} J K^{-1}) and T the temperature. The intensity can be expressed by the following equation (7):

$$I = {hc\mathrm{P}\ g\mathrm{N}e^{-E/kT}}/{\lambda Z} \tag{7}$$

Finally, it is possible to establish a relationship between the intensity of wavelength and the concentration by performing a calibration. Different solutions with known concentrations are analyzed and a linear equation is obtained. This allows the determination of the majority of the elements and makes this technique very useful for elemental quantification.

2.2.4. Dispersive system

The radiations are then collected by an optical system composed of one monochromator and one polychromator, where a set of phototubes collects the photons emitted by the atoms in the plasma. The purpose of these systems is to separate all individual wavelengths collected and allows the identification of the elements without any perturbations from other wavelengths. A Czerny - Turner monochromator collects the light at one wavelength if high spectral resolution is needed as the Paschen – Runge polychromator can collect up to 30 different wavelengths at the same time (**Fig.18**). The theoretical resolution of the polychromator is 0.025 nm in the first order and 0.015 nm in the second order covering a spectral range from 165 nm to 408 nm, and the monochromator has a practical resolution of 0.005 nm

in a spectral range of 120 to 320 nm and a resolution of 0.010 nm in a range of 320 to 800 nm. The emissions are converted into electronic signals and collected by a data acquisition system.

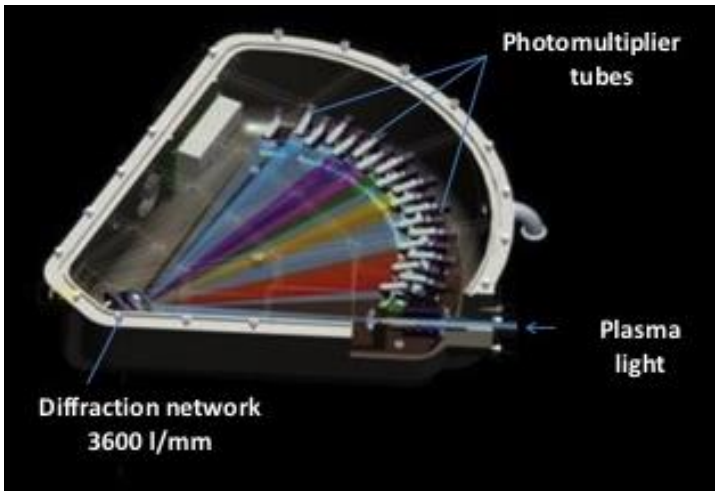

Figure 18 : Schematic representing a Pashen-Runge polychromator composed of a set of photomultiplier tubes. They can collect up to 30 different wavelengths at the same time [124].

2.3. Part C: Element quantification and AESEC data treatment

2.3.1. Concentration, flow rate and convolution.

The intensity of each emission is correlated to the concentration of the corresponding element, hence allowing their quantification through a standard calibration procedure. The concentration C_M is then given by the relationship [125]:

$$C_M = (I_{\lambda_M} - I^{\circ}_{\lambda_M})/k_{\lambda_M} \quad (8)$$

where $I^{\circ}_{\lambda_M}$ and k_{λ_M} are respectively the background intensity and the sensitivity factor for a given wavelength, λ. This technique offers a large linear dynamic range (LDR, from µg L^{-1} to g L^{-1}) and excellent detection limits for almost all the elements.

Knowing the concentration of the released elements C_M (ppm), the flow rate f (mL min^{-1}) and the exposed surface area A (cm^2), it is possible to calculate the corrosion rate v_M (mg s^{-1} cm^{-2}) of individual elements according to Equation (9):

$$v_M = f C_M / A \quad (9)$$

where it is assumed that M is not present in the initial electrolyte. The dissolution rate can also be converted into a current density, j_M (mA cm^{-2}), using Faraday's law:

$$j_M = zF v_M / M_M \quad (10)$$

with z the oxidation number, Faraday's constant F= 96485 C mol^{-1}, and the molar mass M_M (g mol^{-1}). In this work, a Horiba Jobin Yvon - Ultima 2C™ - ICP-AES was used to realize the electrolyte analysis downstream the flow cell.

The total electrical current, j_e, analyzed by the potentiostat can be expressed as the sum of the anodic and cathodic currents, j_e, j_a, and j_c respectively:

$$j_e = j_a + j_c \quad (11)$$

The AESEC allows the measurement of the soluble species of the metal dissolution which corresponds to the anodic current. When the metal undergoes only active dissolution, this current, j_a, may be expressed as:

$$j_a = \sum j_M \tag{12}$$

However, if the reaction involves dissolution and the formation of insoluble species, related to j_M^{ins}, then j_a may be expressed as:

$$j_a = \sum j_M + \sum j_M^{ins} \tag{13}$$

The quantity (Q_M^{ins}) of insoluble species may be determined by relation (14):

$$Q_M^{ins} = \int_0^t j_M^{ins}\, dt = \int_0^t (j_e - j_M) dt \tag{14}$$

when the signal collected from the potentiostat (j_e) and the data from the ICP-AES need to be compared, the ICP-AES signal (j_M) needs to be processed as j_e and j_M have very different time resolution: j_e is measured instantaneously by the potentiostat and j_M is broadened by the hydrodynamic of the flow cell. This "correction" was realized by a numerical convolution of j_e, using a transfer function h(t) which corresponds to the output signal of j_M after the application of j_e per unit of time. In the context of our AESEC experiments, the time resolution used was 1 s and h(t) can be approximated by a log-normal function according to Equation (15), in which the pre-exponential factor is a constant:

$$\text{h(t)} = \begin{cases} \sqrt{\frac{\beta}{\pi\tau^2}}\, e^{-\frac{1}{4\beta}}\, e^{-\beta ln^2 \frac{t}{\tau}} & if\ t > 0 \\ 0 & if\ t = 0 \end{cases} \tag{15}$$

where τ corresponds to the peak maximum, as illustrated in **Fig.19**. The interest of the convolution was demonstrated in several publications [115,116,126], and corresponds to the numerical application of the convolution sum to j_e:

$$j_e^*(t) = \sum_{\zeta=0}^{t} j_e(\zeta) h(t-\zeta) \tag{16}$$

where $j_e^*(t)$ represents the analyzed AESEC current, which is influenced by the cell hydrodynamics; j_e is the real current as measured by the potentiostat. With this mathematical formula, it is possible to eliminate the influence of the hydrodynamics and to accurately compare j_M and j_e.

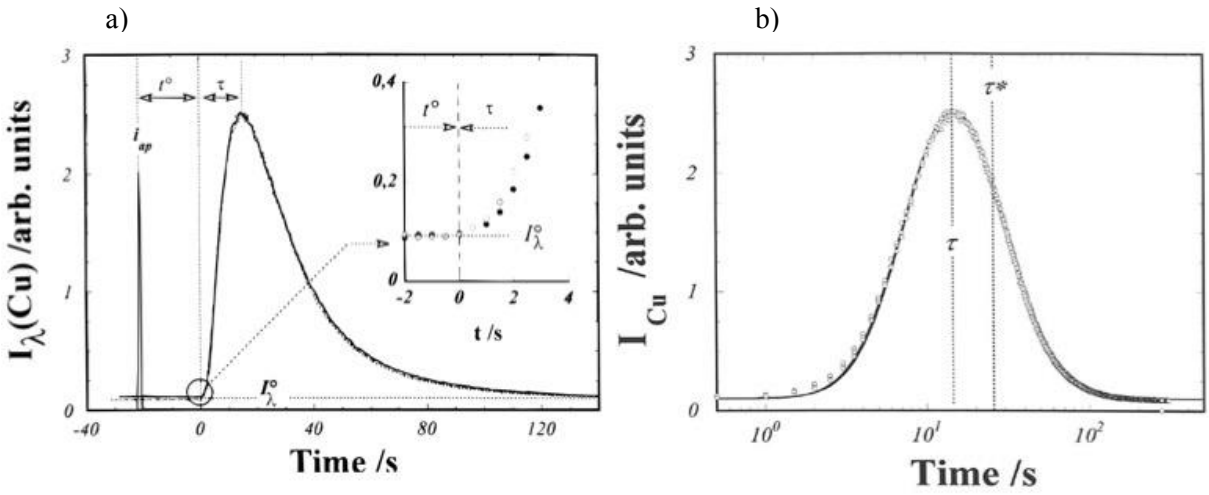

Figure 19 : a) Residence time distribution of the flow cell after applying 10 mA pulse to pure Cu in 1.2 M H_2SO_4 and the Cu intensity was measured in response. t° is defined as the time between the initial pulse and the first at which the signal rises above the background (I_λ°) and τ is defined as the time between t° and the peak maximum and b) corresponds to the curves a) with a log-normal distribution fit of I_{Cu} (adapted from [116]).

Nonetheless, this procedure takes into account the hydrodynamics of the flow cell, and not the electrochemical processes. Recently, the development of a deconvolution algorithm has been performed by Shkirskiy et al. [127] to minimize the error caused by the smoothing procedure during the convolution procedure.

2.3.2. Hydrodynamics

The concept of this work was to simulate the entire surface pretreatment process, which involves multiple steps. Therefore, unlike most previous AESEC investigations, it was necessary to change the electrolyte during the course of the experiment. The aim of this section is to report the rate of electrolyte change in the cell, when one electrolyte is substituted for another at the reservoir.

The measurement is performed by filling the cell with a 1.25 M NaOH electrolyte containing 10 ppm Al, then switching the flow over to the bypass and rinsing the capillaries with water until the Al signal had decreased down to the background level. Then the electrolyte flow is switched back to the electrochemical flow cell and the Al concentration transient is monitored as a single volume of the cell as washed downstream by water. An overlay of two concentration transients thus obtained is given in **Fig. 20** as well as the integral of the concentration transient, all shown as a function of log(t).

The result reveals that the Al is rapidly removed from the cell, as 90 % of the Al is evacuated from the cell in approximately 25 ± 2 s. From the integration of the concentration peak, it was possible to calculate the volume of electrolyte measured in this experiment as follows:

$$Q_{Al} = f \int_{t0}^{t} C_{Al}(t)\, dt = (V_{cell} + V_{tube})\, C_{standard} \quad (17)$$

where $C_{standard}$ is the standard concentration used for the experiment in ppm (10 ppm of Al) and V_{tube} the volume of the two capillaries connecting the flow cell to the FIA valve. $V_{cell} + V_{tube}$ was found to be $V_{cell} + V_{tube} = 0.26 \pm 0.02$ cm^3 with $V_{tube} = 0.07$ cm^3, so $V_{cell} = 0.19 \pm 0.02$ cm^3.

The experimental data are represented by points in **Fig. 20** The fit curve is a log-normal distribution fit to the experimental data:

$$h(t) = \begin{cases} \sqrt{\frac{\beta}{\pi\tau^2}}\, e^{-\frac{1}{4\beta}}\, e^{-\beta ln^2 \frac{t}{\tau}} & if\ t > 0 \\ 0 & if\ t = 0 \end{cases} \quad (18)$$

β and τ are empirical parameters. For this work, those parameters were found to be β = 1.90 ± 0.03 and τ =7.02 ± 0.04 yielding an increased time resolution as compared to the galvanostatic pulse measurements reported previous work and illustrated in **Fig. 21** [116].

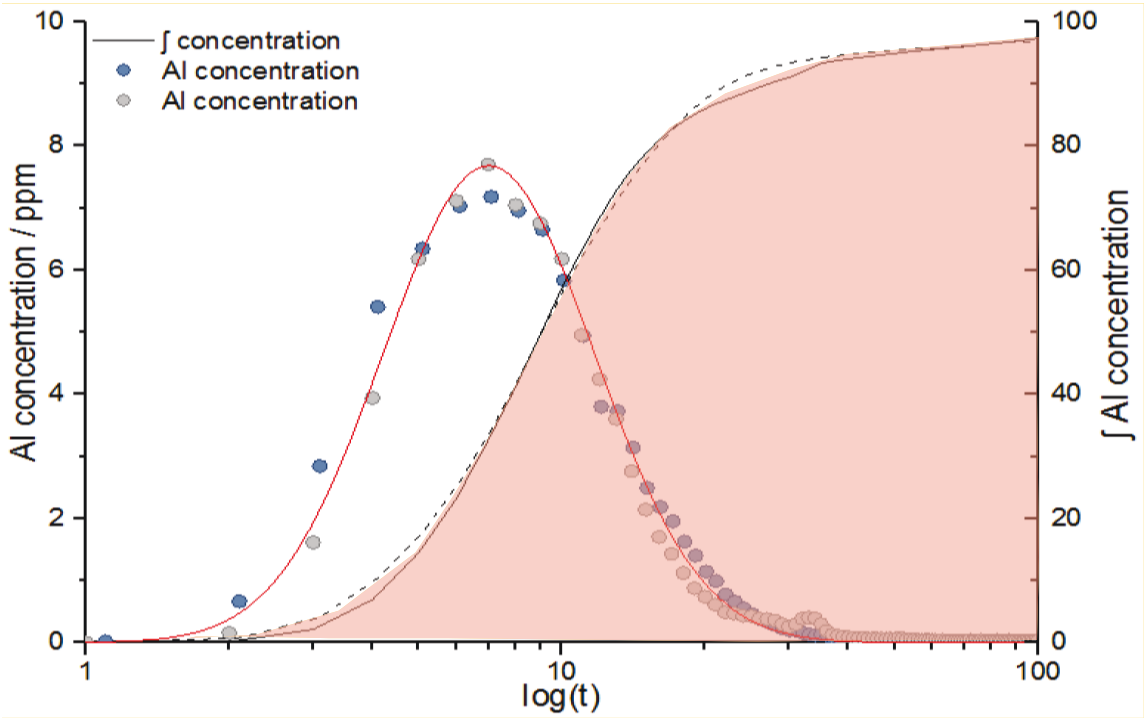

Figure 20 : Experimental data and the curve fit used to determine the residence time distribution of an electrolyte between two pretreatment steps. The curve fit is presented as a log-normal distribution with these parameters: β = 1.90 ± 0.03 and τ =7.02 ± 0.04 [128].

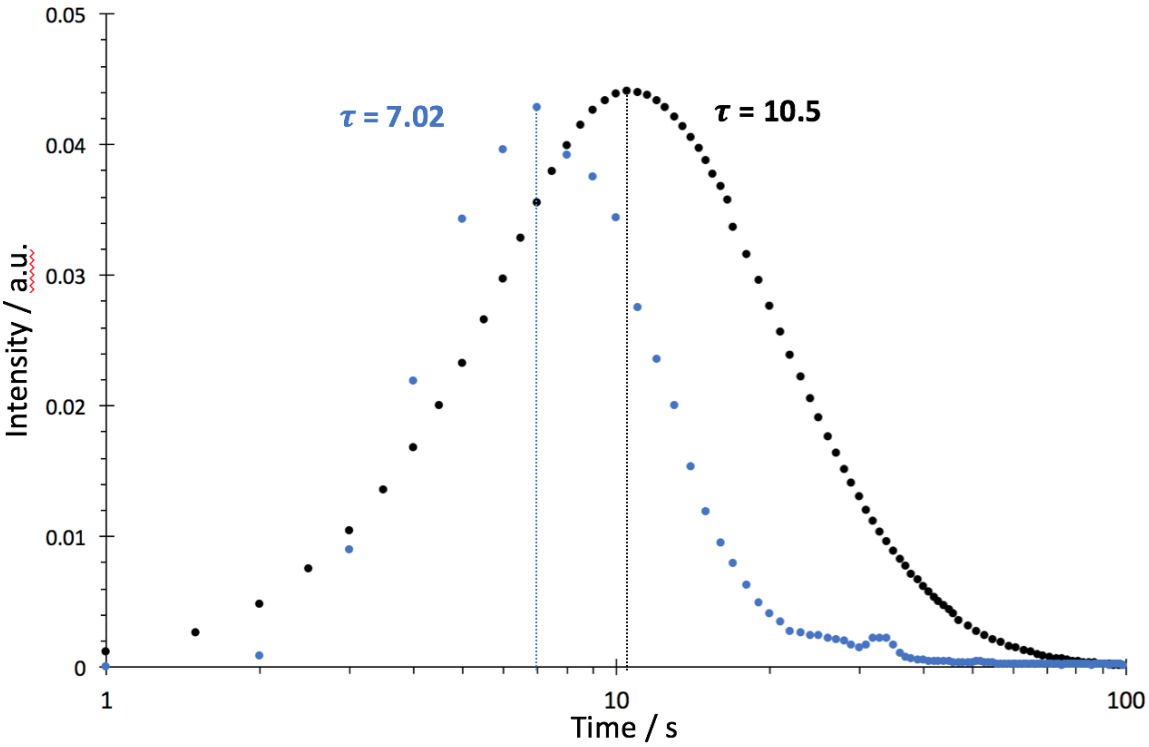

Figure 21 : Comparison of the experimental data between (in black) the galvanostatic pulse and (in blue) the hydrodynamic experiments used to determine the residence time distributions.

2.4. Sample preparation

Prior to AESEC experiments, the samples were ground with silicon-carbide (SiC) paper to a final finish of 4000 grit under ethanol, and then dried using nitrogen. Grinding the samples is not typical for surface treatment applications. In the case of our studies, we assumed that the surface exposed during the experiments was representative of the bulk alloy composition. However, numerous studies highlighted the complexity of the surface microstructure and its modification due to the rolling process. The latter creates a new surface layer-called grain refined surface layer (GRSL, mentioned in chapter I) [15] - with a different grain structure by breaking the intermetallic particles covered by an Al oxide. Thus, in order to be consistent, we tried to remove this GRSL from the surface and to be as close as possible to bulk composition. Some samples were mounted in cold epoxy resin for cross sectioning observations.

2.5. Electrochemical characterization

The electrochemical behavior of the surface is an extremely important feature when the performances of a pretreatment need to be checked. Different electrochemical methods were used during this PhD thesis and presented in the following sections.

2.5.1. Potentiodynamic polarization curves

Electrochemical reactions are the basis of metallic corrosion phenomena and can be studied to understand metal degradation. A potentiodynamic polarization involves measuring the relationship between the electrochemical potential of the working electrode and its current response. Between the

reference electrode and the working electrode, the potential is varied and the current response circulating between the working electrode and the counter-electrode is recorded. In the context of this PhD thesis the idea was to electrochemically characterize the surface before and after pretreatment. The experiments were performed with the electrochemical flow cell in order to keep the same operating parameters and the same exposed surface area. The samples were exposed to a 0.5 M NaCl at pH = 6.5 from -1.4 V to -0.3 V vs. Ag/AgCl at a scanning rate of 1 mV s^{-1} and at a 3 mL min^{-1} flow rate.

2.6. Surface ex-situ characterization techniques

2.6.1. Scanning electron microscopy (SEM)

Scanning electron microscopy is a widely used technique to study the surface morphology compositional distribution. The sample is introduced into an under vacuum chamber where a focused beam of electrons interacts with the sample. From these interactions various data can be collected:

- Secondary electrons: they give information about the surface morphology and the distribution.
- Backscattered electrons: this mode is used to obtain chemical contrast from an image. The elements with high atomic number Z will appear lighter than the elements with a low Z.
- Photons: they are produced from the interaction of electrons with the sample and are from characteristic X-rays. They are collected, analyzed and can be used to realize a mapping of the surface composition but also perform more specific analysis (particle analysis for example).

All SEM micrographs in the secondary and backscattered electron mode were taken at a 10 kV accelerating voltage and 10 mm working distance (WD) using a FEI Quanta 3D FEG 600 focused ion beam/scanning electron microscope (FIB/SEM) coupled with energy dispersive X-ray spectrometry (EDXS) realized at the Monash Center for Electron Microscopy (MCEM), Australia.

2.6.2. Focused Ion Beam (FIB)

The focused ion beam also known as FIB is a technique developed in the late 1980s, initially to perform sample preparation for transmission electron microscopy (TEM). The FIB microscope works along the same principle as the scanning electron microscope, as a focused electron beam interacts with a sample and from the scan a resulting image is obtained. Nevertheless, the FIB has also the ability to produce a high current density beam to realize *in-situ* cross sections with a size of a few micrometers. The choice of the liquid metal to generate the ion beam relies on these following requirements:

- The metal needs to wet the tip of the needle without corroding it
- It must have a low vapor pressure in the molten state

For cross sectioning, a Ga^+ ion beam is mainly used because of its low melting point which makes it a very convenient material to create a compact gun.

2.6.3. *Glow discharge optical emission spectrometer (GDOES)*

The glow discharge optical emission spectrometry is a multi-element analysis technique used for surface and interface characterization. This method gives fast analysis and is easy to use as it does not require a specific sample preparation. The sample is exposed to a plasma in a primary vacuum chamber, slowly sputtered by argon ions and neutral species accelerated into the plasma. The extracted elements are then excited by the plasma following the same principle described for the ICP-AES. From this technique it is possible to identify the nature of the material, perform quantification and determine the elemental depth distribution (**Fig. 22)**.

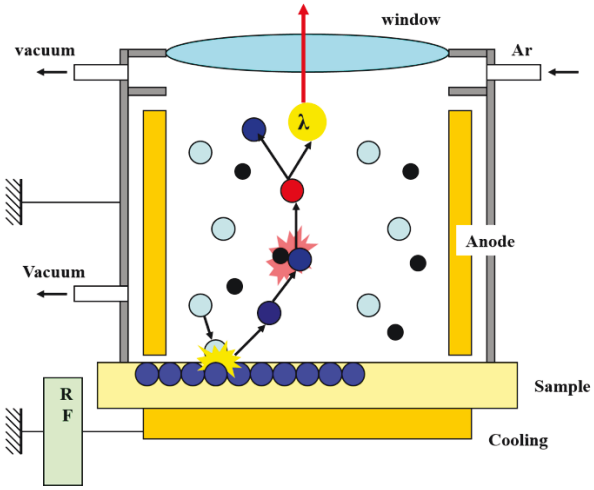

Figure 22 : Principle of Glow discharge optical emission spectroscopy.

Elemental depth profile of the film was performed using a Horiba Jobin Yvon GD profiler 2™ glow discharge optical emission spectrometer (GD-OES). The data collection was realized at 0.007 s integration time per point. During the experiment, signal of approximately 30 elements were recorded on the polychromator.

2.6.4. *Profilometry*

During surface treatment processing, one of the key parameters is the roughness of the underlying metal. The latter plays a major role in coating adhesion and therefore, corrosion protection. Roughness measurement is regularly used in surface treatment industry to control the efficacy of the pretreatment, but also for pit measurement after corrosion tests [129].

There are two different profilometers: the optical and the stylus profilometer. Optical profilometer is a non-contact method, providing 2D and 3D images of a surface with high resolution (up to 0.2 nm for height resolution), also numerous roughness characteristics. A light beam is produced and projected to the sample surface. Through the interferometer, half of the incident beam will be reflected from a reference and the other half will be reflected from the sample. Then, they finally recombine to produce interference fringes and the system records the intensity of each point on the surface as the scanning goes downwards.

The stylus profilometer uses a tip to scan the surface, physically moving along the surface to measure its height. The changes in the z- position (in the direction normal to the surface) gives the surface profile, which can be given by the software.

Surface topography (roughness, depth of attack) was characterized using a Veeco Wyco NT1100 Optical profilometer and a Veeco Dektak 150 stylus profilometer. In the context of this PhD thesis, the profilometry technique was performed as complementary test to check the etch rate determined by the AESEC calculations.

2.6.5. X-ray photoelectron spectroscopy (XPS)

X-ray photoelectron spectroscopy (XPS), is a characterization tool used for extreme surface analysis (5-10 nm). It gives access to the composition of the sample as well as the oxidation state of the element present on the surface. The principle relies on the irradiation of the sample with a X-ray beam generated by an electron gun bombarding a metallic target. As a consequence of this photon irradiation, the atoms of the surface of the sample will ionize by a photoelectric effect. The excited atoms will emit photoelectrons during their relaxation and their kinetic energy E_k is measured. According to Einstein's relation, the characteristic binding energy E_b can be calculated:

$$E_b = h\nu - (E_k + \phi) \quad (11)$$

where $h\nu$ is the energy of the photon from the X-ray source and ϕ the energy required to extract the electron from vacuum which depends on the spectrometer (considered as negligible for the calculations). XPS is used to determine surface composition and the thickness, contamination level, or the chemical state of elements and their local bonding environment.

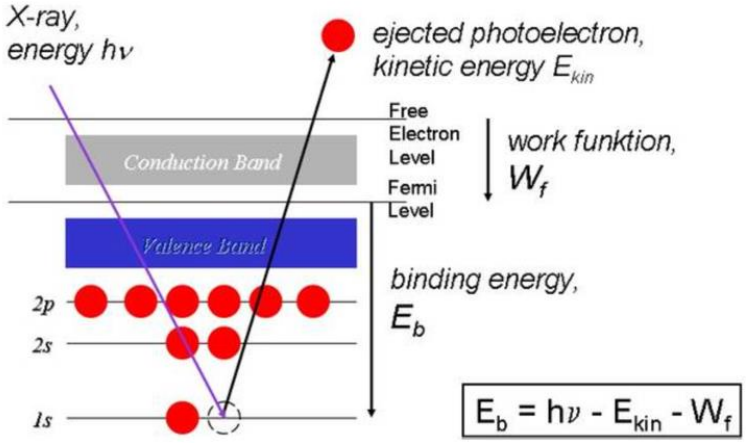

Figure 23 : Principle of X-ray photoelectron spectroscopy.

2.6.6. Vibrational spectroscopy

Raman spectroscopy

When a light interacts with a molecule, it can be either transmitted, absorbed, reflected or scattered. In Raman spectroscopy, the sample is irradiated with a monochromatic laser beam, the latter will interact with the molecules on the sample and produced a scattered light. The Raman effect represents

approximately 10^{-7} of the scattered light and its frequency is different from the incident laser beam (inelastic scattering). This change in wavelength is induced by the interaction of the light and molecular vibrations which provides chemical and structural information on the analyzed sample. Depending on the vibrational state of the molecule, the Raman shifted light can be either at a higher or lower energy state. Raman spectroscopy was used herein as a complementary tool to the X-ray diffraction (XRD), in order to identify the amorphous products.

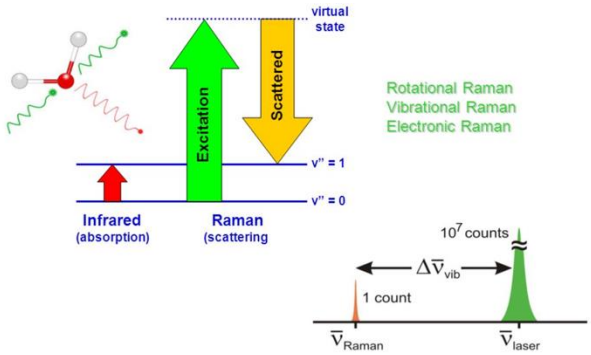

Figure 24 : Principle of Raman spectroscopy.

Surface observation and film composition were investigated using a Renishaw Invia confocal Raman microscope with excitation by a Co diode Pumped Solid State (DPSS green laser 532 nm) and an edge filter focused on 1000 cm^{-1}. The exposure time was 1s and 50 accumulations were realized for each spectrum.

Infrared (IR) spectroscopy

Infrared spectroscopy gives access to the chemical nature of the bonds present on a sample. A sample is irradiated with an infrared light source which is sent to a modulator that separates the light into numerous wavelengths. A detector then collects and determines the quantity of absorbed IR light by the sample. Finally, by data processing, a spectrum is obtained, which gives access to the vibrational frequencies of chemical bonds between two atoms. During their radiation, the molecules are prone to the change of their dipole moment. From their ground level state, their vibrational energy level is transferred to a higher level called excited state.

Infrared spectra were obtained from the corrosion product using a Nicolet 6700 IR spectrometer equipped with an ATR (attenuated total reflectance) accessory including a diamond crystal. This latter was used to permit the analysis of thin layers on substrate without specific sample preparation. The spectrometer is equipped with a nitrogen-cooled MCT (mercury-cadmium-telluride) wide band detector. For each spectrum, 256 scans were recorded in the wavelength range from 600 to 2000 cm^{-1} with a nominal resolution of 2 cm^{-1}. Moreover, the background was collected on the ATR accessory without any substrate pressed against the crystal.

2.6.7. X-ray diffraction (XRD)

X-ray diffraction is a characterization methods used to determine the structural properties of crystalline materials. This technique allows the identification of crystalline structure, indexation and quantification of the crystalline phases present in the materials. Moreover, it gives access to specific features such as lattice refinement, grain size and their orientation or the deformation of the crystalline network could be also determined. The principle relies on the interaction of a monochromatic X-ray at a chosen wavelength on the surface of the sample and an incident angle θ. The beam is reflected by reticular planes {h, k, l}, separated by an inter-reticular distance d, of the crystalline sample. The radiation will provoke the vibration of atoms at the same frequency of the X-ray radiation and spread them in all directions. Depending on their direction, the atoms arranged in the crystal may undergo constructive or destructive interferences. The constructive interferences or diffraction peaks are determined by Bragg's law, as mentioned and illustrated in **Fig. 25**.

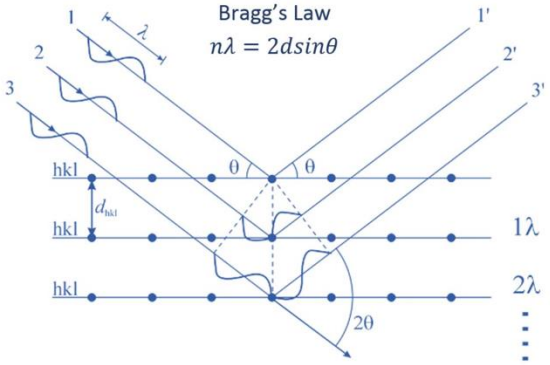

Figure 25 : Principle of X-ray diffraction.

Consequently, through the angular position, the intensity and the shape of the diffracted lines, it is possible to have access to:

- The geometry of the crystal, the size and the shape of the lattice
- The type of atoms involved and their arrangement in the lattice along with their crystallographic orientation,
- The size of the particles and their deformation.

During this PhD, the analysis was performed using a PANanalytical X'Pert PRO diffractometer operating with Cu Kα radiation (λ=1.54050 Å), at 40 kV and 45 mA with a PIXcel detector. The data collection was carried out with an angular resolution of 0.02° and a scan rate of 0.3 s per point.

CHAPTER III: *IN SITU* MONITORING OF ALLOY DISSOLUTION AND RESIDUAL FILM FORMATION DURING THE PRETREATMENT OF AL-ALLOY 2024-T3.

« Le trop d'expédients peut gâter une affaire ;
On perd du temps au choix, on tente, on veut tout faire.
N'en ayons qu'un, mais qu'il soit bon. »

« Expedients may be too many ;
consuming time to choose and try.
On one, but that as good as any,
It is best in danger to rely. »

Jean de La Fontaine. Le Chat et le Renard. Livre IX, Fable 14.

In situ monitoring of alloy dissolution and residual film formation during the pretreatment of Al-alloy AA2024-T3.

O. Gharbi[1], N. Birbilis[2], K. Ogle[1], *

[1] Chimie-ParisTech, PSL Research University, CNRS - Institut de Recherche Chimie Paris Paris 75005, France

[2] Department of Materials Science and Engineering, Monash University, VIC 3800, Australia

The dissolution of intermetallic phases in AA 2024-T3 aluminum alloy sheet was investigated during a coating pretreatment sequence. The atomic emission spectroelectrochemistry (AESEC) technique was used to quantitatively measure the dissolution rates of individual alloying elements during a complete pretreatment sequence. The results demonstrate the significant selective dissolution of Al in 1.25 M NaOH, leading to the enrichment of alloying elements such as Cu. Subsequent 2.8 M HNO_3 treatment contributes towards dissolving the excess residual layer and passivates the alloy matrix, however the presence of a residual Cu layer at the alloy surface was evidenced. The real-time alloy dissolution profiles are presented herein, and discussed in the context of the surface morphology via microscopy.

This article was published in The Journal of the Electrochemical Society

1. INTRODUCTION

The surface treatment of aluminum (Al) alloys is required prior to the application of corrosion protective coatings [130]. Protective coatings are essential in order to allow microstructurally complex alloys, which are nominally prone to localized corrosion [8,21,29,56,131,132], to be used in service; particularly in aerospace applications [5]. Coatings for Al-alloys are nominally multilayered coating 'systems', with the first coating being a chemical conversion coating. The surface treatment prior to this chemical conversion coating is as important as the coating itself, since it determines the efficacy of any conversion coating[82,130]. Such surface treatment, often termed pre-treatment, generally involves alkaline etching and acid pickling. Sodium hydroxide (NaOH) is often used to remove any organic residue and also to remove several micrometers of the alloy surface[81]. This is followed by acid pickling, usually performed in nitric acid (HNO_3) to remove any residue, products, films, or particles remnant from – or caused by - the prior alkaline step. The purpose of surface pretreatment is to provide a chemically homogeneous surface chemistry prior to subsequent coating processes. The chemical heterogeneity of the Al-alloy surfaces **is** due to the many alloying elements present, such as copper (Cu), magnesium (Mg), iron (Fe) and manganese (Mn). Cu improves the mechanical properties of AA 2024-T3 [6] however decreases corrosion resistance due to stimulating various phases which serve as local electrochemical entities, in addition to raising the alloy potential to above the pitting potential of the matrix phase [2,19,21,47,133,134]. This element is considered to be a major contributor to the localized corrosion of Al [49,131,135] and its elimination is one of primary goals of aluminum alloy surface pretreatment.

Knowledge of the elementary dissolution kinetics during the pretreatment sequence would be very useful for the development of surface treatment formulations, however, this information is often very difficult to obtain. *In situ* monitoring of the corrosion reactions during surface treatment is difficult as the corrosion reactions occur within a relatively short time with large reaction rates and may involve extensive precipitation of dissolution products and/or particle release.

Chemical pretreatments and their effect on coating performance have been studied for various Al-alloys [16,83,90–92,99,136–138] and it has been noted that these pretreatments can lead to surface enrichment of certain alloying elements such as copper [49,93,94,104,139]. On the other hand, Hughes et al. studied the effect of various deoxidizing agents, like nitric acid (HNO_3), sulfuric acid (H_2SO_4), phosphoric acid (H_3PO_4) or hydrofluoric acid (HF) using *ex situ* surface characterization – scanning electron microscopy (SEM), transmission electron microscopy (TEM), X-ray photoelectron spectroscopy (XPS) and Rutherford back scattering (RBS) - and concluded that only the HNO_3 treatment combinations produced a surface free of copper-rich smut [103]. However, Liu et al. [104] observed copper enrichment after HNO_3

immersion via RBS and TEM analysis, similar to the extent obtained from NaOH immersion. Using XPS, Moffit et al. [97] measured a thin residual copper layer beneath an Al oxide film after pretreatment in a nitric acid based oxidizer. Muster et al. [14] concluded that two main considerations should be taken into account in the point of view of surface enrichment of alloying elements: (i) the so-called etch rate of the metal finishing solution, and (ii) the solubility of the alloying elements in that solution. These considerations were suggested to be considerations for evaluating pretreatment performance.

Nevertheless, despite all surface characterization performed after pretreatment to date, the kinetics of the metal / electrolyte reactions during the process need to be clarified. In order to do this, an in situ methodology is required, as methods to date involve analysis ex situ of the pretreatment electrolyte, and analysis subsequent to the pretreatment process. The aim of the present work is to demonstrate the utility of atomic emission spectroelectrochemistry (AESEC) to monitor the kinetics of Al alloy surface pretreatment (which is possible at open circuit using AESEC) in terms of alloy dissolution, residual film formation, and particle release[111]. AESEC analysis of surface treatment processes have been previously performed in the context of chromating, phosphating, degreasing or anodization [113,118,140–142]; however the works to date have involved only single step treatments and comparatively low dissolution rates. The novelty of the work herein as concerning AESEC is to combine two different steps with respect to electrolyte exposure, and to analyze a system experiencing significantly rapid dissolution rates. In addition to this, AESEC is the only quantitative method capable of providing element-by-element dissolution analysis (and real dissolution rates) under open circuit conditions. The study is focused on aluminum alloy AA2024-T3.

2. EXPERIMENTAL

Materials Commercial AA2024-T3 aluminum alloy sheet (2 mm thick) was supplied by Constellium . The corresponding elemental analysis is given in **Table 8**. Immediately prior to experiments, the samples were ground with silicon-carbide (SiC) paper to a final finish of 4000 grit under ethanol, and then dried using nitrogen. The purpose of grinding is to two–fold: to produce a surface representative of the bulk alloy composition, assumed in later calculations, and to remove the grain refined surface layer (GRSL) [15] associated with the manufacturing process - such as rolling [143]. All chemicals used herein were reagent grade and solutions were prepared from 18.2 MΩ cm water purified with a Millipore™ system.

Table 8: Elemental composition of AA2024-T3

AA2024T3	*Al*	*Cu*	*Mg*	*Mn*	*Fe*	*Si*	*Zn*	*Ti*	*Cr*	*Ni*	*Zr*
composition wt %	bal	4.21	1.38	0.48	0.13	0.066	0.12	0.023	0.0051	0.0059	0.0138

AESEC method **Fig. 26** illustrates the experimental set-up used for this work. The AESEC system is a combination of i) an electrochemical flow cell where the sample is exposed to the electrolyte, and a downstream ICP-AES spectrometer. The method has been described in detail previously [111] : the ICP-AES **s**pectrometer is used to continuously analyze the elemental composition of the electrolyte exiting the flow cell. The alloy dissolution occurring as a result of exposing the sample to the electrolyte leads to the formation of dissolved species, which are carried to the ICP spectrometer. The concentrations of the released elements, C_M, are monitored as a function of time to give the elemental dissolution rates (v_M) of the alloy components:

$$v_M = C_M f / A \quad (1)$$

where f is the electrolyte flow rate passing through the cell and A is the exposed surface area of alloy. In some cases, it is convenient to express the dissolution rate as an equivalent current density assuming Faraday's law as:

$$j_M = zF v_M \quad (2)$$

where z is the oxidation state of the dissolved species.

A valve developed for flow injection analysis (FIA), was used to route the electrolyte either through the cell or through a bypass. The latter is used for standards during the calibration procedure. The FIA valve (from FIALab) was made from Kel-F(CTFE)™ for the stator material and Valcon M™ for the rotor, materials chosen for their good chemical resistance to nitric acid. The flow cell has a separate compartment for the reference and the counter electrode (Pt foil) separated from the main compartment by a porous membrane of natural cellulose. This

was chosen for its good resistance to nitric acid at room temperature**.** In fact, no deterioration of any part of the cell was observed during the course of experiments herein.

A second peristaltic pump was used to inject 2.8 M nitric acid containing 15 ppm Y as an internal standard into the electrolyte flow immediately after the flow cell at 1 mL min $^{-1}$. Nitric acid was used to neutralize NaOH solution thereby making it easier to detect elements, which are otherwise insoluble in alkaline solution, such as Mg, and Cu. **Fig. 26** also shows the electrolyte introduction system for the ICP which consists of a TR-30-K3™ Meinhard nebulizer especially used for high solid content electrolytes and a cyclonic aspiration chamber. The efficiency of nebulization is about 5 to 10% while the remainder of the electrolyte is removed by a third peristaltic pump and may be subjected to subsequent chemical analysis.

The flow rate in the cell was precisely measured before each experiment and was 3.01 ± 0.02 mL min^{-1}. The exposed surface area was 0.87 ± 0.07 cm^2 based on image analysis of the attacked surface. Further experimental details concerning the exchange rate of electrolytes in the flowcell and the surface topography of the attacked zone are given in the Appendix. The electrolyte in the reservoir was maintained at a constant temperature with a water bath and the temperature was also controlled at the backside of the sample by placing it in contact with a hollow copper block, not shown, which was connected to a recirculating temperature controlled water bath.

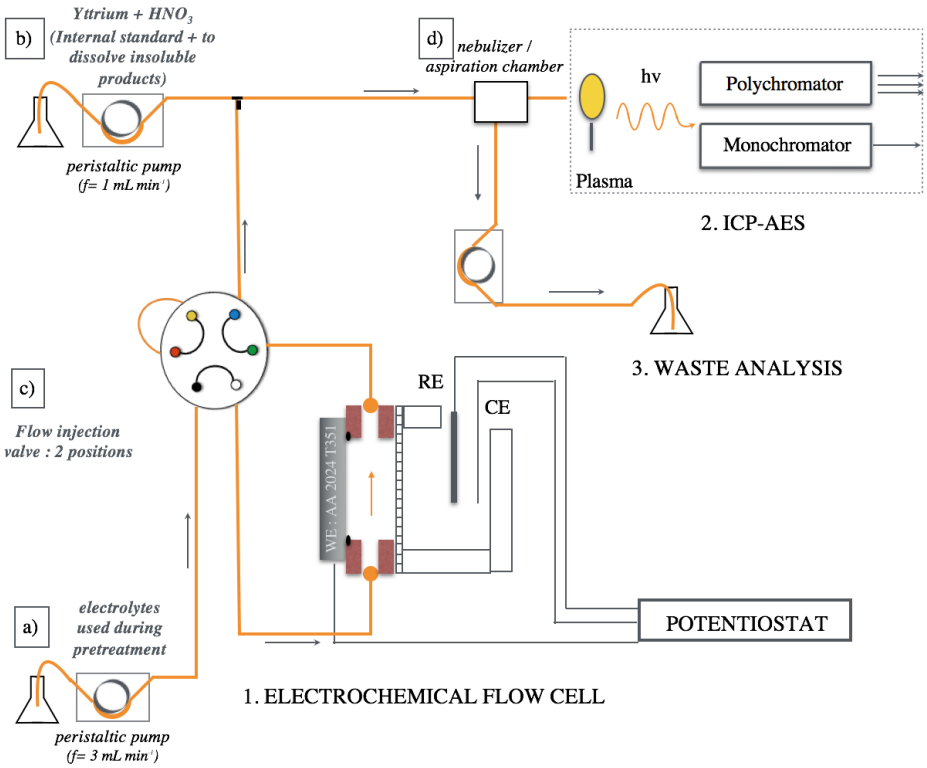

Figure 26: Schematic of the experimental set-up showing: the electrochemical flow cell, two pumps with their electrolyte reservoir a) and b), a flow injection valve c) connected to the electrochemical flow cell. The ICP-AES collects the electrolyte to measure the dissolution rates and the potentiostat follows the electrochemical data. b) Injects 2.8 M HNO3 with 15

ppm Y after the flow cell at 1 mL min $^{-1}$. d) represents the nebulizer and aspiration chamber system which collects ~ 5 % of the electrolyte to inject it in the plasma. The remaining 95 % were collected downstream. A recirculating temperature controlled water bath and a hollow copper block (not shown here) were used to maintain the electrolyte and the sample at a constant temperature (60 °C).

Instrumentation The ICP-OES spectrometer used was an Horiba Jobin Yvon Ultima 2C consisting of a 50 cm focal length Paschen-Runge type polychromator with an array of photomultiplier tube detectors at chosen wavelengths and a monochromator. The emission wavelengths for Al, Cu, Mg, Fe, Mn and Ti and their detection limits ($C_{2\sigma}$) - defined as three times the standard deviation of the blank solution divided by the sensitivity factor - are reported in **Table 9**. Calibrations were performed for each electrolyte used. The electrochemical experiments (open circuit potential and polarization curves) were executed using a Gamry Reference 600™ potentiostat with an Ag/AgCl saturated reference electrode and a Pt wire counter electrode.

Microscopy and Surface Topography Surface topography (roughness, depth of attack) was characterized using a Veeco Wyco NT1100 Optical profilometer and a Veeco Dektak 150 stylus profilometer. The surface of the alloy was characterized before and after the experiment using an FEI Quanta 3D FEG 600 focused ion beam/scanning electron microscope (FIB/SEM) coupled with energy dispersive X-ray spectrometry (EDXS). Some samples were crossed sectioned (using a focused Ga ion beam) for analysis of the surface profile via SEM.

Table 9 : Detection limits (C2σ) of the different elements in all electrolytes.

Element	*Wavelength, nm*	*$C_{2\sigma}$ in NaOH, ppb*	*$C_{2\sigma}$ in water, ppb*	*$C_{2\sigma}$ in HNO_3, ppb*
Al	396.152	7.3	9.1	9.3
Mg	279.079	Not soluble in NaOH, measurements realized in water	2.1	1.3
Cu	324.754		2.7	2.2
Mn	257.610		2.4	2.7
Fe	259.940		2.3	2.2
Ti	337.280		2.3	2.2

3. RESULTS AND DISCUSSION

3.1. In situ measurement of AA2024 pretreatment kinetics

The entire pretreatment sequence including: (1) treatment in 1.25 M NaOH at 60 °C, (2) deionized water rinse, (3) treatment 2.8 M HNO_3 at 25°C, and (4) deionized water rinse, was performed while monitoring the dissolution rate of the alloy components. **Fig. 27** reveals the variation of the Al and Cu dissolution rates as a function of time during pretreatment process, as well as the open circuit potential. Note that the Cu signal has been multiplied by 500 during the NaOH treatment and water rinse periods of the experiment, demonstrating that Cu dissolution is relatively negligible during this period. Cu and Al dissolution occur at a similar order of magnitude during the HNO_3 dissolution step and have been multiplied by 10 for clarity.

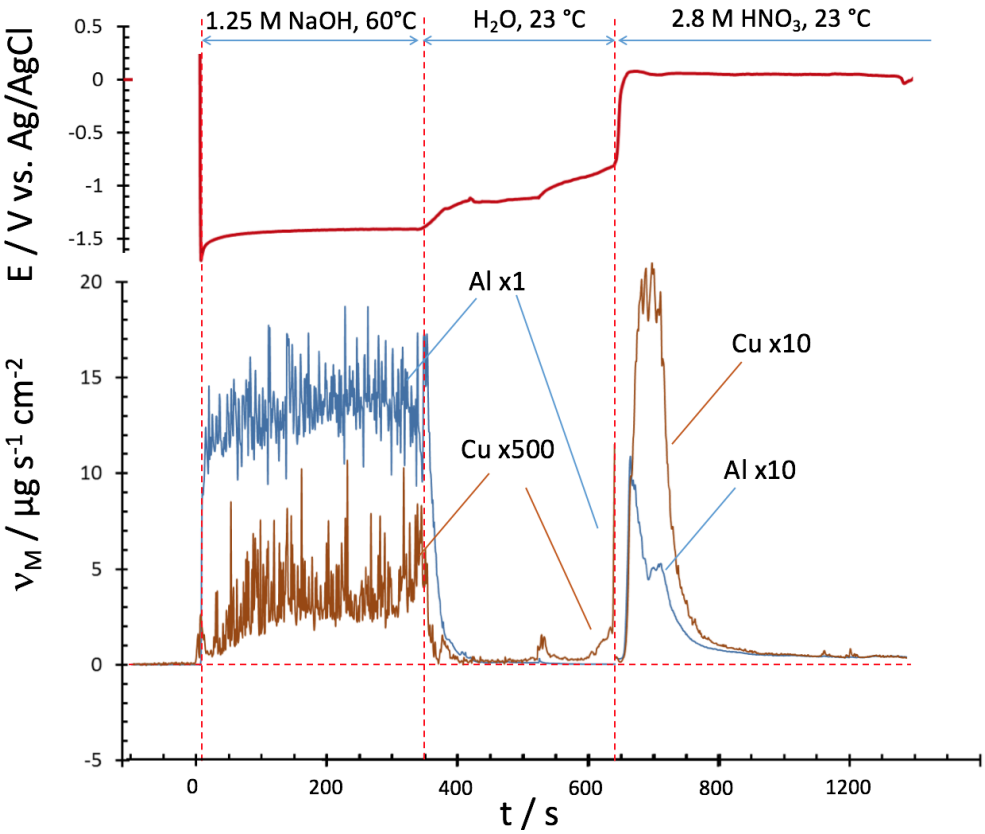

Figure 27: AESEC dissolution profiles for Al and Cu and the electrochemical potential during the pretreatment sequence of AA2024 – T3. Exposure to 1.25 M NaOH at 60 °C begins at t=0 indicated with a dashed vertical line. This was followed by water, and then 2.8 M HNO_3 both at ambient temperature (≈ 23 °C). Note the indicated multiplicative factors for the two elements in the different regions of the curve. Also the time axis is broken to give the dissolution rates obtained after a longer time period.

During the first (NaOH) step, the Al dissolution rate rises rapidly to reach a steady state value of ~13.4 ± 1.6 µg $s^{-1}cm^{-2}$ in the Figure. The NaOH experiment was repeated three times and the average value was found to be 14.2 ± 0.7 µg $s^{-1}cm^{-2}$, demonstrating the good reproducibility of the experiment. The open circuit potential drops to ~-1.7 V vs. Ag/AgCl and then rises rapidly

to obtain a steady state value around -1.4 V vs Ag/AgCl**.** The dissolution rate curve shows extensive oscillations, due to the evolution of hydrogen gas during the experiment (with water reduction to form hydrogen being the favored reduction reaction at the corresponding potentials). The high dissolution rate observed and the negative potential are consistent with Al in the active state [2,144].

In 1.25 M NaOH, the dissolution rates of Cu (and Mg, Fe, Ti, Mn, although not shown in Fig. 27) were negligible compared to the dissolution rates expected for congruent dissolution of the alloying components relative to the bulk alloy composition. For example, the expected dissolution rate for Cu was 0.6 µg s^{-1} cm^{-2}, 0.2 µg s^{-1} cm^{-2} for Mg and 68 ng s^{-1} cm^{2} for Mn. Therefore, it may be assumed that an appreciable proportion of the alloying elements remain on the surface as a residual film during the exposure of AA2024 to 1.25 M NaOH at 60°C.

The transition from the NaOH solution at 60 °C and the deionized water at 23°C is marked by a slow increase in the open circuit potential rising to approximately -1.1 V vs. Ag/AgCl and a significant decrease of Al dissolution rate over the course of about 80 to 100 s. During the HNO_3 pretreatment period we observe a peak of Al dissolution followed by a peak of Al and Cu dissolution, where the Cu dissolution rate is ~2 times higher than the Al dissolution rate. This suggests that Cu dissolution is favored during this period. The other elements (Mg, Fe, Mn and Ti) are discussed later. Following this relatively short-lived transient, passivation of the alloy surface is indicated by the Al dissolution being reduced to 30 ng $s^{-1}cm^{-2}$ and Cu dissolution at 15 ng $s^{-1}cm^{-2}$. These values expressed as equivalent current densities, using Faraday's law, would correspond to 320 and 45 µA.cm^{-2} respectively (assuming n=3 for Al and n=2 for Cu).

The data in **Fig. 27** may also be presented in integral format to determine the cumulative change in mass due to the dissolution of Al, Q_{Al}.

$$Q_{Al} = -\int_0^t v_{Al}\, dt \tag{3}$$

This value is shown in **Fig. 28** as a function of time. Assuming that the alloy composition is uniformly distributed in depth at t=0, the quantity of residual Cu, Q_{Cu}, may be determined by a mass balance in Equation 5:

$$Q_{Cu} = -xQ_{Al} - \int_0^t v_{Cu}\, dt \tag{4}$$

where $x = {}^{Cu\ w\%}/_{Al\ w\%}$ = 0.045 the ratio determined from the bulk alloy composition given in Table 1. (This value was redetermined as x = 0.042 in our laboratory by ICP-OES analysis). Q_{Cu} is also shown as a function of time in **Fig. 28**. A large Al mass loss occurs during the NaOH exposure, reaching a value of -4.89 mg cm^{-2} after only 5 min, corresponding to an enrichment of Cu of approximately 220 µg cm^{-2}. Assuming the standard density of Al and a uniform distribution of the reaction on the surface, the quantity of Al dissolved would

correspond to 18.2 µm in good agreement with the crater depth measured by profilometry of ~19 µm (Appendix). Those values remain stable during the water rinse for both elements. However, on contact with the HNO_3 electrolyte, the Q_{Cu} decreases markedly to reach a steady state value after 1300 s, corresponding to an excess Q_{Cu} of 70.0 µg cm^{-2}. It is noted that the quantity of Al dissolved during the HNO_3 treatment (- 57 µg cm^{-2}) is very small compared to that dissolved during the NaOH treatment. This indicates that the majority of Al oxidation occurring during the NaOH treatment leads to soluble Al cations, with only a minor amount remaining on the surface as a film.

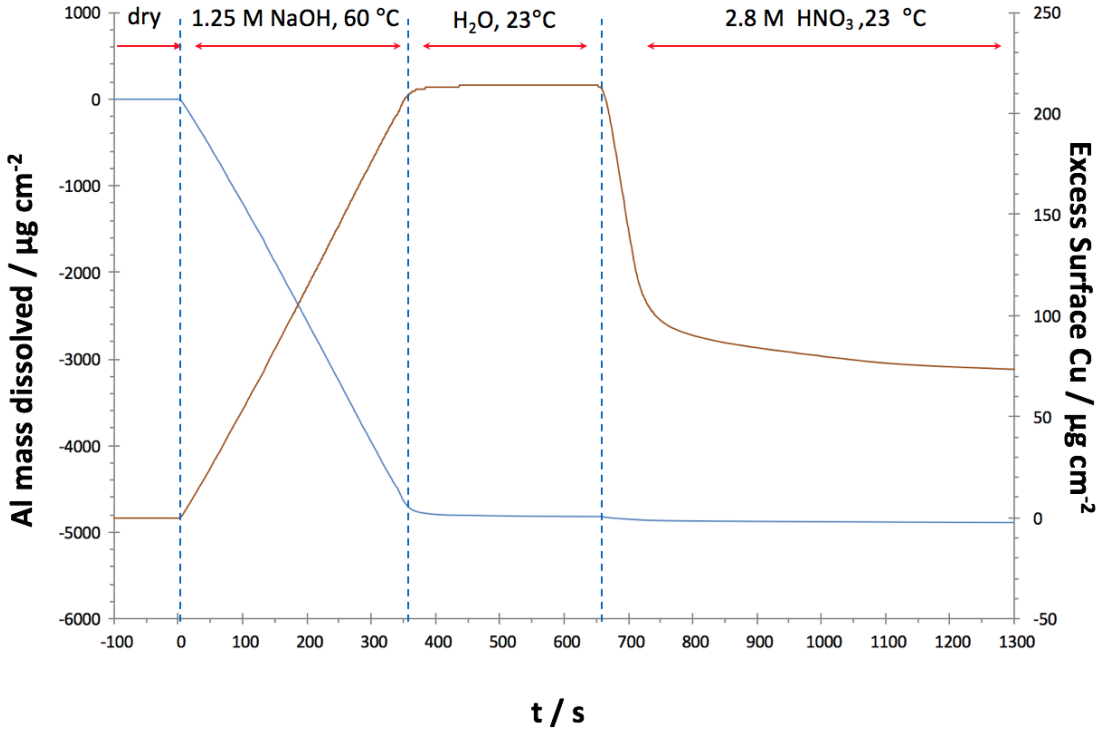

Figure 28 : The formation and dissolution of the residual film: showing the evolution of the Al mass loss and the residual Cu calculated from mass balance - during the pretreatment sequence. The quantity of residual and final Cu, Mg, Fe, Mn, and Ti are given in Table 3.

The total quantity of Cu dissolved in NaOH is only 2.5 µg cm^{-2} as compared with **150** µg cm^{-2} in HNO_3. It is noted that $\square_{Cu}$ in NaOH may be theoretically underestimated if undetected Cu rich particles are too large to be measured efficiently by ICP-OES [117,145]. To determine this, the quantities of Al and Cu released during the NaOH exposure were measured by collecting the electrolyte downstream from the plasma (**Fig. 26**). It was found that 4.28 mg cm^{-2} of Al was obtained as compared to 4.82 mg cm^{-2} determined from integration of the ICP-OES concentration transient, yielding a nebulization efficiency of 11.5%. The quantity of Cu was 3.7 µg cm^{-2} as compared to 2.5 µg cm^{-2} by integration of the concentration transient. Accounting for the nebulization efficiency of 11%, it appears that 61% of the Cu was detected during the NaOH treatment. However, the rate of Cu dissolution is very low and even considering the

corrected dissolution rate, it remains negligible as compared to the 220 µg cm^{-2} formed by selective dissolution of Al as determined by mass balance.

3.2. Microstructural analysis of pretreated surfaces

Fig 29. gives a general overview of the AA2024-T3 at a relatively low magnification (1500x) to reveal the surface modifications at stages of the pretreatment. **Fig 29a** represents the general AA2024 surface morphology before the experiment, illustrating the presence of intermetallic particles at the surface and the chemical heterogeneity of AA2024-T3 at the length scale examined. The larger of the observed particles correspond to constituent particles, which are irregularly shaped, with size up to ~10 µm[11]. Such particles do not contribute to improved mechanical properties of the alloy[6]. The constituent particles do not metallurgically dissolve in response to heat treatment, and contain impurity elements such as Fe and Si, however some typical constituent particles in 2xxx series Al-alloys, where Cu is present, also include Al_7Cu_2Fe, $Al_{12}(Fe,Mn)_3Si$, $Al_6(Cu,Fe)$, Al_2CuMg, Al_2Cu[6]. The NaOH treatment significantly altered the surface leaving an attacked surface structure with surface cracks evident, and particles of different shape and size. (**Fig. 29 b**). Probably all of these cracks may have occurred during dehydration of surface products under vacuum, although when the cracks occurred is not really relevant on the basis that the surface morphology is that of extensive attack. The morphology of the attacked surface layer in Fig 4b, is however, significantly altered following the HNO_3 treatment, presenting a rather severely etched surface with some remaining intermetallic particles (**Fig. 29 c)**.

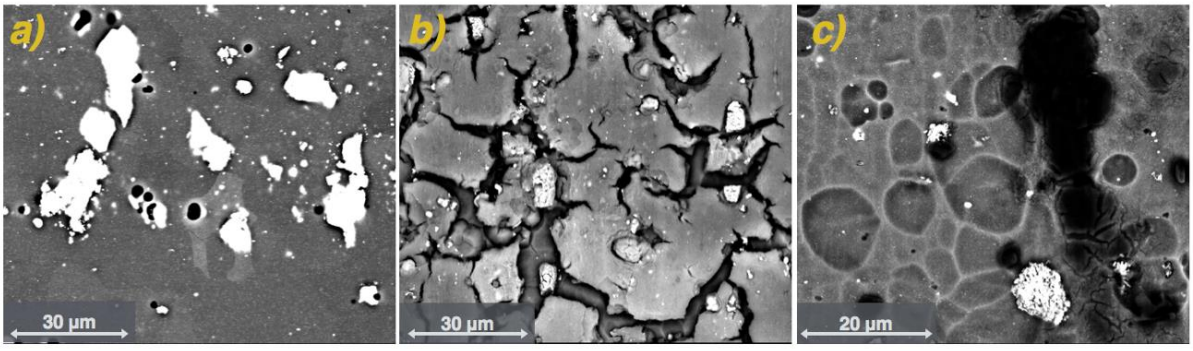

Figure 29 : SEM of AA2204-T3 showing (A) initial surface, (B) after 1.25 M NaOH at 60 °C for five minutes, (C) after 2.8 M HNO_3 for 15 minutes (backscattered electron images - FEI Quanta 3D FEG).

After NaOH etching, EDXS and mapping were carried out on the surface, including some intermetallic particles in order to identify the surface distribution of elements. **Fig. 30** illustrates a typical SEM micrograph represented in secondary (ii) and backscattered (i) electron mode with the corresponding mapping. These micrographs show the presence of two particles

protruding from the surface, labeled as iii) and iv). EDS spectra and mapping indicate that the phases conform to what may be S-phase (Al_2CuMg) and Al_7Cu_2Fe. Al was selectively dissolved from the matrix when exposed to NaOH, but it was also shown that Al could selectively dissolve from the intermetallic particles themselves (namely Al_7Cu_2Fe). This was revealed from EDS mapping, in particular for the particle labeled iv). Similar results concerning selective dissolution have been reported by Lunder et al. [16]; whereby after NaOH exposure, most of the alloying elements, such as Fe and Mn, remained in the enriched layer, while Al was dissolved.

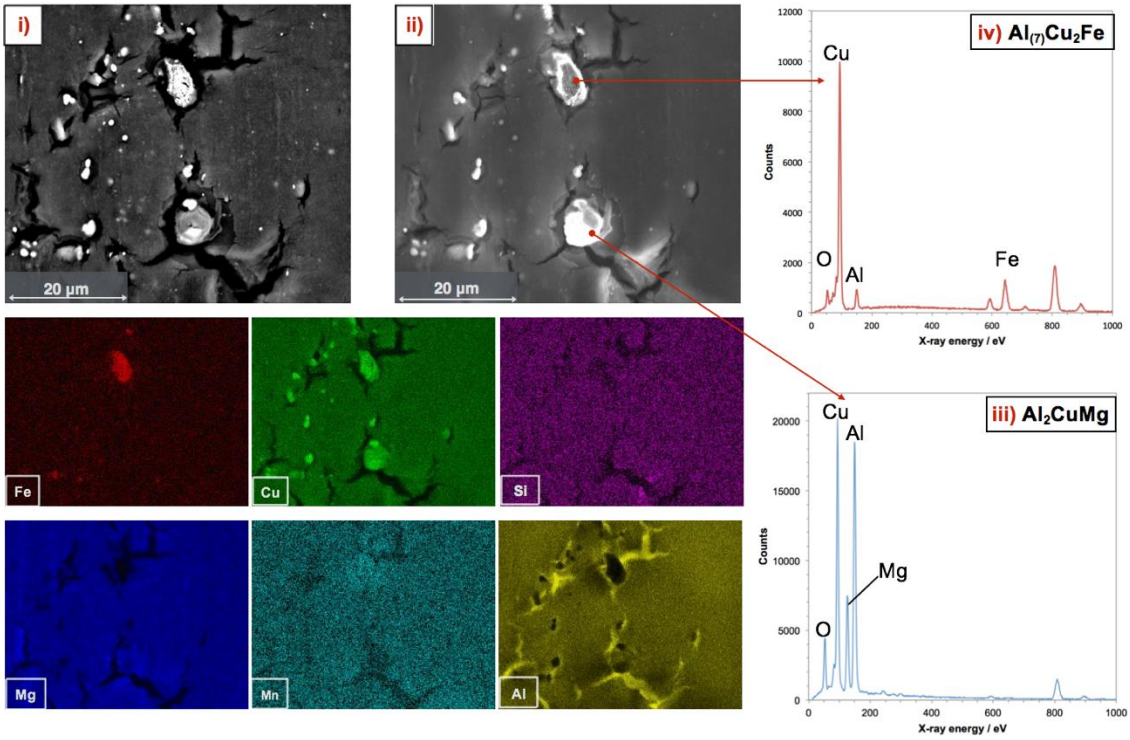

Figure 30 : SEM micrographs of AA2024-T3 in (i) image in backscattered electron mode and (ii) secondary electron mode. The corresponding X-ray mapping and EDS spectra corresponding to the two particles which are labelled as iii) and iv) are shown, revealing Al_2CuMg and Al_7Cu_2Fe after 1.25 M NaOH at 60 °C respectively.

Some particles were completely removed from the surface during the NaOH treatment, departing the surface principally by undermining (from dissolution of the surrounding matrix). This particle detachment process has also been evidenced by ICP analysis, and was accompanied by the presence of a heavy residual layer composed most likely of hydrated aluminum oxy-hydroxides.

An equivalent SEM analysis after HNO_3 exposure (**Fig. 31**) reveals the presence of cavities on the surface, suggesting particle release during the pretreatment (top left). On the other hand, the top right image in Fig. 6 shows a remnant particle, which did not seem affected by the pretreatment. These particles were of the Fe-Mn-Cu rich type, and persisting upon the AA2024-T3 surface. The average size of these particles (~5 µm) corresponds to what are constituent

particles [46]. These results are in good agreement with the wider literature and confirms that HNO_3 is not completely efficient in removing all surface intermetallics [86]. Moreover, the surface composition after pretreatment was also estimated by EDX analysis and reveals an increase of the Cu content of approximately 1.7 wt % (4.2 before pretreatment to 5.9 % after pretreatment).

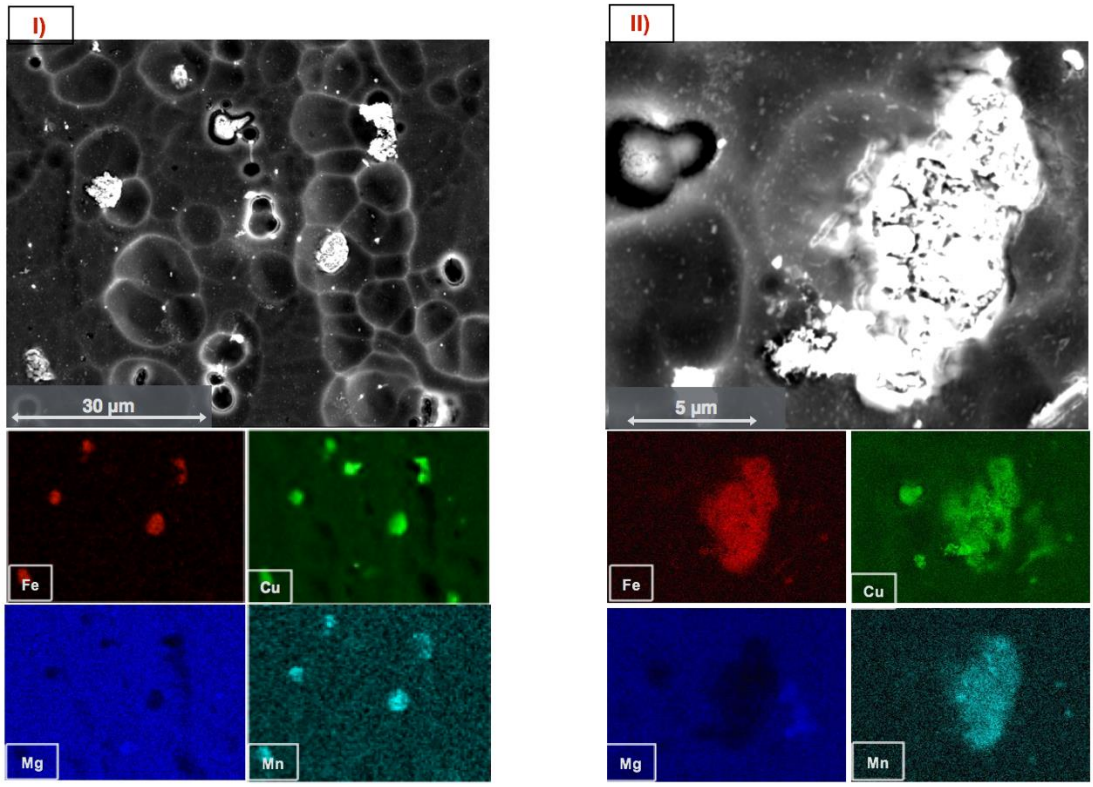

Figure 31 : EDS maps performed on two locations after the exposure of AA2024-T3 to 1.25 M NaOH at 60 °C for 5 minutes, followed by 2.8 M HNO_3 for 15 minutes. I) represents the general surface showing the protruding particles and II) is a map on a remaining particle.

Cross sections of the oxidized surface at three different times during the NaOH exposure (**Fig. 32**) reveals that the residual film grows systematically with time**.** From these images – taken in backscattered electron mode - it is possible to see some particles (likely Cu containing particles) disassociating themselves from the matrix and remaining within the Al hydroxide / oxide film. The micrograph at 3 minutes shows what appears to be a uniform Cu film at the extreme surface probably due to residual Cu remaining after selective dissolution of Al from the bulk matrix. This structure is no longer visible after 5 minutes as the oxide film becomes more complicated. This dark grey structure could be a combination of intermetallic particles surrounded by an Al/Mg hydroxide thick film. However, it was not possible to determine the composition of the layer from this micrograph. A number of different particles are observed with very different compositions; **Table 10** provides an overview of the EDS analysis observed for 3 different intermetallic particles and two surfaces, one after NaOH treatment and the other after HNO_3 treatment corresponding to Figure 5 and 6.

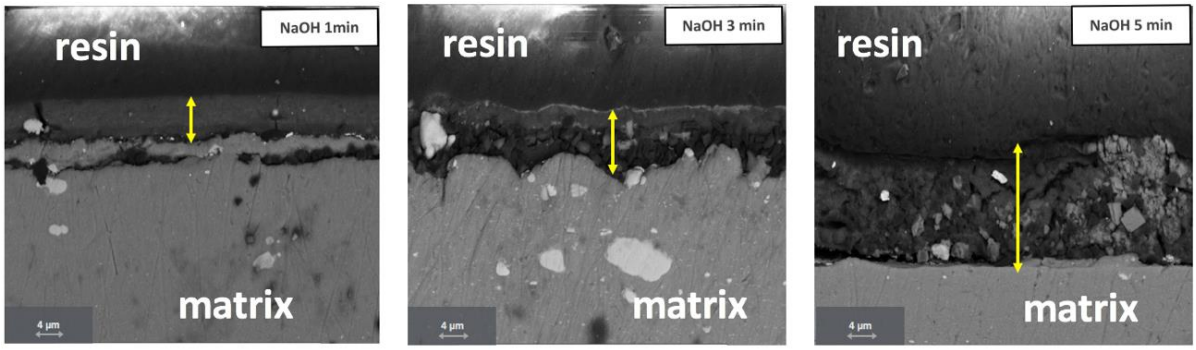

Figure 32 : SEM micrographs in cross section of the oxidized surface after 1, 3 and 5 minutes of exposure to 1.2 M NaOH at 60°C. (Backscattered electron images) - LEO series 1500

Table 10 : Elemental composition of alloying elements and surface composition after NaOH and HNO_3 exposures determined from EDS spectras and mapping (in wt% and at%).

		Al	*Cu*	*Mg*	*Mn*	*Fe*	*Si*	*O*	*Total%*
i) Al_2CuMg	wt%	36.82	40.91	14.39	-	-	-	7.88	100
	At %	44.13	20.82	19.13	-	-	-	15.92	100
ii) $Al_{(7)}Cu_2Fe$	wt%	4.19	68.58	-	-	23.89	-	3.36	100
	At %	8.29	57.64	-	-	22.85	-	11.22	100
iii) & iv) Surface after NaOH	wt %	36.82	40.91	14.39	6.86	-	-	-	100
	At %	44.13	20.82	19.13	4.49	-	-	-	100
I) Surface after $NaOH + HNO_3$	wt %	88.59	5.88	1.88	0.55	0.12	0.05	2.93	100
	At %	89.95	2.54	2.11	0.28	0.06	0.05	5.01	100
II) Al-Fe-Cu-Mn	wt %	49.25	29.12	-	6.86	10.89	2.43	1.45	100
	At %	65.64	16.48	-	4.49	7.02	3.11	3.26	100

3.3. Kinetics of Cu rich Particle Release in NaOH

As previously described, the dissolution rate of Cu is comparatively low during the NaOH treatment, and the alloy potential remains well below the reversible potential for Cu oxidation in this electrolyte; thus we may affirm that Cu released in NaOH is due to non-faradaic processes. Indeed, sharp spikes are revealed, representing the release of Cu rich particles that are transported to the plasma [117,145]. In previous work, we have demonstrated that solid particles entering the plasma will give rise to a peak of < 10 ms in duration.

Therefore, to confirm the attribution of these peaks to Cu rich particle release, the experiment in **Fig. 27** was repeated at a data collection rate of 10 points per second (100 ms duration) instead of the release of a single particle should give rise to a single data point peak. The results over a 15 s period are shown in **Fig. 33**.

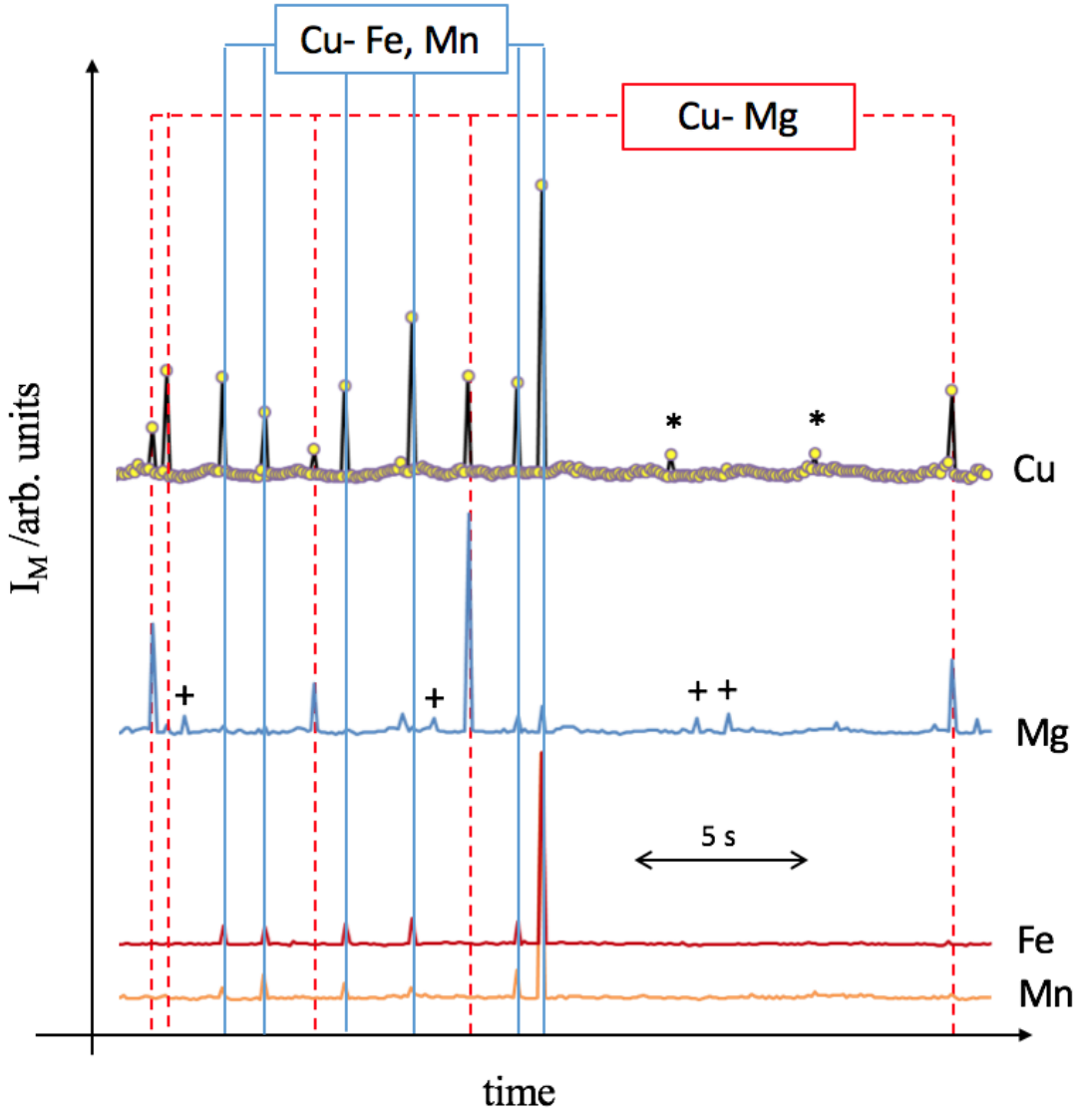

Figure 33 : Transient data for Cu, Mg, Fe, and Mn during the reaction of AA2024- T3 with 1.25 M NaOH at 60°C obtained at 10 points per second. The sharp peaks (single points) correspond to particle release. Different types of particles are detected including those that

contain Cu and Mg (solid lines) and Cu Fe and Mn (dashed lines). Particles containing only Cu are indicated with a "*" and only Mg by a "+".

The upper curve (corresponding to Cu) in **Fig. 33** reveals a series of peaks corresponding to a single point of 100 ms, corroborating with the notion that Cu rich particles are burst released, likely through a non-faradaic process. Interestingly the Cu peaks appear to correlate with either a similar transient in either the Mg signal or with the Fe signal. By contrast, Mg and Fe peaks are rarely seen together, suggesting a stoichiometry of Al_2CuMg or Al_7Cu_2Fe consistent with the particles observed in **Fig. 30**.

The measured Fe transients also correlate with Mn transients, somewhat complicating prescription to specific particles, however these signals may be attributed to the Al-Cu-Mn-Fe phase, which is noted as representing ~40 % of the constituent particle population for AA2024-T3[46]. For some of the smaller transients observed in **Fig. 33**, only a single element peak was detected. Pure Cu peaks are indicated with a "*" and pure Mg peaks are indicated with a "+". These results demonstrate that particle release may be observed in real time, however the quantification is difficult because only a fraction of the particles will be transported to the plasma. It is probable that the fraction of particles transmitted to the plasma will vary with the particle size [117].

3.4. Dissolution and passivation in HNO_3

The dissolution profile obtained when the water rinse is exchanged for HNO_3 is given in **Fig. 34**. Shown as a function of time are the potential (**Fig. 34a**); the Al, Cu and the theoretical residence time distribution (**Fig. 34b**); and the Mn, Mg, Fe and Ti (**Fig. 34c**) dissolution rates. The HNO_3 first enters the cell at the point indicated by the dashed line where the potential begins to increase. The dissolution of the Mg and Al begins approximately 20 s later, corresponding to about a 60 % changeover according to **the electrolyte exchange study (appendix)**. Also shown in **Fig. 34b** is a theoretical residence time distribution curve, h(t), calculated for the conditions of this experiment [126].

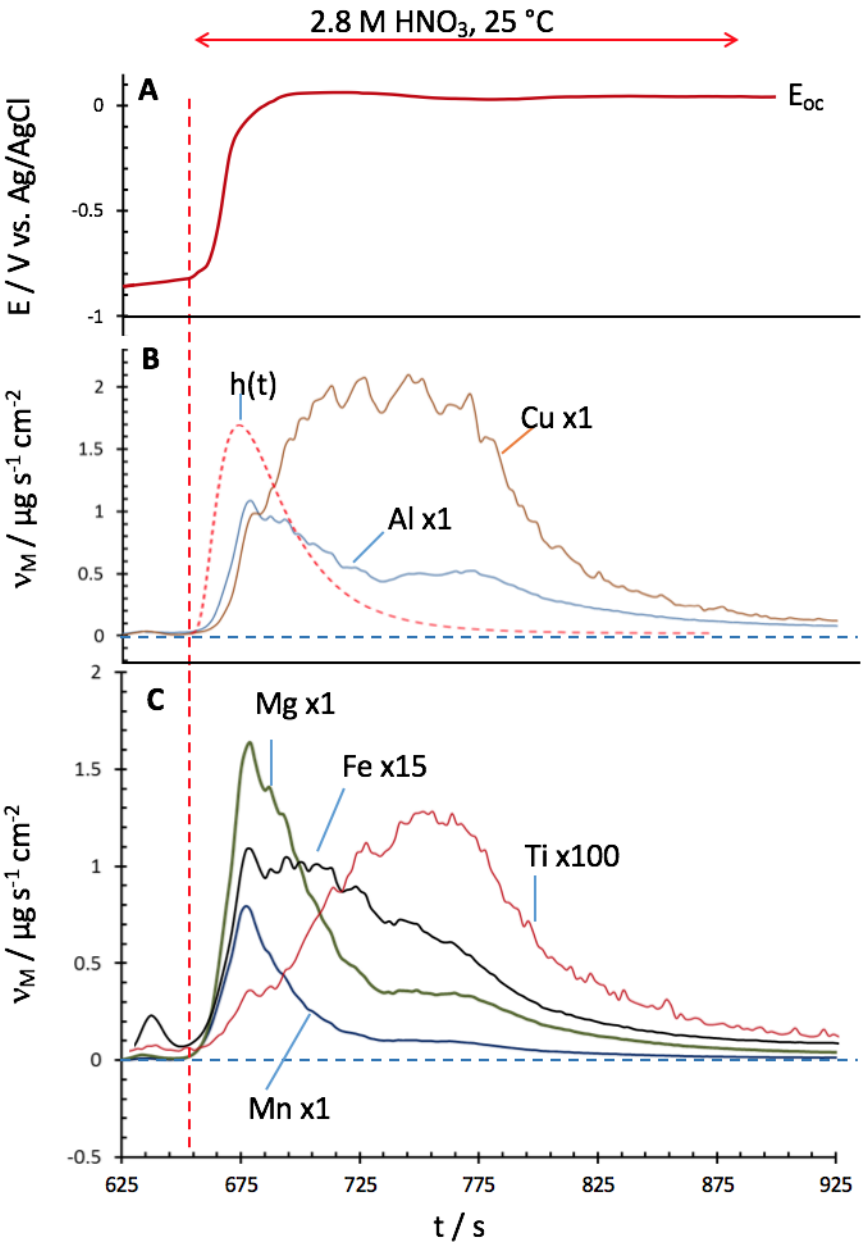

Figure 34 : Dissolution profile for AA2024-T3 in 2.8 M HNO_3, 23°C, following 1.25 M NaOH exposure at 60 °C, showing (A) the potential, (B) Al, Cu, the residence time distribution h(t) and (C), Mg, Mn, Fe (x15) and Ti (x100) as a function of time.

Initially, there is a sharp peak of Al, Mg, Fe and Mn. These peaks are consistent with the residence time distribution of the cell and therefore corresponds to an instantaneous dissolution on the time scale of this experiment. On the other hand, Cu rises with the Al signal and reaches a steady state value of 2 µg s^{-1} cm^{-2} for ~ 50 s. Meanwhile, Ti dissolution rate rises much more slowly, over a 50 s time period, and reaches a maximum extending for about 50 s. Such slow kinetics demonstrate that the dissolution rates of these elements are limited by the reaction with HNO_3. The simple interpretation of this behavior is that the film consists of Al, Mg and Mn hydroxides that are immediately dissolved on contact with HNO_3; and Cu, Fe and Ti containing intermetallics dissolve more slowly. An important point revealed by **Fig. 34** is that the

dissolution reactions are essentially complete within 200 s from the initial contact with HNO_3 and the potential is relatively constant at ~0.05 V vs. Ag/AgCl. This demonstrates how fast HNO_3 dissolves the residual oxide films and intermetallic particles from the surface while passivating the underlying substrate. Assuming that only the elements in the residual film contribute to the dissolution in 2.8 M HNO_3, the quantities of Al, Cu, Mg, Fe, Mn and Ti in the residual film were calculated from the integral of the data in **Fig. 34**. The results are given in **Table 11** and compared with EDS measurements in **Table 10** for the surface after NaOH exposure, revealing a similar trend. Indeed, the quantities of Cu, Mg and Mn have similar values, however, the Al value is notably higher from the EDS analysis, more than likely accounted for by Al contained in the matrix as a result of the large x-ray interaction volume in EDS that extends beyond the size scale of surface film or particle size. Moreover, the low sensitivity of EDS analysis does not reveal any Fe or Ti in the residual film.

Table 11 : Elemental composition and absolute quantity of the residual film (calculated from integral of fig 34.) and from the mass balance

Element	*Al*	*Mg*	*Cu*	*Mn*	*Fe*	*Ti*
Concentration $\mu g\ cm^{-2}$ (dissolved in HNO_3)	84.4 (26.8 %)	57.4 (18.2%)	147.8 (46.9%)	20.7 (6.6%)	4.6 (1.5%)	0.6 (0.2%)
Concentration after HNO_3 exposure	-	14.9	70.0	3.2	1.8	0.2

It was of interest to verify the assumption that only the residual film contributes to the dissolution profile of **Fig. 34**. Consequently, an AA2024-T3 sample was exposed to 2.8 M HNO_3 for 15 min, without any prior exposure to NaOH. **Fig 35** illustrates the dissolution rates of Al, Mg and Cu as a function of time.

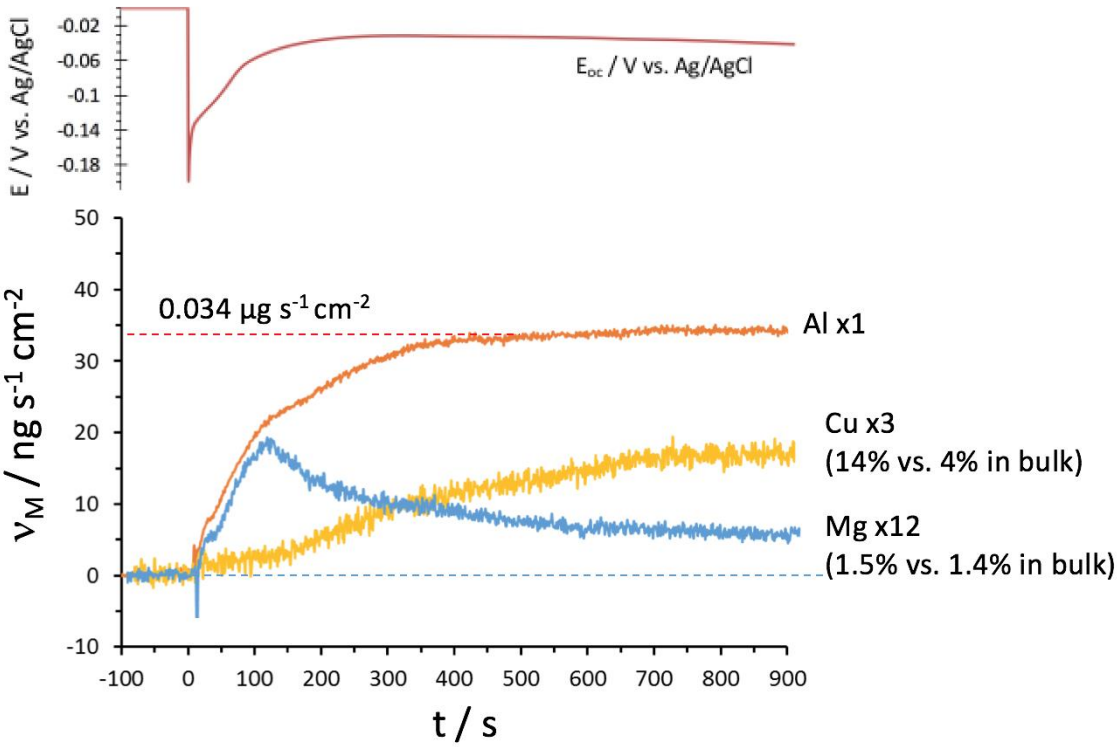

Figure 35 : Dissolution profile for AA2024 – T3 in 2.8 M HNO_3, 23°C, without pretreatment showing Al, Cu, and Mg dissolution as a function of time (Mn, Fe and Ti were not detected).

The electrolyte makes contact with the sample at t = 0, where the Al dissolution rate starts to rise continuously for approximately 300 s and reaches a steady state value of ν_{Al} = 34 ng s^{-1} cm^{-2}. However, the alloying elements (with the exception of Mn, Fe and Ti which were not detected) exhibit different kinetics of dissolution in this experiment. The Cu signal begins to increase ~150 s later than the Al signal. Nevertheless, the shape of the curve is similar to the Al curve as the signal stabilizes at ν_{Cu}= 5 ng s^{-1} cm^{-2} until the conclusion of the experiment. The Mg signal was more difficult to detect, as the signal was very close to the background level. However, the Mg signal reaches a maximum of ν_{Mg} = 1.5 ng s^{-1} cm^{-2} at 100 s and slowly goes to a steady state value of 0.5 ng s^{-1} cm^{-2}. These values also highlight the selective dissolution of Cu during this experiment. Indeed, ν_{Cu} / ν_{Al} = ~14 % which is higher than the 4.2 % in bulk AA2024-T3 if we assume congruent dissolution. However, Mg exhibits a different behavior as the steady state Mg/Al ratio (1.5%) has the same value as the bulk composition demonstrating the simultaneous dissolution of the two elements.

This experiment suggests that, selective dissolution of Al and Mg occur under HNO_3 exposure with preferential dissolution of Mg at the early stage of the experiment (Mg/Al = 7 at 100 s). This phenomenon is most likely occurring at intermetallic particles. As Mg and Al are dissolving, the open circuit potential steadily increases (the potential value starting at ~-0.2 V vs. Ag/AgCl and reaching ~ -0.03 V vs. Ag/AgCl after 200 s); this could be rationalized by nobler elements remaining on the surface, such as Cu. When the majority of Al and Mg are

dissolved at the intermetallic particles (which can even be considered preferred local anodes for supporting the net anode load) [46,48], Cu starts to dissolve. This also correlates with the evolution of open circuit potential, whereby as the Cu is dissolved during the experiment, the open circuit potential decreases.

From the results herein, Q_{Cu}= 3.45 ± 0.03 μg cm^{-2} in the absence of NaOH pretreatment, as compared with Q_{Cu}= 150 μg cm^{-2} following NaOH pretreatment. Therefore, only 2.3 % of this amount corresponds to Q_{Cu} coming from the underlying metal. Thus, we can assume that the Cu dissolved during the HNO_3 step in the complete pretreatment, is essentially coming from the residual film formed during the NaOH etching.

Further *ex-situ* characterization was performed on the sample, using FIB-SEM (**Fig 36).** The top view image indicates localized attack surrounding the intermetallic particles, especially at the particle / matrix interface. The particle has a dealloyed, sponge like shape suggesting selective dissolution of certain components during the HNO_3 exposure leaving these small particles at the surface. The cross section images were performed on two dealloyed intermetallic particles. From the images it is possible to see the presence of trenches, characteristic of the selective dissolution phenomenon around the intermetallic particles due to a microgalvanic coupling between the Al matrix and the intermetallic particle [38,46]. On the other hand, the matrix seems to not be significantly attacked by HNO_3. Such observations correlate with the assertions from ICP results, which also reveal selective dissolution of Al and Mg.

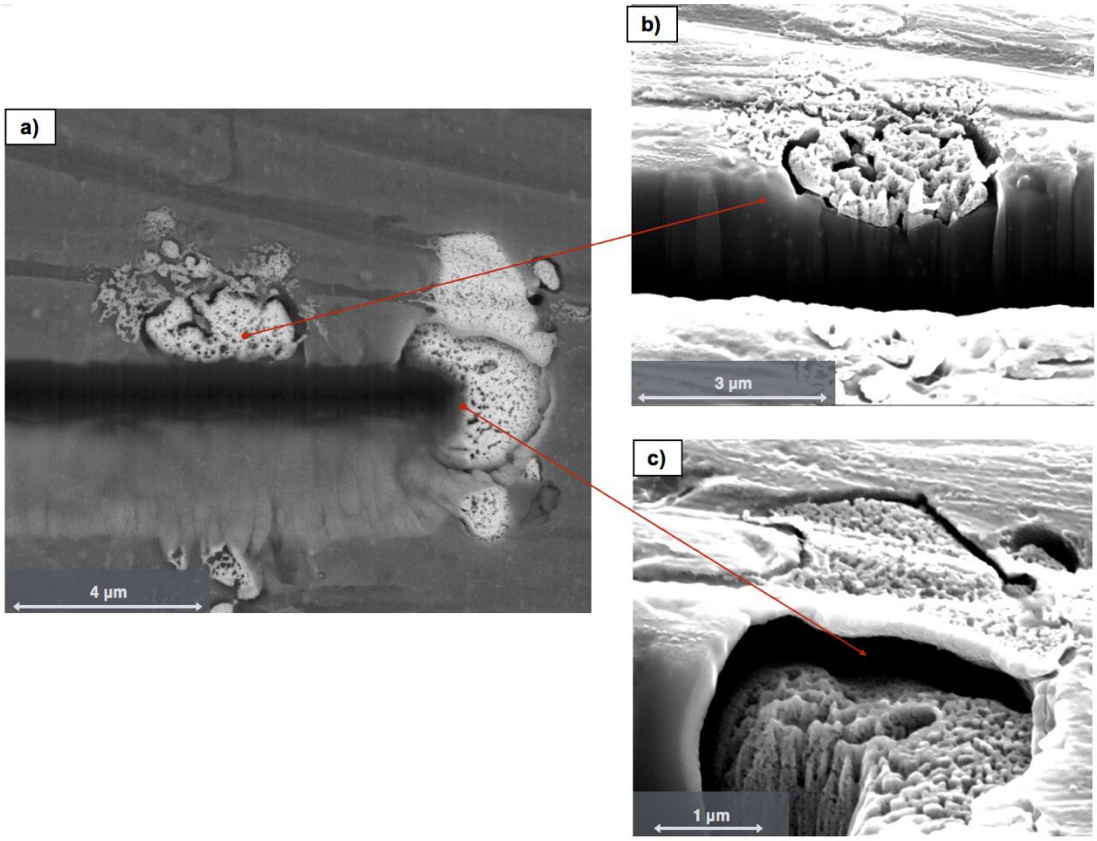

Figure 36 : FIB and SEM micrograph of AA2024-T3 intermetallic particles after 15 min exposure in 2.8 M HNO3 revealing dealloying at the Al/intermetallic particle interface and in the particle.

3.5. Polarization Behavior prior to, and following, pretreatment

To better characterize the effects of the surface treatment, simultaneous AESEC information with polarization curves of the treated and untreated AA2024-T3 were performed in 0.5 M NaCl at pH = 6.7, and at room temperature (**Fig. 37**). The conventional polarization curves are shown in Fig. Figure **37A**, showing electrochemical current, j_e,as a function of potential on a log $|j_e|$ vs. E scale. **Fig. 37B** compares j_e and j_{Al} showing a comparative Faradaic yield throughout, although there is a slight offset between j_e and j_{Al} which is likely due to surface film / oxide formation. Comparing the treated and untreated surface in **Fig. 37A**, a marked effect of pretreatment is apparent; with the cathodic current above -0.8 V vs. Ag/AgCl reduced by more than an order of magnitude and the onset of the enhanced dissolution domain is shifted by ~ 40 mV. The potential where $j_e = 0$ (i.e. the corrosion potential) coincides with the pitting potential for both surfaces. These results would normally suggest a decrease in the quantity of Cu at the surface as Cu accelerates the cathodic reaction and destabilizes the passive film. However, the results of Fig. 3 indicated an excess of Cu at the surface following the pretreatment sequence. It is likely that the remaining Cu is either passivated by the nitric acid treatment or is somehow detached from the surface such that there is no electrical contact between the Cu and the Al.

Excess Cu is clearly evidenced in **Fig. 37C**, which reveals the partial Cu dissolution rate (expressed as an equivalent current by Eq. 2) measured at the same time as the polarization curves of **Fig. 37A**. The result shows that Cu dissolution is remarkably enhanced by the surface pretreatment sequence. For the untreated surface, Cu dissolution is almost exclusively in the form of particles with very little background Cu dissolution suggesting a non-faradaic Cu release[14,45], where Cu nanoparticulates physically detach from the surface during the dissolution of Al and Mg. For the treated surface however, a steady signal of Cu dissolution increases along with j_e and j_{Al}. Nevertheless, Cu dissolution is well below that expected for a stoichiometric dissolution.

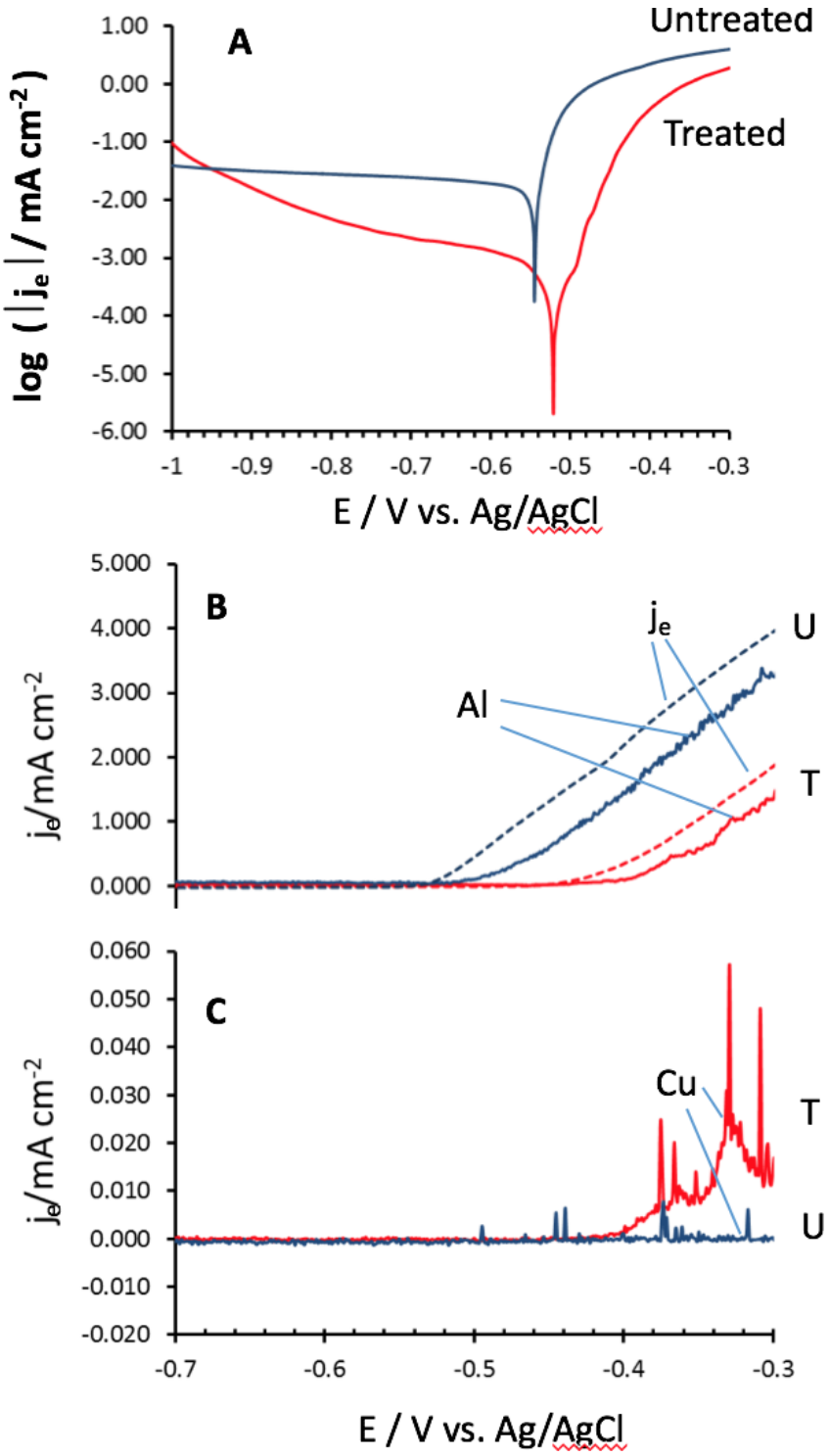

Figure 37 : AESEC – polarization curves of treated and untreated AA2024-T3 in 0.5 M NaCl, at pH = 6.7, and at room temperature, before and after pretreatment, measured at 1 mV s^{-1}. (A) Conventional polarization curves, (B) j_e (dashed) and j_{Al} (solid) showing the Faradaic yield for Al dissolution in the transpassive domain; (C) j_{Cu} showing enhanced Cu dissolution for the pretreated material. The peaks in Cu dissolution indicate particle release.

A similar analysis was performed for Mg and Mn (not shown) and their respective signals increased proportionally to the Al signal in agreement with a congruent dissolution. The Mg/ Al ratio was 1.4 % vs. 1.6% bulk while Mn/Al was 0.25% vs. 0.39% bulk. Fe and Ti dissolution

was not detectable in these experiments probably due to their insolubility in neutral pH electrolytes.

Coupling of AESEC with open circuit pretreatment exposures, and polarization testing as described herein, provides a significantly novel, and new, insight into Al-alloy pretreatment. This approach across Al-alloy systems, and specific pretreatments can be used to both understand surface evolution, and also as a means of optimizing pretreatment.

4. CONCLUSIONS

In this study, the AESEC technique was used for the first time to measure the dissolution kinetics of Al-alloy AA2024-T3 during a pretreatment sequence. The results highlighted the prevalence of incongruent dissolution, along with the formation of films containing residual alloying elements during the pretreatment sequence. From the experimental data herein, several conclusions can be made:

1) In 1.25 M NaOH at 60 °C, selective dissolution of Al was measured. The Al dissolution rate rapidly reached a steady state value, and this value appeared to be reproducible. The depth of attack measured by profilometry was in agreement with dissolution rate obtained by ICP-AES.
2) Signals of Cu, Mg and Fe were detected in ICP-AES primarily as sharp peaks in 1.25 M NaOH, indicating a burst-like particle release during the alkaline treatment step. Coincident Mg and Cu spikes were detected. The Fe signal was less frequent and only correlated with the Cu signal. These results were interpreted in terms of the release of specific particles, namely Al_2CuMg and Al_7CuFe
3) During HNO_3 exposure, two times periods of dissolution were distinguished: The early Al, Cu and Mn peaks correspond to the instantaneous dissolution of the hydroxide layer formed during NaOH etching. These elements are completely soluble in HNO_3. On the other hand, Cu, Ti and Fe exhibit slower dissolution kinetics, indicating that their reaction is not instantaneous and that the reactivity to HNO_3 of these elements is different.
4) From a mass balance analysis (considering the elemental composition of AA2024-T3, and the dissolution rates obtained by the AESEC), it was revealed that some residual particles (most probably Cu containing species) remained at the surface following the entire pretreatment process.
5) The SEM analysis evidenced significant alterations on the surface after NaOH exposure. The EDS spectra and mapping were carried out on particles protruding from the surface illustrating the presence of alloying elements in the enriched layer. These results are consequently in good agreement with the ICP results. Cross-sections of the surface at three different times during NaOH exposure highlight the formation of an Al hydroxide/oxide film where some intermetallic particles are incorporated. It was possible to distinguish a thin Cu film at the extreme surface caused by the selective dissolution of Al.
6) On the other hand, according to the SEM micrographs, HNO_3 seems to dissolve the particles, leaving cavities on the surface. However, EDS mapping indicated Fe-Mn-Cu

rich particles subsisting on the surface. The EDS analysis of the surface also suggests a notable increase of Cu content, consistent with reported literature.

7) By integrating the dissolution profiles of AA2024-T3 under HNO_3 exposure, it was possible to determine the quantities of Al, Cu, Fe, Mn and Ti present in the residual film. The results were compared to EDS analysis and revealed a similar trend. Nevertheless, the AESEC data seemed to be more sensitive as compared to EDS measurements.
8) AESEC polarization curves before and after pretreatment revealed a significant decrease of the cathodic current and an anodic shift of the transpassive domain following pretreatment. This was explained by the removal of Cu containing particles during the pretreatment. However, surprisingly, the analysis shows the presence of an excess residual Cu dissolving from the surface. This result could be interpreted by the passivation of the remaining Cu during HNO_3 treatment or by a physical detachment of the particles from surface such as no electrical contact was possible between Al and Cu.

5. APPENDIX

5.1. Hydrodynamics

The concept of this work was to simulate the entire surface pretreatment process, which involves multiple steps. Therefore, unlike most previous AESEC investigations, it was necessary to change the electrolyte during the course of the experiment. The aim of this section is to report the rate of electrolyte change in the cell, when one electrolyte is substituted for another at the reservoir.

The measurement was performed by filling the cell with a 1.25 M NaOH electrolyte containing 10 ppm Al, then switching the flow over to the bypass and rinsing the capillaries with water until the Al signal had decreased down to the background level. Then the electrolyte flow was switched back to the electrochemical flow cell and the Al concentration transient was monitored as a single volume of the cell as washed downstream by water. An overlay of two concentration transients thus obtained is given in **Fig. A1** as well as the integral of the concentration transient, all shown as a function of log(t).

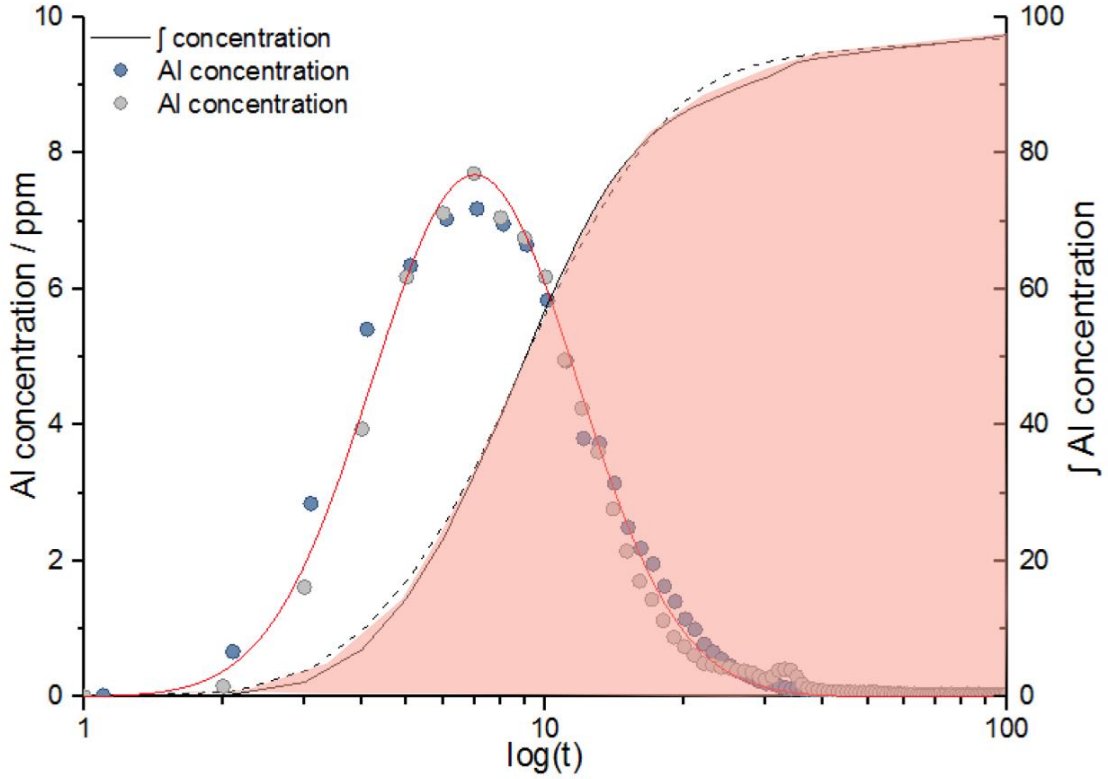

Figure A1: Experimental data and the curve fit used to determine the residence time distribution of an electrolyte between two pretreatment steps. The curve fit is presented as a log-normal distribution with these parameters: β = 1.9 ± 0.03 and τ =7.02 ± 0.04

The result reveals that the Al is rapidly removed from the cell, as 90 % of the Al is evacuated from the cell in approximately 25 ± 2 s. From the integration of the concentration peak, it was possible to calculate the volume of electrolyte measured in this experiment as follows:

$$Q_{Al} = f \int_{t0}^{t} C_{Al}(t)\, dt = (V_{cell} + V_{tube})\, C_{standard} \quad 1)$$

where $C_{standard}$ is the standard concentration used for the experiment in ppm (10 ppm of Al) and V_{tube} the volume of the two capillaries connecting the flow cell to the FIA valve. $V_{cell} + V_{tube}$ was found to be $V_{cell} + V_{tube} = 0.26 \pm 0.02$ cm^3 with $V_{tube} = 0.07$ cm^3, so $V_{cell} = 0.19 \pm 0.02$ cm^3. The experimental data are represented by points in **Fig A1.** The fit curve is a log normal distribution fit to the experimental data:

$$h(t) = \begin{cases} \sqrt{\frac{\beta}{\pi\tau^2}}\, e^{-\frac{1}{4\beta}}\, e^{-\beta ln^2 \frac{t}{\tau}} & if\ t > 0 \\ 0 & if\ t = 0 \end{cases} \quad 2)$$

β and τ are empirical parameters. For this work, those parameters were found to be β = 1.9 ± 0.03 and τ =7.02 ± 0.04 yielding an increased time resolution as compared to the galvanostatic pulse measurements reported previously [116].

5.2. Surface topography and etching rate

Fig. A2 shows an optical micrograph of the surface after treatment with NaOH. The surface is clearly darkened due to the formation of oxides and other residual films during this treatment making it easy to visually identify the attacked surface. The edge of the attacked zone shows some non-uniformity no doubt due to an attack under the area delimited by the o-ring. Image analysis of the attacked zone yielded a surface area of 0.87 ± 0.07 cm^2. **Fig. A2a** shows a line scan measured with an optical profilometer along the edge of the attacked zone after removal of the black residual film by treatment with HNO_3. It is clear that the edge is fairly well defined, dropping 19 μm in approximately 500 μm. **Fig. A2b** also highlights the change in surface roughness due to the surface pretreatment. The roughnesses measured before and after pretreatment are respectively 0.162 μm and 0.409 μm. Coating adhesion, in surface treatment industry, is regularly checked to assess the quality of the surface preparation. Different studies have been carried out to understand the effect of roughness on the adhesion [129,146]. It has been shown that when the roughness increases, new bonding sites are created for the coating and the adhesion strength is enhanced [129,146]. Thus, the deposition rate and adhesion properties of the subsequent coating rely on this parameter **Fig A2b**. also shows a three-dimensional analysis of the edge in the upper left hand corner obtained using a stylus profilometer. This analysis also shows a number of protusions within the attacked zone.

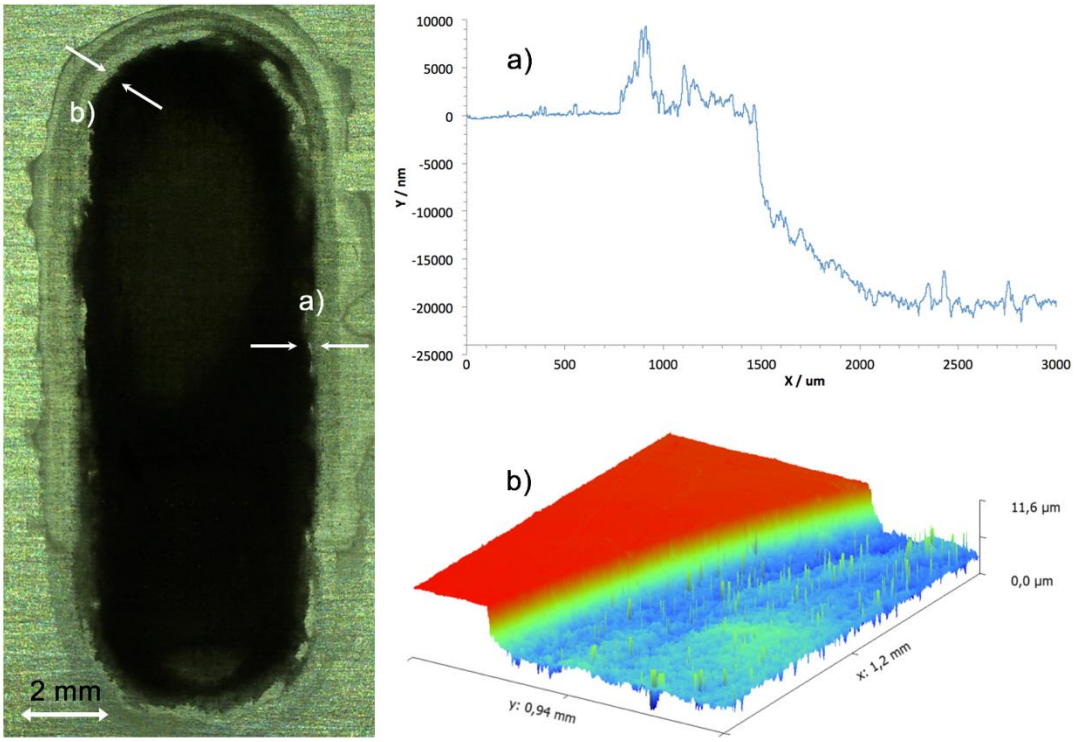

Figure A2 : Optical photograph of the surface after NaOH exposure and the profilometry data measured at different spots on the surface. The 3D image b) and the 2D profile a) show the absence of edge effect and that the surface is relatively well defined.

ACKNOWLEDGMENTS: WE WOULD LIKE TO THANK LIONEL PEGUET FROM CONSTELLIUM FOR SUPPLYING THE AA2024-T3 AND THE USEFULL DISCUSSIONS.

CHAPTER IV: ON-LINE REACTIVITY MEASUREMENT OF AL-LI ALLOY AA2050-T3 DURING A SURFACE PRETREATMENT SEQUENCE USING AESEC

" لا تثق فى البدايات، فاصدق الكلام يقال فى اللحظة الاخيرة . "

جبران خليل جبران .

"Don't trust the beginnings, truth is told in the last moments."

Gibran Khalil Gibran.

On-line reactivity measurement of Al-Li alloy AA2050-T3 during a surface pretreatment sequence using atomic emission spectroelectrochemistry.

O. Gharbi[1], N. Birbilis[2], K. Ogle[1], *

[1] Chimie-ParisTech, PSL Research University, CNRS - Institut de Recherche Chimie Paris Paris 75005, France

[2] Department of Materials Science and Engineering, Monash University, VIC 3800, Australia

The dissolution of aluminum alloy AA2050-T3 (which contains 0.77 wt.% Li) during a chemical pretreatment sequence was investigated. Atomic emission spectroelectrochemistry (AESEC) was used to quantitatively measure the dissolution rates of individual alloying elements during a complete pretreatment sequence. The results reveal significant Li and Al dissolution, and Cu enrichment during NaOH exposure. When the alloy was exposed to HNO_3, excess Cu was preferentially dissolved in addition to the dissolution of Fe, Mn and Mg. Polarization testing in conjunction with on-line AESEC reveal a decrease in both anodic and cathodic currents, along with an increase in the alloy pitting potential, following pretreatment. In addition, what appears to be a protective Li/Al surface film was also determined to exist with GDOES surface profiles following polarization as indicated by an increase in the surface Li/Al ratio. Beyond the context of surface pretreatment, which is necessary precursor to conversion coating, the study herein also provides significant insights into the corrosion of AA2050-T3 - including selective dissolution and its attendant rate - which are previously unreported.

Keywords: Al-alloy, pretreatment, spectroelectrochemistry, Al-Li

This article was submitted to Electrochimica Acta

1. INTRODUCTION

High strength aluminum (Al) alloys continue to be developed in pursuit of property combinations that include high strength, low density and corrosion resistance [147]. The 2xxx series Al-alloys, namely the legacy alloy AA2024-T3, have a long history of use in aerospace applications owing to their mechanical properties [5,6]. However, it is also well recognized that owing to the main alloying element required for increased mechanical properties (copper, Cu), a reduction in corrosion resistance occurs [11,46,131]. More recently, lithium (Li) -containing Al-alloys have been developed with a balance of properties that exceed AA2024, and also exceed the properties of many 7xxx series Al-alloys (based on the Al-Zn-Mg systems) such as plate alloys AA7075 or AA7050 [59,148–150]. Whilst Al-Li alloys have been under development for many decades, the modern generation of Li-containing Al-alloys (which are strictly Al-Cu-Li alloys) have demonstrated both a high strength in conjunction to very high corrosion resistance in the peak aged condition [59]. Such alloys include AA2050 and AA2060. Moreover, numerous studies have showed that each 1 % of Li added decreases the alloy density by 3 % [3,58].

In spite of improved corrosion resistance relative to other high strength Al-alloys, Al-Cu-Li alloys are also nominally surface treated and coated prior to use in service, typical of all Al-alloys [81]. Furthermore, the structural heterogeneity of Al-Cu-Li alloys does lead to a surface electrochemical heterogeneity that can contribute to localized corrosion [60,72,151] and microgalvanic coupling between the alloy matrix and intermetallic particles [64]. In regards to corrosion propagation of Al-Cu-Li alloys, numerous reports have attributed intergranular corrosion and stress corrosion cracking to the effect of precipitated T_1 phase (Al_2CuLi) located along sub-grain boundaries [72,152], however the prevalence of such modes of corrosion propagation are temper dependent [78–80].

Numerous surface treatments and subsequent coatings formulation have been designed in order to eradicate or at least decrease the corrosion susceptibility of Al-alloys. In general, Al-alloys are conversion coated for corrosion protection, however prior to conversion coating, there are important chemical ‘pretreatment’ steps that occur. In fact, it has been reported that pretreatment is a critical step in the corrosion protection system, as it contributes towards the quality of any subsequent coating [138,153]. A typical pretreatment sequence for high strength Al-alloys consists of an alkaline treatment, to remove organic surface residue and to dissolve the natural oxide layer; followed by an acid treatment (often also called deoxidizing or pickling). The combination of pretreatment steps is used to homogenize the alloy surface, by removing surface intermetallic particles and creating a more uniform surface chemistry prior to subsequent coating. The relevance of pretreatments to AA2024-T3 have been well documented previously [84,99], whilst also indicating that depending on the process conditions,

selective dissolution may occur and this may also lead to Cu enrichment [16,97,103]. Whilst there are some decades of experience in the pretreatment of AA2024-T3, there exist less reports of the efficacy and mechanistic aspects related to the pretreatment of Al-Cu-Li alloys, such as AA2050-T3.

The composition of AA2050 differs from that of AA2024-T3 via the addition of Li, in addition to a decrease in the Mg content. This results in the formation of different phases within the alloy, namely with Al_2CuLi (T phase) being the principal precipitate in AA2050, where Al_2CuMg (S phase) is the principal precipitate in AA2024 [70]. Furthermore, the size range and aspect ratio of T phase is considerably different to that of S phase (T phase being significantly thinner and with a higher aspect ratio); whilst the constituent particle population in AA2050 includes less coarse constituent particles, and some Ag-containing particles. All such difference may affect the pretreatment process and its efficiency, and should be considered.

Herein, the atomic emission spectroelectrochemistry (AESEC) technique was used for on-line measurement of the dissolution of AA2050-T3 during a pretreatment sequence. The aim of this study was to understand the effect of a well-known pretreatment sequence for Al-alloys upon AA2050-T3 with regards to alloying element dissolution, surface enrichment and in particular the fate of Li which is usually not readily possible to measure with other techniques. Furthermore, as previously demonstrated, AESEC technique allows a direct quantitative measurement of elemental dissolution and particle detachment, in real time, under simulated industrial conditions [128].

2. EXPERIMENTAL

Materials Commercial AA2050-T3 aluminum alloy plate (10 mm thick) was used in this study. The composition of the alloy studied was independently determined (Spectrometer Services, Victoria, Australia) and is given in **Table 12**. Test samples were mechanically ground with silicon-carbide (SiC) paper to a final finish of 4000 grit under ethanol, and dried using nitrogen. Grinding was carried out in order to provide a consistent initial surface, which was deemed necessary [128] on the basis that as-received material may contain a grain refined surface layer (GRSL) from manufacturing. In cases when more detailed surface analysis was required, samples were polished to a 0.25 µm diamond paste finish. All chemicals used during the experiments were prepared with purified water (18.2 MΩ.cm, Millipore™).

Table 12 : Chemical composition of AA2050-T3 (wt%).

Al	*Cu*	*Mg*	*Zn*	*Fe*	*Li*	*Mn*	*Ni*	*Sr*	*Zr*	*Ag*	*Cr*	*Ti*	*Si*
Bal	3.30	0.32	0.02	0.06	0.77	0.39	<0.01	<0.001	0.08	0.17	<0.01	0.03	0.10

Atomic emission spectroelectrochemistry (AESEC) The AESEC method has been previously described in detail[111]. The AESEC method uses a three electrode electrochemical flow cell coupled to an ICP-AES (inductively coupled plasma atomic emission spectrometer) which quantifies the elements released from the sample working electrode in the flow cell. A potentiostat is used to control and/or measure the electrochemical current and potential in the flow cell. The electrolyte enters contact with a sample (the working electrode) at a constant flow rate and is subsequently collected by ICP-AES, which measures the concentration of all the dissolved species. The instantaneous dissolution rates (v_M, in µg s^{-1} cm^{-2}) of the alloy components are monitored (as a function of time) and can be related to the concentrations of released elements, C_M (in ppm) by:

$$v_M = C_M f / A \quad (1)$$

where f is the electrolyte flow rate (in ml min^{-1}) and A is the exposed surface area of the alloy (0.5 cm^2). To express the dissolution rate as an equivalent current density, it is possible to apply Faraday's law, giving:

$$j_M = zF v_M / M \quad (2)$$

where z is the oxidation state of the dissolved species and M the molar mass.

The flow cell employed has two compartments, with one housing the reference and counter electrodes, and the other compartment housing the working electrode. The compartments are separated by a porous membrane of natural cellulose. The flow rate was measured prior to each experiment and was determined to be 3.01± 0.01 mL min^{-1}. The electrolyte was maintained at a constant temperature with a water bath system and was also controlled at the backside of the sample by placing it in contact with a hollow copper block, connected to the recirculating temperature controlled water bath.

The ICP-AES system used herein was a Horiba Jobin Yvon Ultima 2C. The system setup consisted of a 50 cm focal length Paschen-Rungen type polychromator, with an array of photomultiplier tube detectors at specific wavelengths and a monochromator (1 m focal length). The monochromator was calibrated on the Li 670.784 nm wavelength for this study.

The emission wavelengths for the elements Al, Mg, Cu, Fe, Mn and Li, and their detection limits, were calculated and determined for all the electrolytes used and reported in **Table 13.**

Table 13 : Detection limits ($C_{2\sigma}$) of the elements analyzed in the different electrolytes.

Element	*Wavelength, nm*	$C_{2\sigma}$ *in NaOH, ppb*	$C_{2\sigma}$ *in water, ppb*	$C_{2\sigma}$ *in* HNO_3*, ppb*	$C_{2\sigma}$ *in NaCl, ppb*
Al	396.152	5.1	3.3	4.2	10
Li	670.784	3.8	1.1	6.5	3.1
Mg	279.079	Not soluble in	0.6	2.3	2.8
Cu	324.754	NaOH,	3.4	4.2	4.4
Mn	257.610	analysis	1.8	2.8	1.6
Fe	259.940	performed in water	9.1	6.1	5.2

A second peristaltic pump was connected to the system after the electrochemical flow cell to inject 2.8 M nitric acid containing 15 ppm Y as an internal standard at 1 mL min^{-1}. The idea was to neutralize NaOH solution before being analyzed by the ICP to make less insoluble species like Mg, Mn, Cu and Fe easier to detect. The electrolyte introduction system for the ICP, was a TR-30-K3™ Meinhard nebulizer, which is used for high solid content electrolytes and a cyclonic aspiration chamber.

The electrochemical experiments (open circuit potential and polarization) were performed using a Gamry Reference 600™ potentiostat with an Ag/AgCl reference electrode and a Pt wire counter electrode.

Microscopy and Surface Topography Surface observation and characterization was carried out using an FEI Quanta 3D FEG scanning electron microscope (SEM) coupled with energy dispersive X-ray spectrometry (EDXS). Elemental depth profiles were performed before and

after the experiments using a Horiba Jobin Yvon GD profiler 2 glow discharge optical emission spectrometer (GD-OES).

3. RESULTS

The complete pretreatment sequence corresponds to: a) 1.25 M NaOH at 60°C during 5 min, b) deionized water rinse at 23 °C during 5 min, c) 2.8 M HNO_3 at 23°C for 15 min, and d) deionized water rinse at 23°C for 5 min. The sequence and procedure are identical to the one used for the AA2024-T3 [128].

3.1. Dissolution profile AA2050-T3 under pretreatment sequence

The dissolution profile of AA2050-T3 during a complete pretreatment sequence (**Fig. 38**) gives as a function of time the Al, Li and Cu dissolution rates. The electrochemical potential, E, is also presented. Note that the Li signal has been multiplied by 10. The exposure consists of (1) 1.25 M NaOH at 60°C during 5 min, and (2) a water rinse during 5 min at 23°C and (3) 2.8 M HNO_3 exposure at 23°C during 15 min.

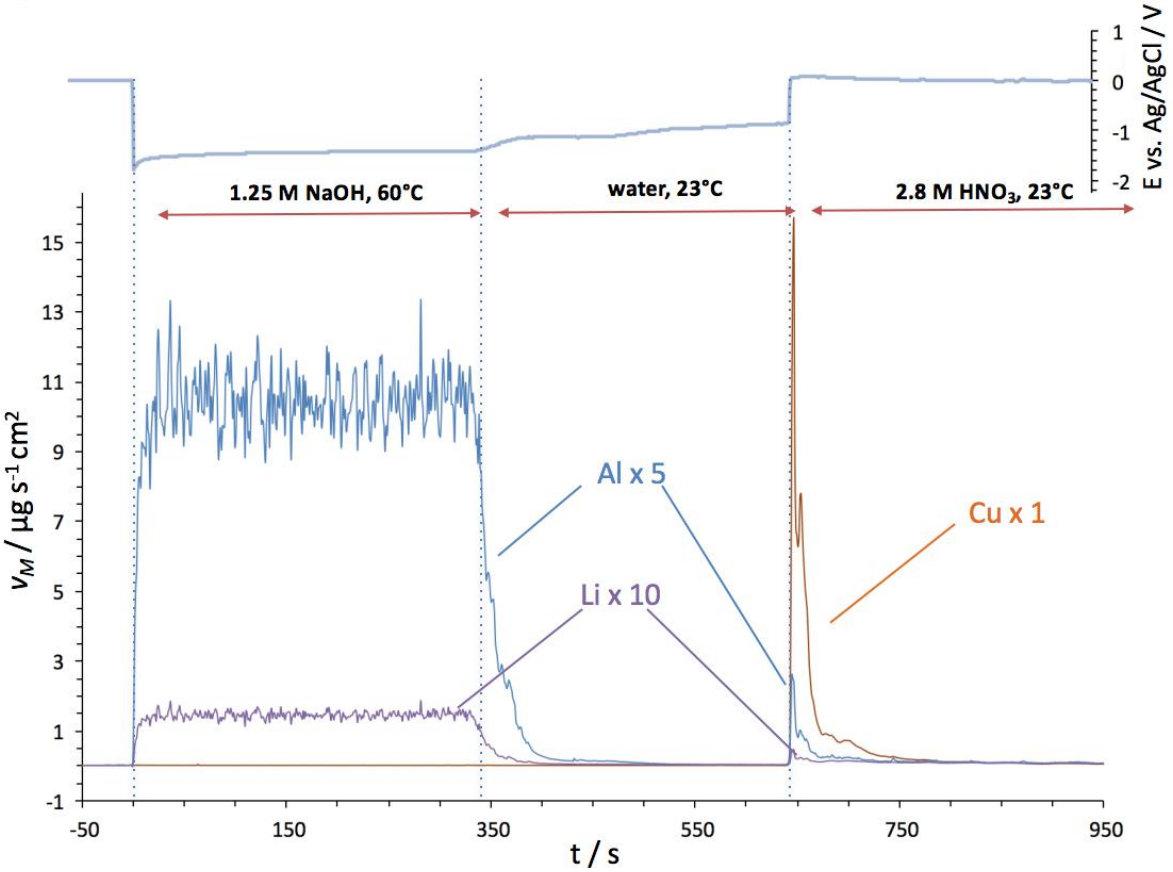

Figure 38: Dissolution profile of AA2050-T3 during a complete pretreatment sequence. Shown as function of time: Al, Li and Cu dissolution rates in µg s^{-1} cm^{-2} and the potential in V vs. Ag/AgCl. Note that the Li dissolution rate has been multiplied by 10.

When the 1.25 M NaOH enters in contact with the alloy at t=0, the Al dissolution rate rises rapidly to reach a relatively steady state value of ~ 2.6 µg s^{-1} cm^{-2}. The extensive oscillations of the Al signal are caused by hydrogen formation during the course of the experiment. The

dissolution profile looks similar to the results obtained during the AA2024-T3 pretreatment sequence [128], however, two important differences need to be taken into account: the Al dissolution rate is lower than the value measured with AA2024-T3 (13.4 µg s^{-1} cm^{-2}) and Li dissolution occurs during the NaOH exposure (~ 0.1 µg s^{-1} cm^{-2}). This experiment shows that Li is preferentially dissolved during this stage of the pretreatment as the rate is approximately 9 times the expected value for congruent dissolution. For Li, this value would be 0.017 µg s^{-1} cm^{-2} based on the Al dissolution rate assuming that Al oxidation leads to soluble $Al(OH)_4^-$.

On the other hand, the potential has a similar value as that measured for the 2024, which is above the activation potential for Li [2] and explains its dissolution during this experiment. When the electrolyte enters in contact with the surface, the potential rises to a value of ~ -1.2 V vs Ag/AgCl, and remains stable. During the water rinsing, the Al and Li dissolution rates decrease slowly - within 200 s - to reach a level close to the background level. Moreover, the potential value rises steadily to stabilize at ~ -0.8 V vs Ag/AgCl. The release of intermetallic particles was also observed during the this period and was analyzed at a high data collection rate (10 Hz) as will be discussed in another section.

When HNO_3 is introduced to the system, the surface reacts immediately with the electrolyte and instantaneous peaks of Cu, Li and Al (and other elements not shown here but described in detail later) appear in the first stage of the experiment and decrease after approximately 150 s. These results were also presented in integral form to quantitatively determine the evolution of the cumulative mass of the elements caused by the Al dissolution. The quantity of Al dissolved, Q_{Al}

$$Q_{Al} = -\int_0^t v_{Al}\, dt \tag{3}$$

is shown on the left hand axis of **Fig. 39** as a function of time. Note that the negative sign indicates a mass loss. Assuming that the alloy composition is uniformly distributed in depth at t=0, and that all oxidized Al is soluble, the quantity of residual metal M (M= Cu and Li), may be determined by a mass balance in Equation 4:

$$Q_M = -x_M Q_{Al} - \int_0^t v_M\, dt \tag{4}$$

where $x_{Cu} = {}^{Cu\ w\%}/_{Al\ w\%}$ = 0.035, and $x_{Li} = {}^{Li\ w\%}/_{Al\ w\%}$ = 0.0081 the ratios determined from the bulk alloy composition given in **Table 12**. Q_{Cu} and Q_{Li} are also shown as a function of time on the right hand axis of **Fig. 39**. During the NaOH exposure, a large Al and Li mass loss occurs, reaching a value of -500 µg cm^{-2} for Al and -47 µg cm^{-2} for Li after only 5 min. On the other hand, Cu accumulates at the surface and Q_{Cu} reaches a value of approximately + 25 µg cm^{-2} after NaOH exposure. These values remain stable during the water rinse for the

three elements. However, when the surface is exposed to HNO_3 treatment, the Q_{Cu} decreases dramatically to reach a steady state value at 1200 s, corresponding to a Q_{Cu} of -175 µg cm^{-2}. It is noted that the amounts of Al and Li dissolved during the HNO_3 treatment (~ - 3.1 µg cm^{-2} for Al and ~ - 6.2 µg cm^{-2} for Li) are very small compared to the quantities dissolved during the NaOH treatment (-500 µg cm^{-2} for Al and ~ - 47 µg cm^{-2} for Li). This experiment clearly indicates the impact of the NaOH treatment. During NaOH exposure, the oxidized Al is soluble and Li reactivity is enhanced. Moreover, after this step, only minor amounts of Li and Al remain on the surface as a film.

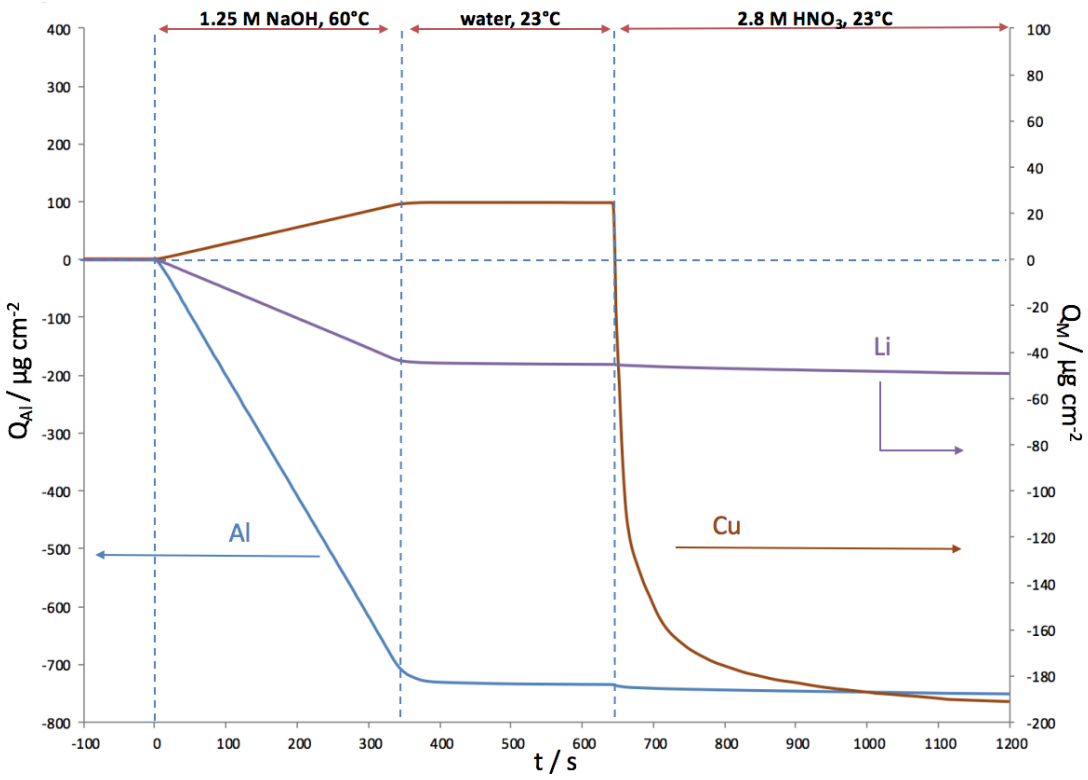

Figure 39: Evolution of the Al, Cu and Li mass, Q_M, as a function of time during the pretreatment (in µg cm^{-2}). Al was calculated as a mass loss by direct integration of Al dissolution profile (Eq 4.). Cu and Li were calculated as residual films from equation 5 assuming homogeneous elemental composition at t=0.

The same sequence was applied to the AA2023-T3 alloy and both alloys reacted differently in spite of their similar Cu content. Indeed, the formation of a Cu containing residual film was evidenced[128] for AA2024-T3 while preferential alloying element dissolution, particularly Cu, is demonstrated for AA2050-T3.

3.2. Reactivity of AA2050-T3 under HNO3 exposure

A typical dissolution profile of AA2050-T3 under HNO_3 exposure is shown in **Fig. 40** where Al, Cu, Li, Fe, Mn and Mg dissolution rates are given as a function of time along with the potential (E in V vs. Ag/AgCl). For more clarity, the upper curves show the Cu, Mg and Mn dissolution rates and the second series show the Al, Fe and Li dissolution profiles.

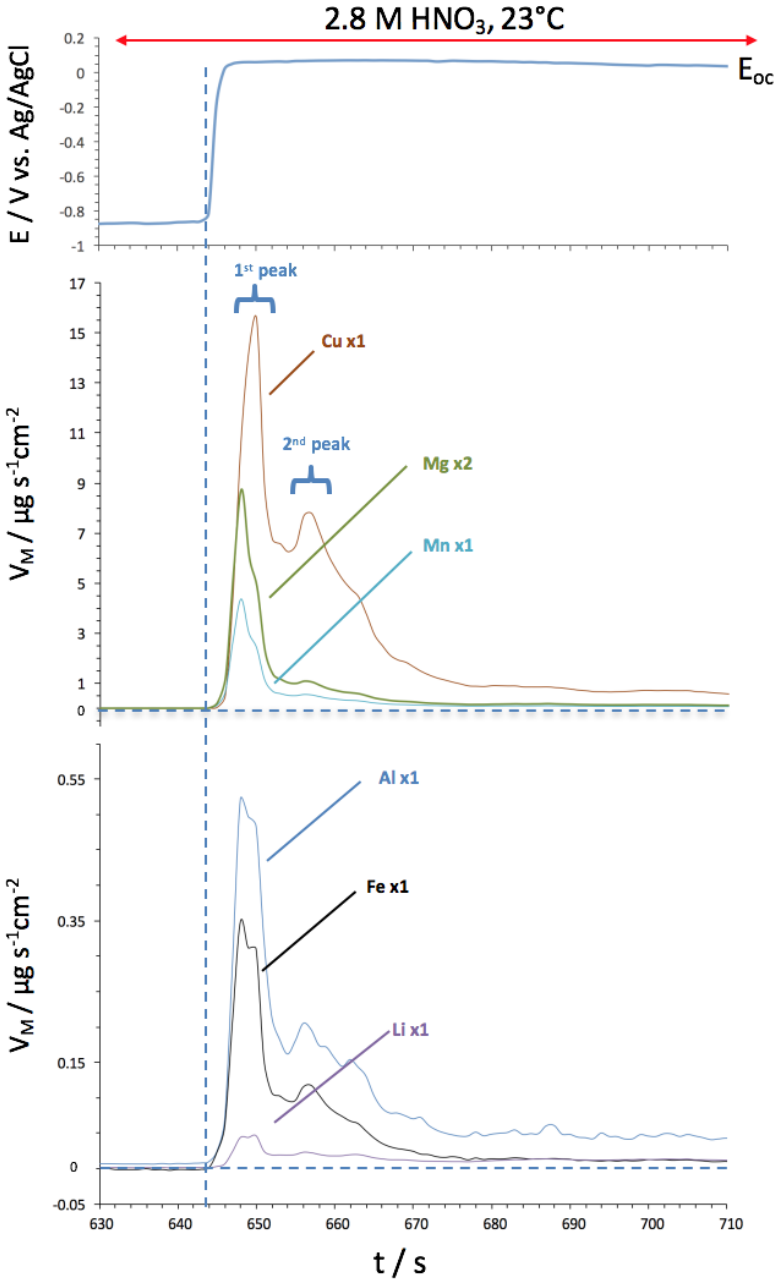

Figure 40: Dissolution profile of AA2050-T3 during HNO_3 exposure where E (upper curve) and Cu, Mg, and Mn (middle) and Al, Fe, and Li (lower) dissolution rates are shown as a function of time.

When the HNO_3 solution reacts with the sample, sharp peaks of Cu, Al, Mg, Fe, Mn and Li rise simultaneously and last approximately 8 s. This is followed by second distinct peaks of Cu, Al and Fe. Meanwhile, Li, Mg and Mn continue to dissolve with relatively stable values. These

results highlight similarities with the AA2024-T3 experiments with the instantaneous dissolution of alloying elements components corresponding to the first peak. This is most likely caused by the dissolution of a residual film composed of Al, Cu, Mg, Fe, Li and Mn hydroxides which reacts immediately with the HNO_3. The second peaks however may correspond to the dissolution of what could be attributed to intermetallic particles. Nevertheless, it is important to note a major difference in the elemental dissolution profiles of HNO_3 as compared with NaOH, as the majority of the dissolution occurs during the first 30 s. In AA2024-T3 pretreatment, it has been shown that the reactions under HNO_3 exposure were completed after ~ 200 s [128]. Moreover, during the NaOH exposure, it has been reported that the Al was selectively dissolved leading to particle enrichment at the surface and leaving a residual layer composed of Al, Cu and Mg hydroxide layer and intermetallic particles surrounded by Al/Mg hydroxide film [16,128,154]. These particles were afterwards dissolved by the HNO_3 but react more slowly than the hydroxide layer which was instantaneously dissolved by the electrolyte. Considering that the AA2050-T3 seems to have less intermetallic particles than the AA2024-T3 alloy and the reaction in HNO_3 is limited by the quantity of intermetallic particles in the film, it is possible to assume that the proportion and size of the big constituent particles in the film strongly affects the reaction during HNO_3 exposure. Indeed, the higher the number of large constituent particles at the surface, the longer their dissolution will last.

Assuming that only the dissolution of the residual film occurs in HNO_3, the quantities of Al, Mg, Cu, Fe, Li and Mn were calculated from the integral of the data presented in **Fig. 40** and are reported in **Table 14**. The results show that Cu is the element which contributes the most to the residual film composition, followed by Mg and Al. On the other hand, Mn, Fe and Li are only present in minor quantities.

Table 14 : Elemental composition and absolute quantity of the residual film after NaOH exposure (calculated from integral of Fig and mass balance).

Element	*Al*	*Cu*	*Mg*	*Fe*	*Mn*	*Li*
Concentration ($\mu g\ cm^{-2}$)	15.3 (5.2 %)	215.2 (73.3 %)	26.0 (8.8 %)	4.5 (1.5 %)	28.6 (9.7 %)	3.8 (1.3 %)

3.3. Microstructural analysis of AA2050-T3 before and after pretreatment

The surface morphology of AA2050-T3 before pretreatment is presented in a SEM micrograph in backscattered electron mode, (**Fig. 41**) at a relatively low magnification (x 500). The surface exhibits a high density of small particles spread over the surface all with different shapes and sizes. The majority of the intermetallic particles seem to have an average size of > 1 µm with a few very large particles (~ 10 µm). The latter are irregularly shaped, and could correspond to

Al(Cu-Fe-Mn) constituent particles. These coarse constituent particles need to be removed from the surface as they form from impurities (Fe) and decrease the fracture toughness and promote localized corrosion [69,70,73]. EDS mapping was carried out on one of these particles to determine its chemical composition and the result (**Fig. 41)** reveals an Al(Cu-Mn-Fe) constituent particle.

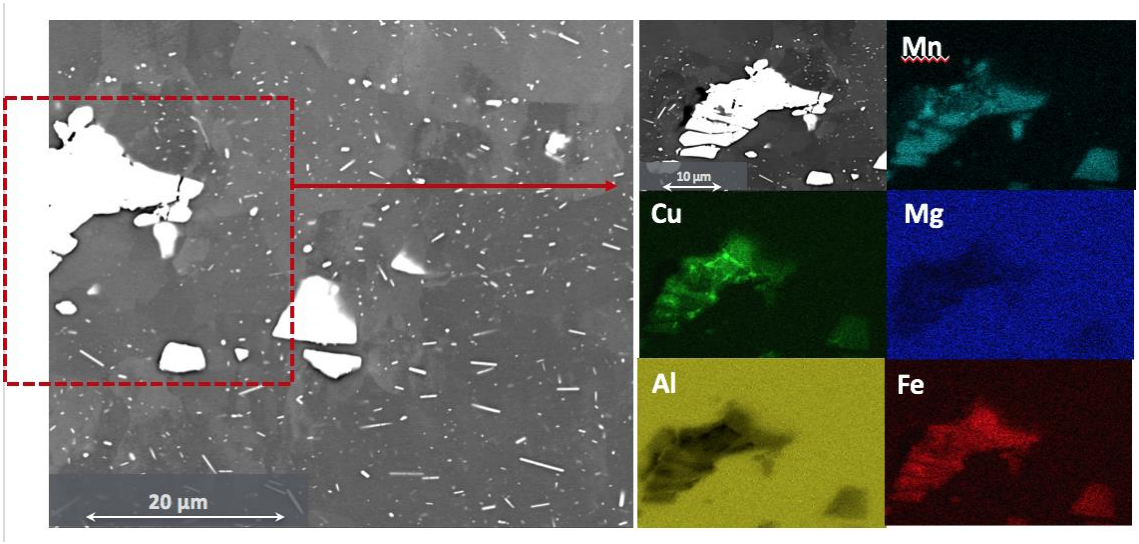

Figure 41: SEM micrograph of AA2050-T3 before surface treatment in backscattered electron mode of AA2050-T3 and the corresponding X-ray mapping of one constituent particle showing the surface composition of Fe-Cu and Mn. Note that the rectangle on the left does not correspond precisely to the EDS mapping area on the left.

On the other hand, some particles are homogeneously distributed in the matrix and are laths shaped. These particles have a size of between 50 to 200 nm and could correspond to the T_1 (Al_2CuLi) or the S (Al_2CuMg) phase. These phases are the most prominent phases in the Al-Li with > 1% Li content and contribute to the mechanical properties [70]. The microstructural analysis clearly emphasizes the effect of the Li addition on the Al microstructure in terms of particle composition, sizes and distribution.

After NaOH exposure, the surface (**Fig 42. A**) shows a very different surface morphology, as in this case, the micrograph reveals a highly heterogeneous surface, with the evidence of surface cracking and several intermetallic particles on the surface. EDS analysis realized on the big particle reveals a Fe enriched particle, on the other hand, the matrix seems to be Al and O enriched, showing that the surface is mainly an Al oxide/hydroxide film formed during the NaOH exposure. In the second SEM micrograph taken in backscattered electron mode (B), the cavities on the surface suggest that the intermetallic particles have undergone active dissolution during HNO_3 exposure. However, the EDS mapping shows that some of the (Al)-Cu-Mn-Fe coarse particles remain on the surface and that they are not affected by the pretreatment.

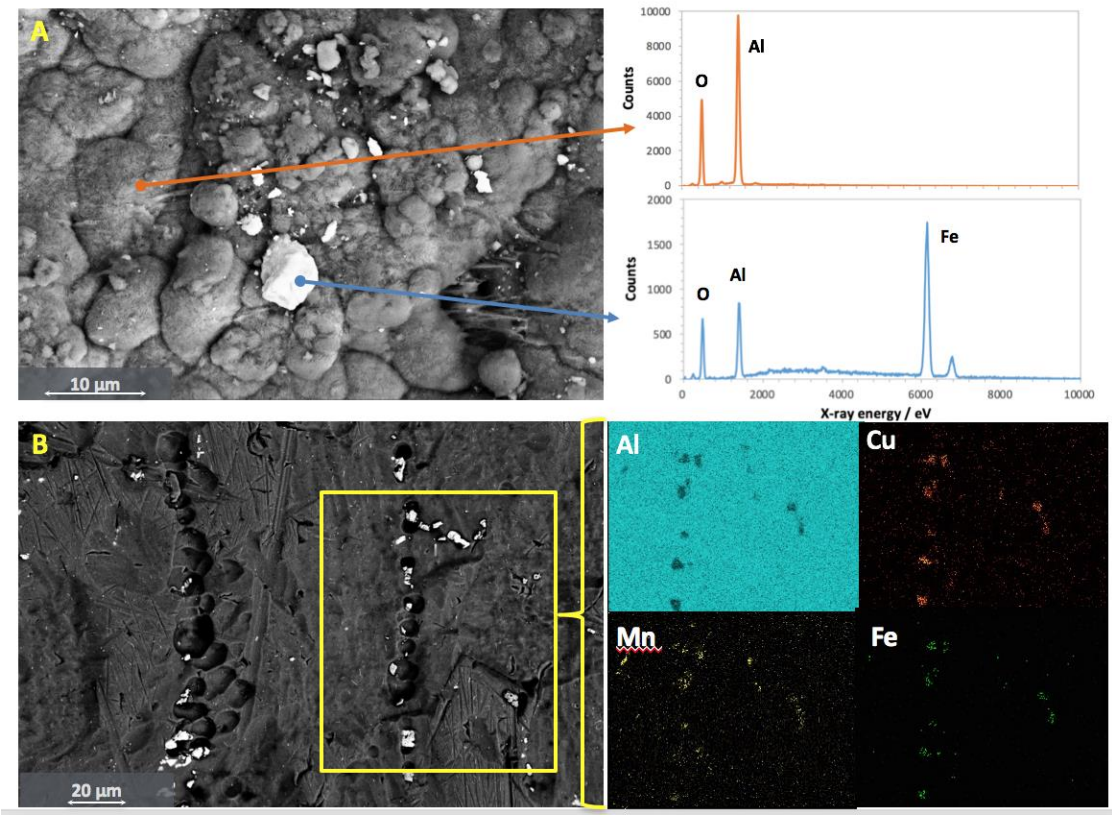

Figure 42: SEM micrographs after 5 min NaOH at 60°C exposure in backscattered electron mode of the surface (A) and the corresponding EDS spectras of one particle and the matrix. (B) represents the surface after HNO_3 exposure with the corresponding mapping showing the chemical composition of the remaining particles.

3.4. Particle detection under NaOH exposure

The particle detachment was investigated during the exposure to NaOH and the results are represented in **Fig. 43** were Mg, Cu, Fe and Mn signal are shown as a function of time. The data acquisition was acquired at 10 Hz in order to increase the spatial resolution of the peaks. During the experiment, the Cu signal correlates with either the Mg signal or with the Fe and Mn signals, suggesting two distinct particle compositions that are distinguished by the AESEC method. Moreover, the most intense Cu peak correlates with the most intense Mn peak. Interestingly, the Mn signal rises during the course of the experiment, sometimes with the presence of peaks which appear only during the first part of the experiment. The Mn dissolution profile accompanied with transients could be ascribed to the dissolution of the Mn rich particles. The addition of HNO_3 to the flowing electrolyte via the second pump probably results in the dissolution of the majority of the particles like the $Al_{20}Cu_2Mn_3$[59,70] dispersoids or the Al_6Mn constituent particles, before being analyzed by the ICP-AES. Indeed, before pretreatment, the SEM micrographs of AA2050-T3 demonstrated the presence of relatively few big intermetallic particles with an average size of ~ 8 µm. It has been shown in a previous study that only particles under the size of approximately 10 µm were analyzed by the ICP-AES (although the nebulization conditions of those experiments were not identical to the present work) [117]. In

the case of this alloy and from the SEM micrographs, their sizes do not exceed 15 µm, thus the majority of the particles released are probably analyzed by the ICP-AES.

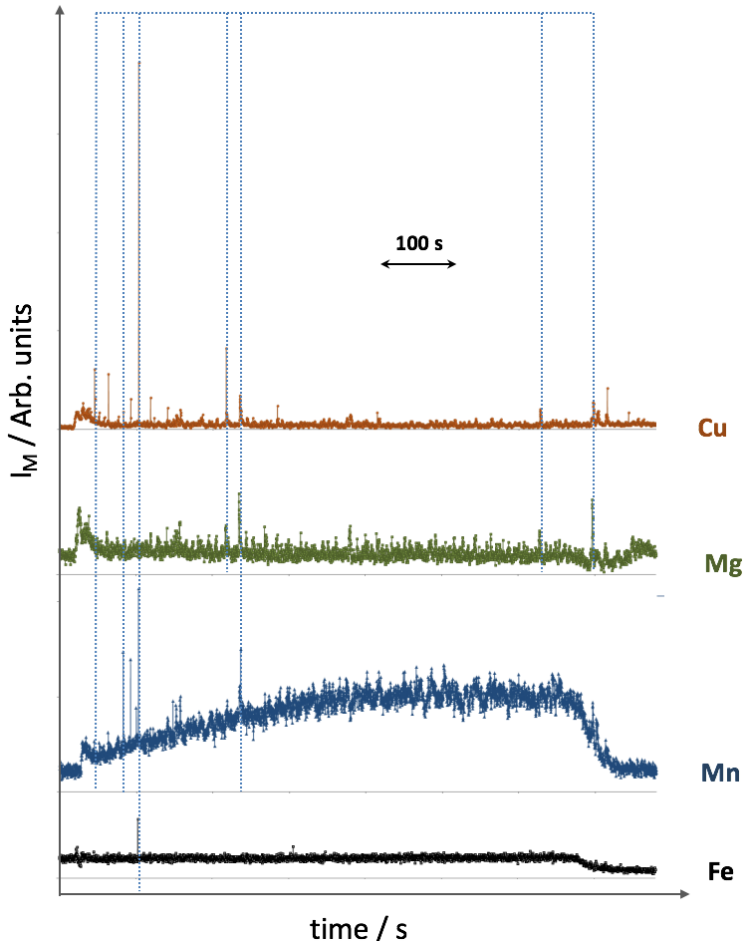

Figure 43: Dissolution profiles during NaOH exposure of AA2050-T3 at 10 pts/s showing Cu, Mg, Mn and Fe. The very sharp spikes indicated with a vertical line are attributed to the release of intermetallic particles.

3.5. AESEC polarization curves prior & after pretreatment

The AESEC polarization curves of AA2050-T3 in 0.5 M NaCl at pH= 6.7 before and after pretreatment are shown in **Fig. 44**. Expressed as a function of the potential (in V vs. Ag/AgCl), the total current density j, and j_{Al}, j_{Li} and j_{Cu} calculated from their dissolution rates using Faraday's law (assuming n=3 for Al, n=1 for Li, n= 2 for Mn). The idea was to investigate the effect of the pretreatment on the electrochemical reactivity of the surface. The effect of the pretreatment is clearly visible on the conventional potentiodynamic polarization curves (**Fig. 44A**), as after pretreatment, the cathodic current density decreases by approximately one order of magnitude. This result is consistent with the SEM and AESEC analysis showing the particle removal during the pretreatment sequence. The second noticeable effect is the increase of the pitting potential but also the anodic current decreased almost one order of magnitude between the corrosion potential (-0.5 V and -0.4 V vs. Ag/AgCl). From these polarization curves

presented herein, the pretreatment seems to have a similar effect as for AA2024-T3, presented previously [128].

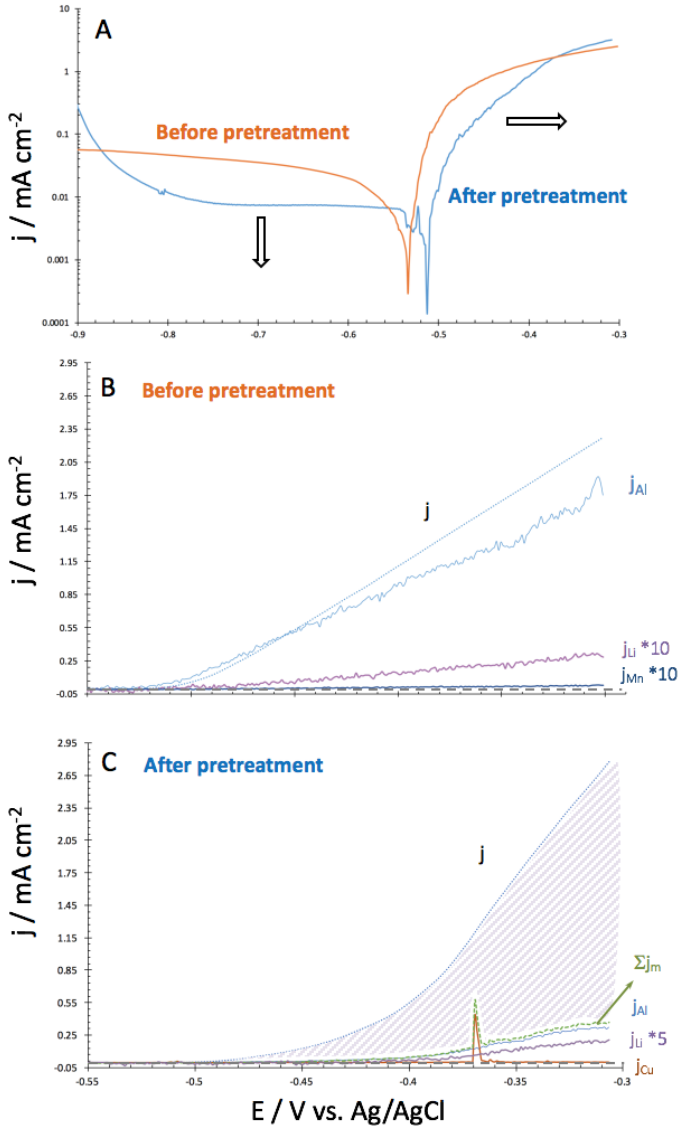

Figure 44: Potentiodynamic polarization curves of AA2050-T3 before and after pretreatment in 0.5 M NaCl, 1 mV s^{-1}, pH 6.8 at T= 23°C. A/ represents the conventional polarization curves, B/ and C/ their corresponding dissolution profiles in the anodic domain before pretreatment (B) and after pretreatment (C). The dashed area in (C) indicates the difference between J_e and ΣJ_m, which is attributed to oxide formation.

On the other hand, (**Fig. 44B**) and (**Fig. 44C**) represents the AESEC polarization curves corresponding to the anodic domain. Before pretreatment (**Fig. 44B**), the Al signal starts to rise progressively following the total current measured by the potentiostat (j). Interestingly, only the Mn and Li signals increase (Mn and Li signals have been multiplied by 10 for more visibility), and Li appears to be dissolving 1.5 times more rapidly than what is expected for congruent dissolution. During the experiment, the Cu, Mg and Fe signal were below the detection limits. After pretreatment, the AA2050-T3 dissolution profile (**Fig. 44C**) shows a

very different behavior than what was observed before pretreatment. Indeed, when the total current j starts to rise, Σj_M - which represents the sum of all the dissolution currents measured by ICP-AES - is 10 times lower than the total current. This difference was attributed to the formation of an oxide which acts as a protective layer regarding the matrix. From the AESEC results, it is possible to monitor the formation of an oxide at the surface which is not possible to detect via conventional potentiodynamic polarization curves.

Meanwhile, during the anodic polarization, only Al and Li are dissolving (Mg, and Fe signals were below the detection limits), and a sharp peak of Cu was observed at -0.37 V vs. Ag/AgCl which can be attributed to a particle detachment. Nonetheless, this dissolution profile does not indicate the presence of Cu particles remaining on the surface as was revealed on the AA2024-T3[128], which is in a good agreement with the results presented in **Fig. 39**. From these values, the Li dissolution rate seems to be lower than what would be expected for stoichiometric dissolution that could suggesting some Li enrichment at the surface of the alloy. However, it is important to note that the surface composition of the alloy is changed after pretreatment as the x_{Li} is lower than what was determined previously from the bulk composition. Interestingly, this phenomenon occurs only after the surface treatment, when the majority of the intermetallic particles are removed from the surface.

3.6. GDOES profiles of the surface after pretreatment and polarization curves

Further investigation of the surface was conducted by GDOES to determine if any Li enrichment could be detected at the surface. Two experiments were realized by GDOES and are illustrated in **Fig. 45** which gives Li/Al ratio profiles as a function of the erosion time. The orange curve corresponds to the AA2050 matrix and the blue curve to the sample after pretreatment and polarization.

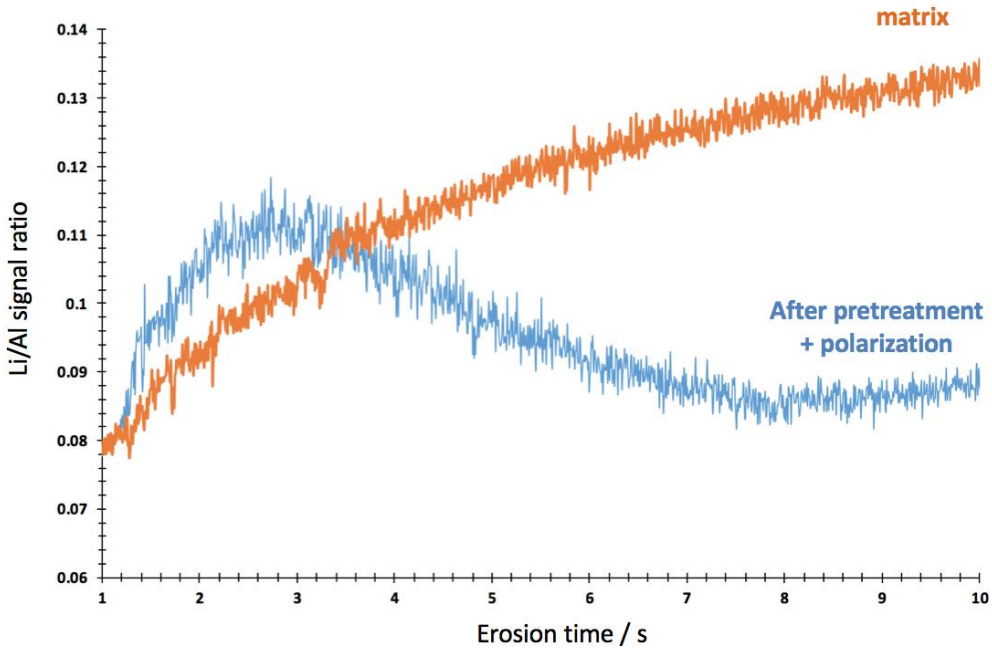

Figure 45: GDOES profiles of AA2050-T3 before and after polarizing. The Li/Al ratio is represented as a function of the erosion time indicated a Li enrichment at the surface.

For the AA2050 matrix, Li/Al ratio signal of the bulk alloy rises steadily to reach a value of 0.13 after 10 seconds. On the other hand, after pretreatment and polarization, the Li/Al ratio rises more rapidly to reach a higher value (than the other curve at 3 seconds of erosion time 0.10 for the matrix and 0.11 for the treated sample). Then it decreases and stabilizes down to a steady value of 0.09 at 10 seconds. This result clearly indicates that the quantity of Li at the surface of the alloy is higher than what is in the bulk alloy and strongly suggests a surface enrichment of Li on the alloy, probably a Li/Al oxide formed during the anodic polarization of the sample.

3.7. Potentiodynamic polarization curve of AA2024-T3 in 0.5 M NaCl with the addition of 1 ppm of Li

A final experiment was realized to clearly demonstrate the effect of Li addition in the anodic dissolution profiles and the formation of an eventual oxide film. An AA2024-T3 sample was pretreated and a potentiodynamic polarization curve was realized in the same condition with the addition of 1 ppm of Li to the 0.5 M NaCl solution. The Al, Cu, Mn Mg and Fe dissolution profiles expressed as a current density using Faraday's law and the total current measured (j_e), are represented as a function of the potential E vs. Ag/AgCl in **Fig. 46** (between -0.9 V and -0.45 V vs. Ag/AgCl). Interestingly, the dissolution profile of AA2024-T3 looks different to what was reported previously on AA2024-T3 after treatment[128] and was very similar to the AA2050-T3 after pretreatment. The total current in the anodic part j_e, is higher than the current

measured by AESEC by approximately one order of magnitude. With this experiment, it was possible to isolate the effect of Li addition on the reactivity of the alloy.

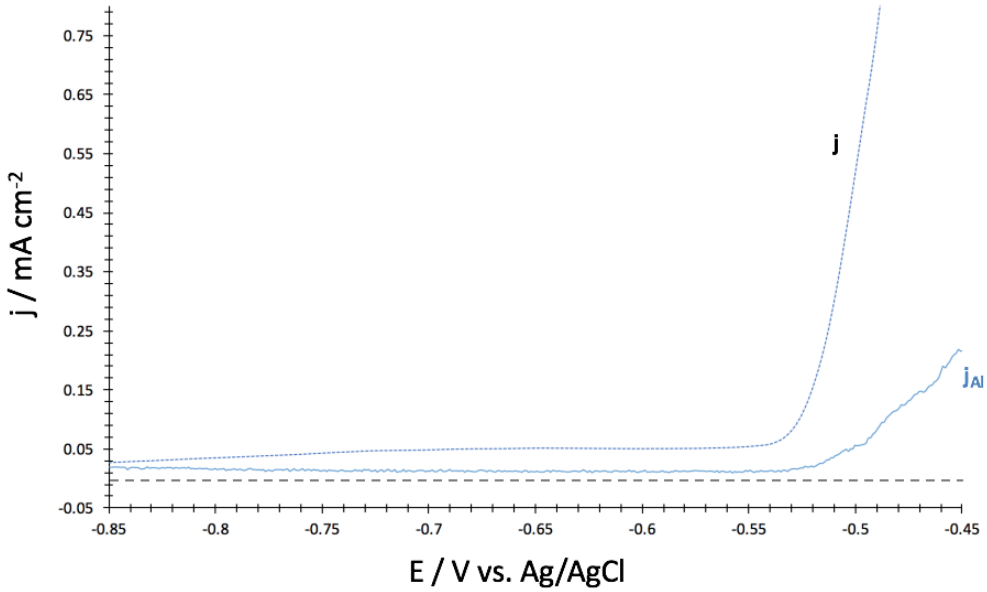

Figure 46: Potentiodynamic polarization curves of AA2024-T3 after pretreatment in 0.5 M NaCl + 1 ppm of Li at 1 mV s^{-1}, pH= 6.7 at T= 23°C. Represented as a function of the potential, the total current and j_{Al}. Note that the Al was the major element contributing to the total current.

4. DISCUSSION

A study from Buchheit et al. [155] in the context of alkaline cracks in Al-Li alloys reported that during the corrosion process of Al in NaCl media, for each Al^{3+} cation produced, there was a net gain of 1 H^+:

$$Al \rightarrow Al^{3+} + 3e^- \quad (5)$$

$$3H^+ + 3e^- \rightarrow {}^3/_2 H_2 \quad (6)$$

$$Al^{3+} + 4H_2O \rightarrow Al(OH)^-{}_{4(aq)} + 4H^+ \quad (7)$$

Moreover, the alloying elements such as Cu, Mg and Fe follow a similar dissolution hydrolysis reaction resulting in the generation of more H^+ cations during the dissolution process. These reactions usually do not favor a local pH increase in the majority of Al alloys and explain why, when a crack forms, the local pH does not exceed 8.

Nevertheless, it has been shown that the addition of Li changes the reactivity as the dissolution of Li results into an increase of the pH:

$$Li \rightarrow Li^+ + e^- \quad (8)$$

$$H_2O + e^- \rightarrow {}^1/_2 H_2 + OH^- \quad (9)$$

as Li^+ is not significantly hydrolyzed [156]. Consequently, for one Li^+ cation generated, one OH^- is produced. In their study, this local alkalization at the subgrain boundaries leads to the precipitation of a hydrotalcite film $Li_2[Al_2(OH)_6]_2CO_3{\cdot}3H_2O$ in 3.5 wt % sodium chloride (NaCl) media during anodic dissolution, passivating the SGB fissure walls.

These observations and our results show some similarities as the formation of a Li film occurs after the removal of intermetallic particles. The possibility of a pH increase could be valid only if the Li dissolution is more important than Al oxidation. Nevertheless, the Al and Li dissolution profiles are not stoichiometric (Al dissolution rate is 3 times higher than Li), which means that the hypothesis of having a significant alkalization at the interface electrolyte / metal is very unlikely to happen. Li precipitation/enrichment could however be explained by the presence of a hydrous aluminum oxide gel, formed by the hydrolysis of Al^{3+} cations. This gel could create a sort of confined environment and act as a barrier for the Li^+ cations leaving the matrix and also promote a local increase of pH caused by the Li oxidation **(Fig.47).**

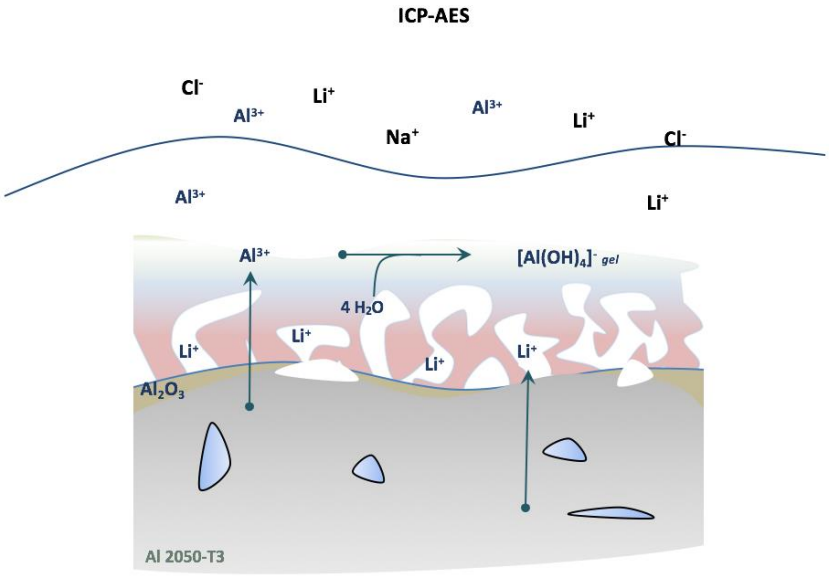

Figure 47: Schematic of the dissolution/ precipitation process of Li and Al during the anodic polarization of AA2050-T3 after pretreatment.

5. CONCLUSIONS

The dissolution of aluminum alloy AA2050-T3 was quantified during a complete surface pretreatment procedure. From the results herein, the following conclusions may be drawn:

1) During open circuit exposure to 1.25 M NaOH, selective dissolution of Al and Li was observed to occur. Specifically, from the dissolution profiles obtained and relative to the bulk alloy composition, it was possible to demonstrate preferential dissolution of Li during this alkaline treatment step.
2) Upon open circuit exposure to 2.8 M HNO_3, dissolution of alloying elements including Cu, Mg, Fe, Mn and Li is detected. By integrating the Al, Cu and Li dissolution profiles, it was possible to assess the temporal evolution of Al and Li dissolution. During NaOH exposure, a residual Cu film remained upon the surface which rapidly dissolved with subsequent exposure of the surface to HNO_3. During acid treatment, the majority of the surface reactions were completed within ~30 s. To this end, it is posited that the majority of such rapid reactions were associated with the dissolution of the residual surface film corresponding to the near-instantaneous dissolution of hydroxides. Such results demonstrate the effect of the microstructure (such as the density and the size of intermetallic particles) on the dissolution kinetics during surface treatment.
3) SEM microanalysis performed upon AA2050-T3 at the various stages of pretreatment correlates well with the results from AESEC dissolution profiles with regards to selective dissolution and its attendant influence on surface morphology. Following NaOH treatment, the surface is highly heterogeneous, with visible mud-cracks and intermetallic particles protruding from the surface. Following HNO_3 treatment, the majority of surface intermetallic particles were dissolved, leaving cavities on the surface. However, from EDXS mapping, it was possible to observe the presence of Al-Cu-Mn-Fe constituent intermetallic particles that did not seem not to be greatly affected by the pretreatment process.
4) The effect of pretreatment on the electrochemical kinetics of the AA2050-T3 surface was evidenced by the polarization curves which revealed a decrease of cathodic kinetics by approximately one order of magnitude, along with a concomitant increase of the pitting potential. Moreover, the dissolution profiles have shown a singular effect of the pretreatment as the total current j_e was ~10 times higher than j_{Al}.
5) GDOES experiments that were realized upon the AA2050-T3 surface following polarization demonstrated Li enrichment. The GDOES erosion profile expressed as a Li/Al ratio corroborates the notion of Li enrichment occurring during anodic polarization.

6) The deliberate addition of Li into 0.5 M NaCl during potentiodynamic polarization of AA2024-T3 resulted in the formation of a surface film upon the surface. This corroborates the notion of an oxide/hydroxide formation mechanism driven by the presence of Li.
7) One postulate for the observed results is that the selective removal of intermetallics (leaving an intermetallic lean surface) coupled with the effect of selective dissolution of Li, would encourage an increase in surface pH. During anodic polarization, Al hydrolysis can lead to the formation of a hydrous alumina gel at the metal/ electrolyte interface, with such a gel serving to moderate Li dissolution and promote a local pH increase leading to the formation of an Al/Li film.

ACKNOWLEDGMENTS: WE ACKNOWLEDGE THE ASSISTANCE OF PATRICK CHAPON FROM HORIBA JOBIN YVON FOR THE GDOES TESTING.

CHAPTER V: CHARACTERIZATION OF AN AL-BASED CORROSION PRODUCT AFTER THE ANODIC POLARIZATION OF AN AL-LI ALLOY.

« Lors même qu'on n'est pas le chêne ou le tilleul, ne pas monter bien haut, peut-être, mais tout seul ! »

« Even when one is not oak or a linden, do not mount high, perhaps, but it alone! »

Edmond Rostand. Cyrano de Bergerac, Acte II Scène VIII.

Characterization of an Al-based corrosion product after the anodic polarization of an Al-Li alloy.

O. Gharbi [a], N. Birbilis [b], K. Ogle [a]

[a] Chimie-ParisTech, PSL Research University, CNRS - Institut de Recherche Chimie Paris Paris 75005, France

[b] Department of Materials Science and Engineering, Monash University, VIC 3800, Australia

The chemical nature of an Al corrosion product formed during anodic polarization in 0.5 M NaCl of an Al-Li 2050 alloy was investigated. In order to determine the elemental composition as well as the chemical features of this film, Raman spectroscopy, X-ray diffraction (XRD) and Infrared spectroscopy (IR), glow discharged optical emission spectrometry (GDOES) have been used. GDOES analysis suggested the presence of a Li enrichment film at the surface. Further investigations using XRD, Raman and Infrared spectroscopy gave relevant information on the crystallinity and the chemical environment of this film. The present results collected from these different techniques lead to the conclusion a protective corrosion layer, possibly Li-enriched which has not been previously reported in this particular conditions. This corrosion product could play an important role in the corrosion protection of Al-Li alloys.

Key words: LDH, Al-Li alloys, corrosion protection

1. INTRODUCTION

The corrosion protection of Al Alloys is an essential step before their use in aircraft applications [81]. Al-Cu-Mg (especially AA 2024) alloys are extensively used for aerospace applications as they exhibit an excellent strength to weight ratio [5,6]. Nevertheless, the majority of the alloying elements and the impurities form insoluble intermetallic particles during the manufacturing process [5,6]. These particles may act as local cathodes and induce localized corrosion [1,8,150,157]. Different ways of protecting Al alloy have been developed, however, they generally involve a surface preparation and chemical coating [14,81,82,158]. To date, the majority of the chemical coatings involve Chromium VI which is recognized to be CMR (Carcinogenic, Mutagenic, Reprotoxic) and needs to be replaced by suitable alternatives. Numerous studies investigated the effect rare earth (cerium, vanadate) incorporated in a Chrome III coating, acting as corrosion inhibitors [107,108,159–161]. Moreover, it has been reported that some compounds like permanganate [162], silicate, phosphate reveal interesting results in the corrosion inhibition of Al alloys. However, to date, these "green" coatings do not provide a sufficient corrosion protection to be seriously considered as a good alternative.

On the other hand, Li addition in Al alloys has been studied since the 1970 and lead to the development of Al-Cu-Li alloy like AA2050 which is progressively replacing AA2024 [57,61,70,149]. The Li addition increases the mechanical properties, by the formation of new strengthening precipitates, but also decreases the weight of the alloy [58]. The effect of Li and its role on the corrosion susceptibility has been progressively studied [66,69,72,155]. Indeed, several researches focused on the effect of Li on the corrosion properties of the alloy and it has been pointed that Li addition may lead in certain conditions to the formation of a Li-Al doubled layered hydroxide also called hydrotalcite film [155,163,164]. Li cations were found to be incorporated into the Al-hydroxide film, forming a double layered hydroxide which was considered as a good candidate for "green" conversion coating formulations [163–169]. Lithium Aluminum double layered hydroxides (LDH) are extensively used for various applications such as catalysis, ion exchange or pharmaceuticals and have the following general stoichiometry: $M^{II}_{(1-x)}\ M^{III}_{(x)}(OH)_2[A^{n-}]_{x/n.}$ Their structure involves a positively charged brucite-type metal hydroxide layer with anions $[A^{n-}]$ intercalated and water molecules.

Buchheit et al. mentioned the presence of this film in the context of the anodic dissolution of Al-Cu-Li alloy, where during Stress Cracking Corrosion, a protective film may form at the subgrain boundaries as a result of a pH increase [155]. Moreover, the hydrotalcite Li containing films are considered as possible replacement to the chromate containing chemical coatings and have been studied and characterized using Raman spectroscopy, XRD (X-ray diffraction analysis) and SIMS (Secondary ion mass spectrometry) [163,167]. It has been shown that Li containing films enhance effectively the corrosion resistance by increasing the pitting potential and decreasing the anodic current [168–170].

A previous study highlighted the effect of the pretreatment on the formation of Li/Al film during the anodic polarization of a AA2050 alloy. The reactivity of Al alloys was monitored by the atomic emission

spectroelectrochemistry during the pretreatment followed by a potentiodynamic polarization test in NaCl. Interestingly, the preliminary results demonstrated that a Li/Al film was formed on the surface during the polarization testing pH 6.7, and only if a pretreatment was performed prior the test. It was suggested, according to the present results, to be hydrotalcite. Indeed, previous studies showed that Li can intercalate easily into Al hydroxides [171], as these amorphous layers act as good Li salts sorbents [172]. Nonetheless, the previous studies reported that hydrotalcite formation is favorable in alkaline environments which is not the case in neutral NaCl during anodic polarization.

Consequently, the aim of the study is to complete the characterization of this corrosion product formed in this AA2050-T3 Al-Li alloy in order to determine its chemical nature, and help to clarify the circumstances of its formation.

2. EXPERIMENTAL

Materials Al-Cu-Li alloy AA2050 with a 2 mm thickness was used for this study. The detailed chemical composition is given in **Table 15**. The alloy was mechanically ground to 4000 grit with ethanol and dried under nitrogen. A chemical pretreatment was realized on the sample with the following procedure: 5 min in 1.25 M NaOH at 60°C, 5 min water rinse at 23°C, 15 min in 2.8 M HNO_3 at 23°C, and finally 5 min water rinse at 23°C. This pretreatment was performed during the AESEC experiment allowing the *in-situ* analysis of elemental dissolution during the process [111]. Following the pretreatment, a potentiodynamic polarization experiment in 0.5 M NaCl was performed on the surface to where the Al/Li oxide film was formed. After the experiment, the sample was rinsed for 2 min in purified water to remove residual chloride. All reagents grade used during the experiments were provided by Sigma Aldrich and prepared with purified water (18.2 MΩ cm, from Millipore™ system).

Table 15: Elemental composition of AA2050-T3 in wt %

Al	*Cu*	*Mg*	*Zn*	*Fe*	*Li*	*Mn*	*Ni*	*Sr*	*Zr*	*Ag*	*Cr*	*Ti*	*Si*
Bal	3.30	0.32	0.02	0.06	0.77	0.39	<0.01	<0.001	0.08	0.17	<0.01	0.03	0.10

GDOES analysis Elemental depth profile of the film was performed using a Horiba Jobin Yvon GD profiler 2™ glow discharge optical emission spectrometer (GD-OES). The data collection was realized at 0.007 s integration time per point. During the experiment, signal of Al, Li, H, C, O but also Mg, Cu, Fe, Mn and Ag were recorded on the polychromator.

X-ray diffraction The crystalline structure of the film was also characterized by X-ray diffraction (XRD) with Cu Kα radiation (λ=1.54050 Å) using a PANanalytical X'Pert PRO diffractometer operating at 40 kV and 45 mA with a PIXcel detector. The data collection was carried out with an angular resolution of 0.02° and a scan rate of 0.3 s per point.

Raman spectroscopy Surface observation and film composition were investigated using a Renishaw Invia confocal Raman microscope with excitation by a Co diode Pumped Solid State (DPSS green laser 532 nm) and an edge filter focused on 1000 cm^{-1}. The exposure time was 1s and 50 accumulations were realized for each spectrum.

Infrared spectroscopy Infrared (IR) spectra were obtained from the corrosion product using a Nicolet 6700 IR spectrometer equipped with an ATR (attenuated total reflectance) accessory including a diamond crystal. The spectrometer is equipped with a nitrogen-cooled MCT (mercury-cadmium-telluride) wide band detector. For each spectrum, 256 scans were recorded in the wavelength range from 600 to 2000 cm^{-1} with a nominal resolution of 2 cm^{-1}. Moreover, the background was collected on the ATR accessory without any substrate pressed against the crystal.

3. RESULTS

3.1. GDOES analysis of the corroded surface

The identification of the corrosion product and the analysis of its composition as a function of the depth was determined by GDOES analysis and is represented in **Fig. 48**. The erosion profiles of Li, C, H, O are expressed as a ratio versus the Al signal. The result clearly shows the presence of a high concentration of C, O and H at the surface of the alloy. The C, O, and H concentrations, expressed as a function of the Al content, decrease with the erosion time. Interestingly, two spikes of C, O and H, at 2 and 3.6 s respectively suggest the detachment of a particle containing these elements. The data provided by this experiment cannot give information about the stoichiometry nor the absolute concentrations, however, the possibility of the detachment of hydrated carbonate could be a plausible assumption for this phenomenon. This hypothesis will be completed and discussed later by Raman and Infrared spectroscopy. Meanwhile, an increase of Li concentration at the surface of the alloy occurs during the first two seconds of the experiment, reaching the value of 0.116, then slowly decreases and stabilizes to a steady state value between 6 and 8 seconds. Then, Li/Al signal rises again until the end of the analysis. It is important to note that prior the corrosion test, the chemical composition of the alloy surface was Li depleted which means that the Li content in the bulk is expected to be higher than at the surface. Consequently, it is assumed that the steady state Li content reached at 6 s corresponds to the pretreated surface. The last part of the curve however, shows that the Ar sputtering is progressively reaching the bulk composition.

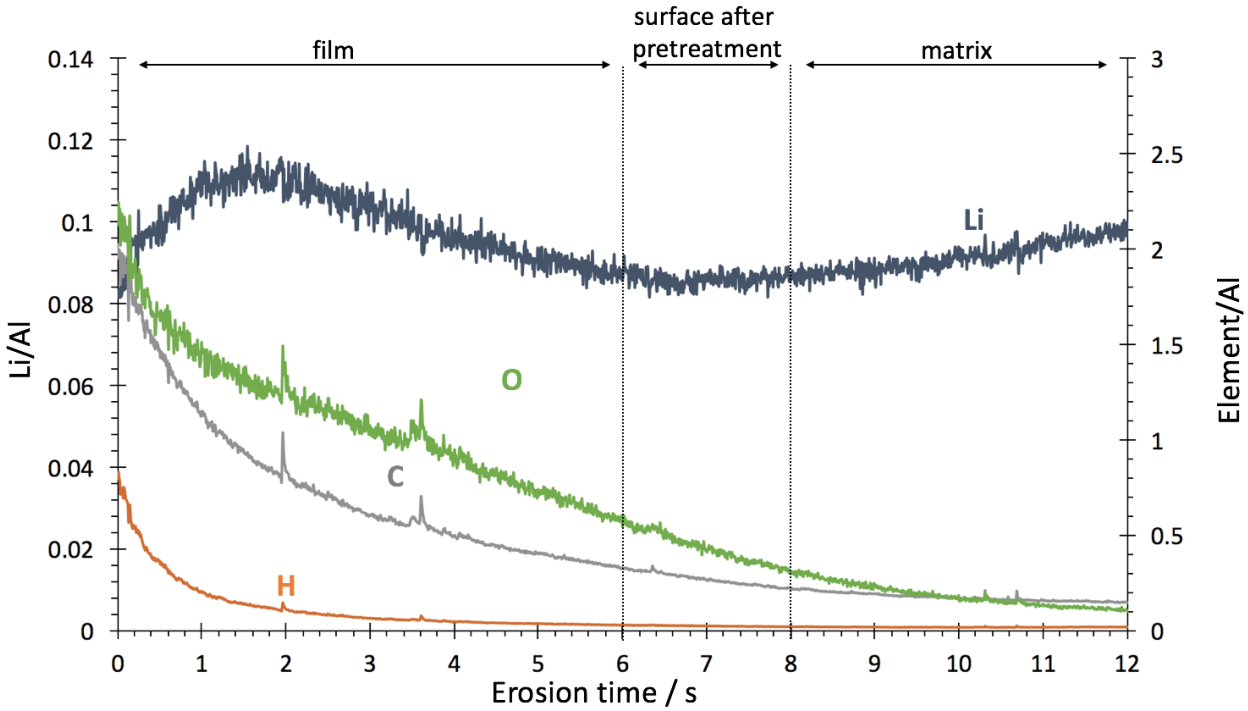

Figure 48 : GDOES profiles of Li, C, H and O expressed as a ratio versus the Al signal.

This result emphasizes the presence of a Li enriched zone encapsulated between Al oxides zones. Thus, the presence of C, H and O at high concentrations on the surface of the sample along with a Li enrichment of the alloy could be taken as a first indication of the corrosion product composition. Hence, the GDOES analysis gave access to the elemental composition of the film and suggests that this could be considered as carbonate-based corrosion products. However, with the present result, it is not possible to state with certainty that the film is Al-Li carbonate based hydroxide.

3.2. X-ray diffraction analysis of AA2050 prior and after corrosion testing

X Ray diffraction has been performed in order to investigate not only whether the Al-Li enriched film evidenced by GDOES has some degree of crystallinity but also to possibly identify its structure and stoichiometry. As presented in the introduction, hydrotalcite could be formed as the corrosion products. X-ray diffraction patterns were collected for the AA2050 bare alloy, as well as the sample after pretreatment and after the film formation. They are superposed in **Fig. 49**: this analysis allows the identification of the lines attributed to the alloy, the surface modification after pretreatment and the film. To better distinguish the modifications induced by the pretreatment or the corrosion steps compared to the matrix features, the intensities recorded have been divided by the intensity of the peak corresponding to the 2θ position at which the intensity is maximum for the matrix ($2\,\theta \cong 45.22°$).

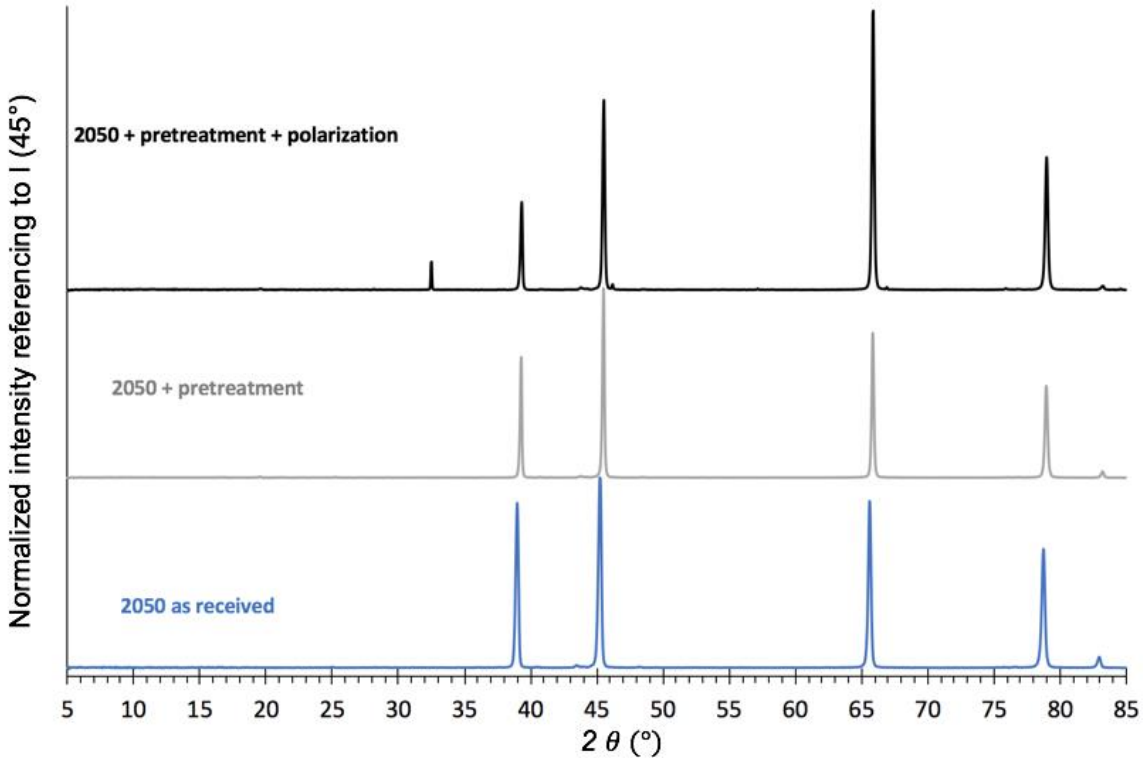

Figure 49 : Diffraction patterns of the AA2050 alloy after the different steps. Values normalized vs the intensity at $2\,\theta = 45°$, corresponding to the maximum intensity recorded for the as received 2050 substrate, after pretreatment and after corrosion test.

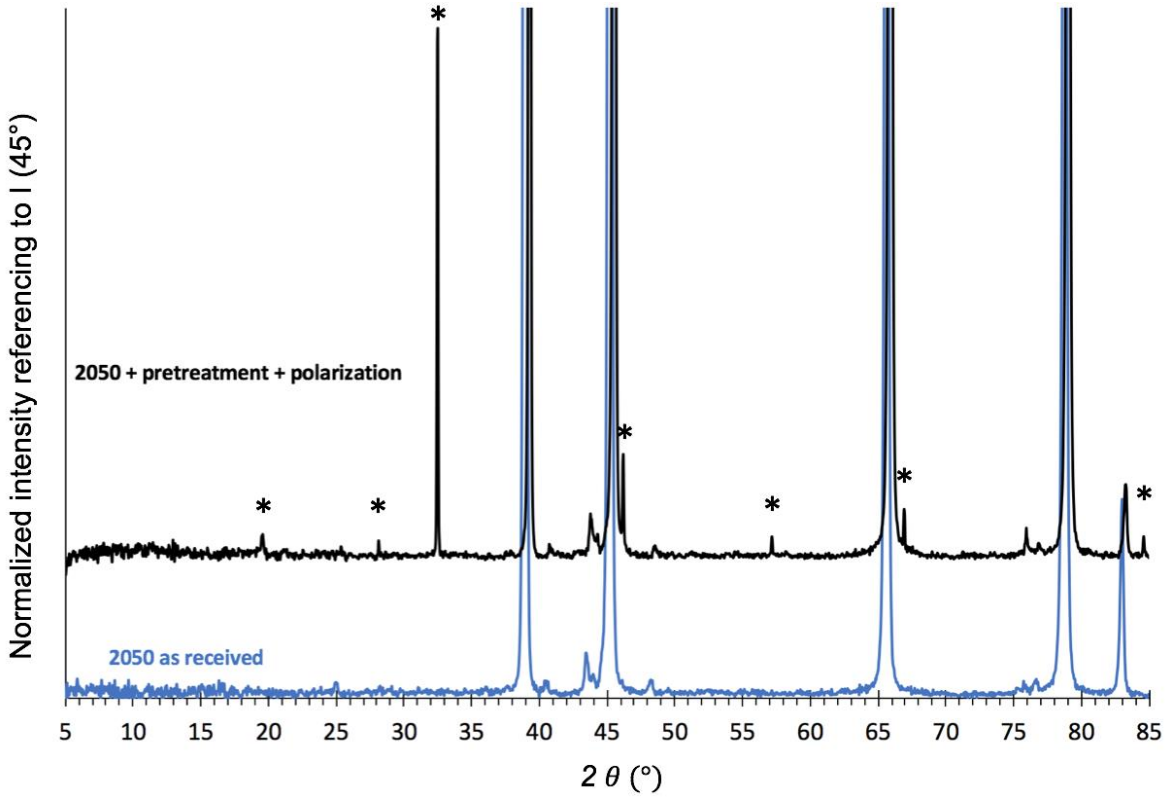

Figure 50 : Focus on the lower intensities of the X-ray diffraction patterns for the as received and after corrosion test 2050.

The fingerprint of the Al matrix is described by 5 main peaks observed for 2θ=38.99, 45.23, 65.62, 78.77° and 83.00°. This is in a good agreement with pdf file N°00-004-087 for pure Al used as the reference. Obviously, these 5 positions are slightly shifted due to the presence of the other elements in the Al matrix, and the relative intensities do not strictly respect those of the reference file. All these features are consistent as the matrix is not a pure Aluminum, but also because of the final rolling realized during the manufacturing process, inducing preferential orientations at the surface and subsurface. Furthermore, these peaks are still present for both pretreated surface and corroded surface patterns, however they are also more shifted towards higher diffraction angles and their relative intensities are different again. This corresponds to a modification of the lattice parameters of the main phase of the matrix.

Interestingly, it is worth noting that after pretreatment, the diffraction pattern does not reveal significant modifications in terms of phase formation or transformation. In contrast, after the polarization test, new narrow peaks appear on the diffraction pattern revealing the formation of a new phase(s). A focus on the lowest intense part (bottom) of both X-Ray diffraction patterns associated to the as-received 2050 alloy and the alloy after the corrosion test is illustrated in **Fig. 50**, showing the presence of 7 new diffraction lines other than the initial matrix lines, at the following 2θ positions: 19.6°, 28.14°, 32.47°, 46.2°, 57.15°, 66.9° and 84.57°. The very low width of the peaks clearly indicates that the ascribed phase(s) are well crystallized. Nevertheless, the very low intensity could be associated with the

formation of a very thin layer, and/or a thin layer related to an amorphous one acting as a mask towards the X-Ray diffraction results. These results highlight the complexity of this film and show that an accurate analysis of the corrosion product in this context is difficult. Nevertheless, two compositions can be suggested from the peak positions: Al_2O_3 (File N° 00-009-440) as a major crystallized phase, as well as lithium aluminate (α-$LiAlO_2$) when referring to Hyun and al (US Patent)[173]. This identification is reasonable considering how the phase was fabricated in the patent, mixing $Al(OH)_3$ and Li_2CO_3. It is worth mentioning that partial fingerprints of both phases are located at the same diffraction positions as the matrix, which could affect their relative intensities. Thus, to summarize the observations made:

- The matrix presents five intense reflections between 5 and 85 degrees, attributed to well crystallized Al based phases. As we knew already from the composition of the 2050 alloy, it is not only one pure Al phase, explaining the slight shifts of the ascribed peaks. Furthermore, the alloy was mechanically treated, which could modify also the intensity ratios.
- The pretreated surface conserves the main peaks of the as-received matrix, with further slight shift of the peaks and new intensity ratios.
- After polarization, additional peaks, assigned to the corrosion product appeared. At this point, Al_2O_3 could be assumed as the main crystalline phase of the film. Moreover, broader peaks were observed, corresponding to the potential formation of a few amount of less crystallized alpha-$LiAlO_2$ component.
- The corrosion product keeps the pretreated and matrix characteristics, however, the peaks are less intense (cf. original X-ray patterns in appendix). On the other hand, new narrow peaks, with low intensities are clearly recorded. They may correspond to one of the signatures of the corrosion product: Al_2O_3 is the main crystalline phase in the film, with probably a very few amount of alpha-$LiAlO_2$ component. We assume at this stage that the Li-enriched film determined by the previous GDOES analysis is an amorphous phase, giving no additional peaks by X-ray diffraction, but acting as a mask for the pretreated surface.

In the context of this study, it is not possible from X-Ray diffraction to evidence the formation of hydrotalcite films. As already mentioned, this phase is poorly crystalline in nature yielding to broad and asymmetric diffraction lines. Moreover, this could increase the difference in relative intensities of the peaks making their attribution by X-ray analysis difficult. Indeed, in the context of our study, additional parameters such as the chemical features of the alloy and the impurities, the anion size, or the degree of hydration considerably affect the X-ray pattern of the product. Thus, we pursued some complementary analysis by vibrational spectroscopies, more specifically Raman and Infrared spectroscopies.

3.3. Identification of amorphous corrosion products by Raman spectroscopy

Raman spectroscopy was used to determine whether the composition of the film shows some similarities with Raman spectra of hydrotalcites ($Li_2Al_4CO_3(OH)_{12}\cdot 3H_20$) reported in the literature, or not at all. This lithium aluminum carbonate hydroxide has been extensively studied for several applications such as Li - based conversion coatings [164–168]. Nonetheless, in the case of our study, only few researchers mentioned the presence of such product during the corrosion of Al-Li alloys [72,169]. The Raman spectra of the AA2050 matrix and the film are shown in **Fig. 51**. The bands of the Al matrix, and the film were taken in the low-wavenumber region between 200 and 1600 cm^{-1}. From the Raman spectrum of the substrate, no specific features are evidenced which confirms our X-Ray diffraction results. The spectrum shows no traces of any kind of alumina phases such as gibbsite, boehmite, bayerite or even the presence of aluminum oxide. This could be explained by the very low thickness of the native oxide which is probably difficult to detect and thus, we focused only on the film contributions. **Table 16** gathers all the vibrational modes assigned to bayerite, gibbsite and boehmite reported in literature.

Table 16: Raman vibrational modes assigned to boehmite, bayerite and gibbsite taken from the literature.

Aluminum hydroxide phase	*Vibration bands (cm^{-1})*
Boehmite RRUFF data base R120133	363 – 495- 680 – 730 -780
Bayerite and *gibbsite* [174]	242 – 255 -306 – 321 - 378- 394 - 411- 429 - 506 – 538 – 567 - 709

Raman spectra of the corrosion product layer were taken in different zones and the main results are represented by the grey and black curves in **Fig. 51**. The superposition clearly reveals the heterogeneity of the film as a corrosion product. The bands observed on the spectra could be separated into four main regions: the first corresponds to the 200 - 800 cm^{-1}, the second to the 800 – 1000 cm^{-1}, 1000 – 1200 cm^{-1} and the last corresponds to the 1200 - 1600 cm^{-1} region.

At the lowest wavenumbers (zone 1), the corrosion product gives three broad and intense bands: i) 200-400 cm^{-1} (including 242 and 318), ii) 450-680 cm^{-1}(including 589), iii) 680-760 cm^{-1} (including 730 cm^{-1}). According to Huneke et al. these bands would be ascribed to the Al hydroxide ($Al(OH)_3$) phase such as bayerite or gibbsite [174].

Zone 2 corresponds to the 800-1000 cm^{-1} region, and exhibits two distinct bands at i) 800-880 cm^{-1}(including 861 cm^{-1}) and ii) 900-960 cm^{-1}(including 919 cm^{-1}). According to Drewien's results [167], the aluminum deformation vibration bands are present in the 600-900 cm^{-1} region. However, it is clear that the bands at 861 and 919 cm^{-1} are not only due to the aluminum deformation region as the matrix does not show such peaks. Smirnov and Baddour-Hadjean, in the context of electrochemically lithiated

TiO_2 anatase for Li batteries applications, attributed these bands to the Li-O bond stretching vibrations [175].

Zone 3 comprises the 1000-1200 cm^{-1} region and exhibits two sharp bands at 1054 and 1096 cm^{-1}. It is commonly accepted that this region corresponds to carbonates. A recent study in the context of Mg/Al hydrotalcite with interlayer CO_3^{2-} showed that the incorporation of carbonate ions in the hydrotalcite structure induces a shift in the strong carbonate band υ_1 from 1063 to 1053 cm^{-1}. Klopprogge et al. stated that this shift is an indication of a lowering of the symmetry from D_{3h} to C_{2v} or C_s [176]. Consequently, the peak found at 1054 cm^{-1} can be attributed to carbonate ions incorporated into a hydrotalcite structure, as it is well known that carbonates are more readily incorporated into hydrotalcites structure due to their small size and double negative charge. A second weak band was reported at 694 cm^{-1}, however the spectrum at this value indicates a broadness which makes a clear separation between the bands difficult. The third band, corresponding to the υ_4 mode was reported to be found at 1415 cm^{-1} and could correspond to the broad and low intense peak registered at 1409 cm^{-1}(zone 4). The last band at 1096 cm^{-1}, however, may correspond to amorphous aluminum hydroxide gel according to White [177]. Moreover, the broadening of the bands was attributed to the amorphous nature of Al hydroxides yielding to various degrees of association with carbonates. **Table 17** reports the Raman vibrational modes of free carbonates and incorporated in hydrotalcites.

Drewien's reported that hydrotalcite precipitate gives sharp bands at 350, 615, 1064 cm^{-1}[167]. Parker et al. proposed three assignments for Li translational modes at 540, 412, 385 cm^{-1} [178]. In our spectra, two large bands are present in this region, however, the broadness of the bands does not allow a clear distinction of these peaks (**Table 18**).

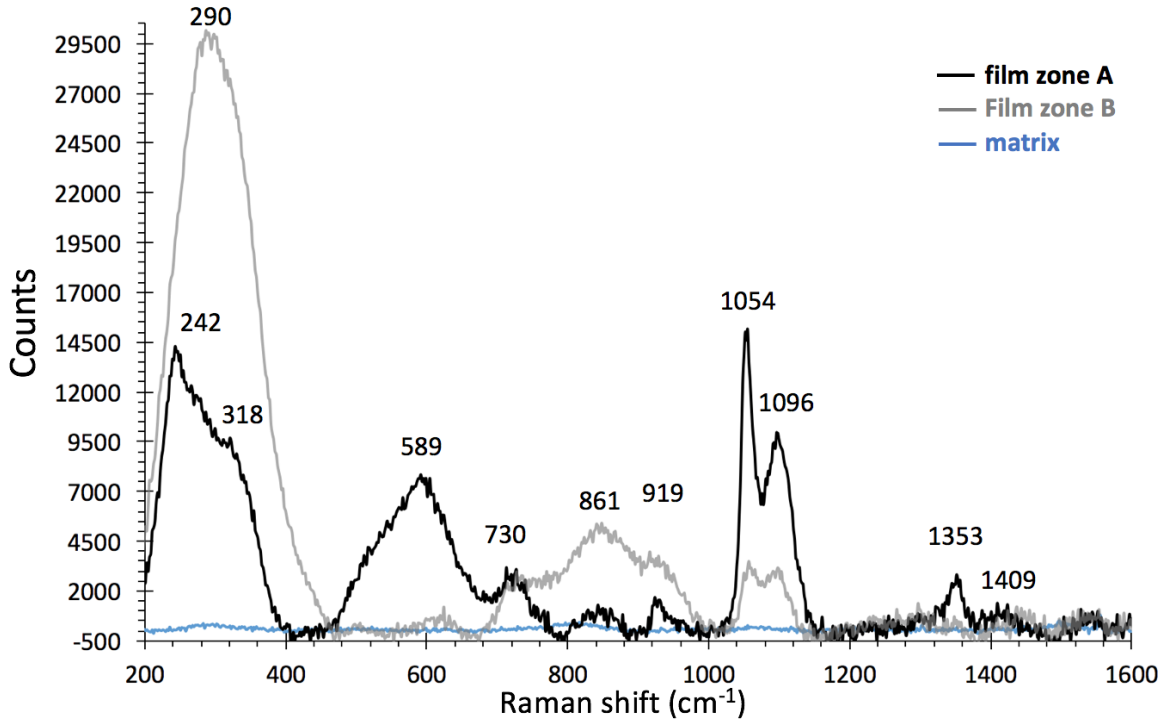

Figure 51 : Raman spectra of two different spots of the film (black and grey) and the matrix (blue).

Table 17 : Raman vibrational modes for free CO_3^{2-} and in LDH

	Free CO_3^{2-} (cm^{-1})	*Hydrotalcite (cm^{-1})*	*This work*
	Ross [179]	Kloprogge [176]	
CO_3^{2-}:			
ν_1	1063	1053	1054
ν_2	-	-	-
ν_3	1415	1372	1409-1353
ν_4	680	725	680-730

Table 18 : Raman vibrational modes for Li reported in the literature and our study

Li-O stretching (cm^{-1})	*Li translational mode (cm^{-1})*	*This work (cm^{-1})*
Smirnov et al. [175]	Parker et al. [178]	
784-954	385 - 412 -540	(589)
		800-980 (861 and 919)

3.4. Complementary analysis of the corrosion product by Infrared spectroscopy

Infrared spectroscopy is used as a complementary technique to the Raman spectroscopy. The assignments of IR bands for Al-Li hydrotalcite have been reported by various researchers. The data collected from the literature and dealing with vibrational modes specific to free carbonates or incorporated into hydrotalcites are gathered in **Table 19.** In addition, the IR vibrational modes for Li-Al-CO_3 series are reported in **Table 20** with our data for comparison. For example, Dutta and Puri reported several bands at frequencies inferior to 600 cm^{-1} [180]. Recently, Gupta et al. reported the assignment of Al-Li-CO_3 through FTIR spectra and assigned the Li(Al)-O and the O-Li(Al)-O at the low frequencies (533-734 cm^{-1}), and three vibrational modes were attributed to the anion fingerprint (ν_1 1004 cm^{-1}, ν_2 860 cm^{-1} and ν_3 1363 cm^{-1}) [181]. Unfortunately, in the case of our study, it was not possible to reach wavenumbers lower than 620 cm^{-1} because of the ZnSe window equipping the apparatus. Thus, infrared spectra have been collected in the 600-1800 cm^{-1} region (**Fig. 52**). Nevertheless, numerous bands are observed in the wavenumber range scanned. For example, one is recorded at 752 cm^{-1}, and could correspond to one of the O-Li(Al)-O vibrational modes observed by Dutta in the case of hydrotalcite [178]. Moreover, two intense bands are clearly observed at 1390 and 1580 cm^{-1}. White et al [177] ascribed them to carbonate-Aluminum association from their study of sodium aluminum hydroxyl carbonate, as well as the lower intense bands at 843 and 1080 cm^{-1}. These authors mentioned that the zone between 1080-1100 cm^{-1} was an inactive band, typical of a substantial lowering of symmetry due to the association between carbonate and aluminum.

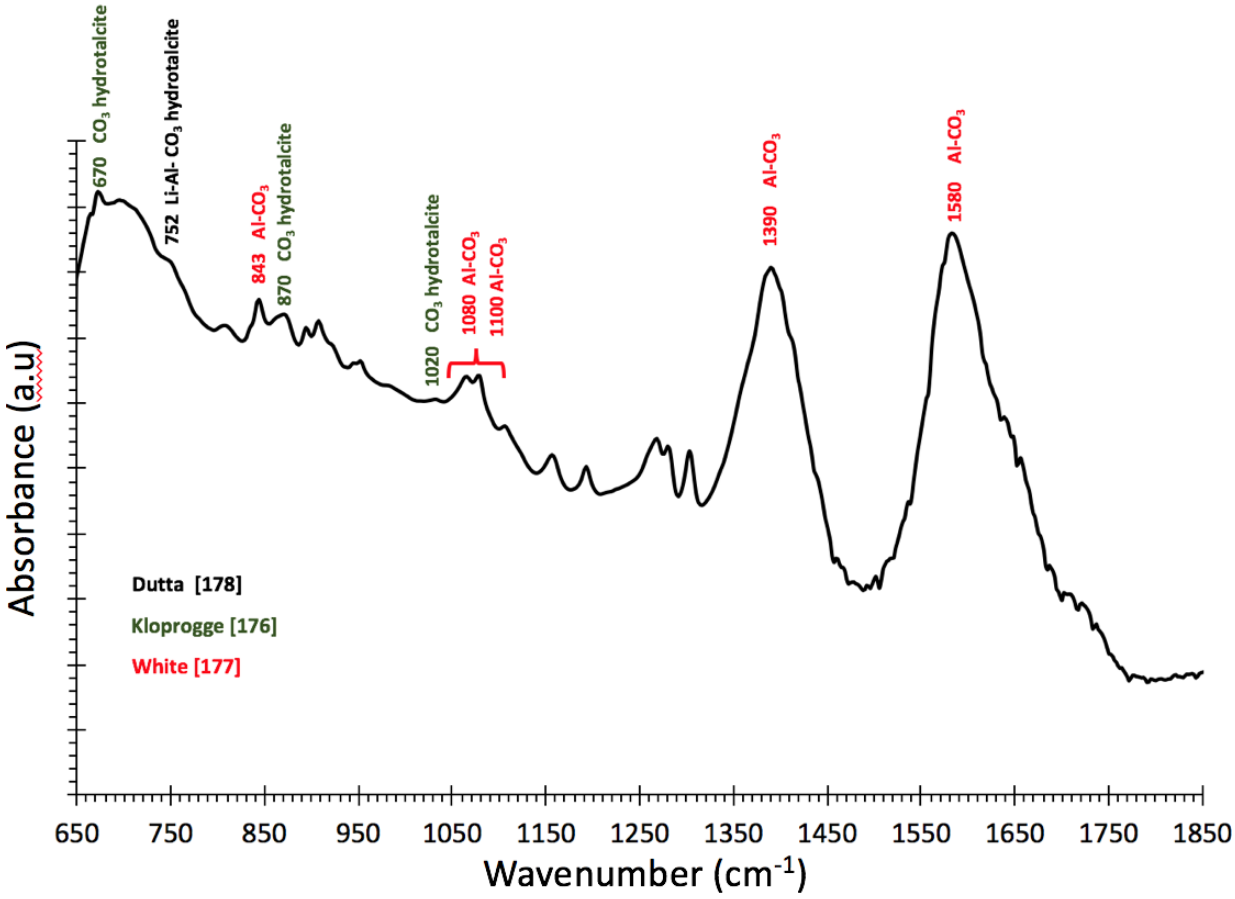

Figure 52 : IR spectra of the corrosion product.

Table 19 : IR Vibrational modes for free CO_3^{2-} and LDH

	Free CO_3^{2-} (cm^{-1})	*Hydrotalcite (cm^{-1})*		*This work*
CO_3^{2-}:	Ross[179]	Gupta [181]	Kloprogge [176]	
ν_1	-	1004	1012	-
ν_2	880	860	870	870
ν_3	1415	1363	1365/1400	1390
ν_4	680	-	667	670

Table 20 : IR Vibrational modes for Li-Al-CO_3 series

	Hydrotalcite (cm^{-1})		*This work*
Li(Al)-O & O-Li(Al)-O	Gupta [181]	Dutta [180]	
	734-533	362-380-402-460-535-555-602-752	752

On the other hand, Kloprogge et al. studied the effect of the nature of the interlayer anion in the infrared spectra of Al/Mg hydrotalcite films [176]. They evidenced the presence of the 4 vibrational modes at ν_1

1012, ν_2 870, a strong and broad ν_3 band at 1365/1400 cm^{-1} and ν_4 at 667 cm^{-1} for the carbonate containing hydrotalcites. These bands, except for the 1012 cm^{-1} (this ν_1 bands was already hardly observable in both studies where the analysis was realized on a pure hydrotalcite powder) could correspond to the following bands in the spectra: ν_2 870 cm^{-1}, ν_3 1390 cm^{-1} and ν_4 673 cm^{-1}. Thus, according to the infrared spectra and the data reported in the literature, the hypothesis of having an Al-Li hydrotalcite film on the surface as a corrosion product is plausible.

4. DISCUSSION

The results provided herein lead to consider the possibility of having a heterogeneous structure comprising two or three films. In chapter IV, it has been revealed that when the surface is exposed to 0.5 M NaCl during anodic polarization, the formation of a film occurred. Unexpectedly, this film forms only if a pretreatment was performed prior polarization.

We may consider that, in chloride containing environment, Al alloys undergo pitting corrosion [1]. Thus, under these specific conditions, the Al and Li ions dissolution leads to the formation of pits. At the bottom of the pit, Al and Li dissolution takes place and aluminum chlorides will form with the presence of chloride ions. This will be followed by Al^{3+} hydrolysis, shifting the pH to more acidic values (pH <3):

$$Al \rightarrow Al^{3+} + 3e^{-} \quad (1)$$

$$Al^{3+} + 3H_2O \rightarrow Al(OH)_3 + 3H^{+} \quad (2)$$

Moreover, in the case of Al alloys, the hydrolysis phenomenon is also applicable for the alloying elements such as Mg, Mn or Fe, and contributes to a local pH decrease by the generation of H^+ ions. When the Al and Li ions concentrations become too high at the pit bottom, they may migrate towards the surface where they are exposed to a less acidic environment (corresponding to the pH of the solution). As a consequence, $Al(OH)_3$ will precipitate at the top of the pit and form amorphous domes. Moreover, the removal of the alloying elements during the pretreatment provides a more favorable environment for the precipitation of amorphous $Al(OH)_3$. This theory is also in good agreement with the solubility diagram of Al oxide and hydroxides established by Pourbaix [2], where the maximum solubility of Al hydroxides decreases drastically from low pH (<3) to near neutral pH (6-7).

Another important parameter that needs to be considered is the proven stabilizing character of Li^+ ions, as, in the case of pure Al, they increase the chances to form a more stable oxide/hydroxide phase [182]. This could explain why this film forms only after pretreatment and its formation is associated to the surface chemistry of the substrate.

Consequently, these amorphous domes could act as a barrier for Li ions yielding to their enrichment on the surface. This supposition was also reinforced by GDOES analysis. From the results presented herein, it was possible to identify the presence of a Li enrichment on the surface of the Al alloy. GDOES analysis was realized on the corroded surface in order to have access to the depth elemental composition of the film. From these results, this lithium film was shown to be incorporated into what could be an Al hydroxide layer and the presence of C, H (mainly on the surface) and O spikes suggested the detachment of some species that could be attributed to carbonates.

Further investigations using the X-ray diffraction analysis were carried out on the Al alloy after different steps in order to isolate the contribution of the film on the diffraction pattern. Interestingly, the results obtained showed the apparition of a crystalline film on the surface after performing the pretreatment. From the data provided in the literature, this film could be assigned to an Al oxide film such as corrindon

(Al_2O_3) on the surface. After the polarization testing, the results revealed that the film formed is mainly composed of Al oxide. Nevertheless, the presence of crystalline phases involving carbonates or Li was not revealed by X-ray diffraction which suggest that some part of the film is either not detected because of its low thickness or/and an amorphous structure. Rangel and Travassos [168] suggested the formation of lithium aluminate, nevertheless, from the present XRD patterns it was not possible to make any significant input on the presence of a Li crystallized structure in the film. Recently, Visser et al. [164] assumed that lithium was intercalated with the aluminum hydroxide gel to produce either small grain size particles or an amorphous structure in the context of the corrosion protection of AA2024 by a Li containing coating. This reinforces our assumptions about the formation of an amorphous hydroxide gel enriched with Li, undetectable by X-ray diffraction, but evidenced by GDOES analysis.

Vibrational spectroscopies (Raman and infrared) were carried out on the surface and clearly show the presence of some carbonate species that could be incorporated in a layered double hydroxide film. These peaks are in good agreement with the assignments reported in the literature for carbonates incorporated in LDH which strongly suggest the presence of what could be a thin layer of LDH. Nonetheless, the mechanism involved in the formation of LDH on the surface of our film still remain unclear. Visser et al. [164] indicated the possibility of an ageing effect of the Al/Li hydroxide promoting the formation of the LDH with time.

In our case, LDH presence was strongly suggested by Raman and IR spectroscopies, although LDH was not found in our XRD patterns. It is important to note that LDH are usually poorly crystalline in nature which makes them hardly detectable by XRD when formed in such conditions.

5. CONCLUSIONS

The chemical nature of an Al- based corrosion product was investigated using several characterization methods. This film was formed under anodic polarization following a pretreatment sequence. The GDOES analysis was used to have access to the elemental depth composition and showed that this film was Al, C, O and H rich with the presence of Li encapsulated in this corrosion product. XRD analysis was conducted to determine the degree of crystallinity and to confirm or exclude the hypothesis of a LDH layer argued in chapter IV. The results obtained indicated the presence of an Al oxide and the possible formation of a lithium aluminate ($AlLiO_2$) although the intensity of the peaks was not significant enough to declare with certainty its formation. The variation of the peak intensities between the different pretreatment steps, suggested the presence of an amorphous layer acting as a mask. Further investigation using vibrational spectroscopies were realized using Raman spectroscopy and Infrared spectroscopy. Carbonate vibrational modes are largely present in the different spectra, as free carbonates or incorporated in hydrotalcite, as well as Li(O)Al signature. These main contributions reinforced our initial assumption concerning LDH formation in our conditions of pretreatment. From these data, the following mechanism was proposed:

- During anodic polarization, Al and Li dissolve, and pits initiate on the surface
- At the bottom of the pit, an important acidification occurs, caused by the Al hydrolysis
- Meanwhile, Al ions and Li ions migrate towards the surface where they are exposed to a less acidic environment, encouraging the precipitation of an amorphous Al hydroxide.
- The formation of domes around the pit will act as a barrier for Li ions and lead to their segregation.

The results observed by the different techniques underlined the heterogeneous character of this film. The mechanism described above corroborates these observations, however, these assumptions need to be verified by additional experiments

As an example, XPS analyses were attempted in parallel, unfortunately in non-adequate conditions for the film product characterization, as only a surface analysis was performed and not a depth profiling. This data should have given accurate information on the environment of Li, the other elements, and probably help in the final determination of LDH (or other).

PRELIMINARY STUDIES & CONCLUSIONS

"***La bêtise consiste à vouloir conclure.***"

"Stupidity lies in wanting to draw conclusions."

Gustave Flaubert.

1. PRELIMINARY STUDIES

1.1. The pretreatment of intermetallic particles: the reactivity of S phase.

This methodology was also extended to the study of single phases, to isolate their behavior during a pretreatment sequence. As an example, the reactivity of the S-phase was monitored using the AESEC set-up and the results are illustrated in **Fig. 53.** When exposed to NaOH, the dissolution profiles of Al, Cu and Mn are close to the detection limit, showing the passive behavior of this precipitate during alkaline etching. This could be explained by the insolubility of Cu and Mg at high pH, protecting the surface by an oxide film, stopping Al from dissolving. The following result clearly shows that this phase is totally unaffected during this first step and suggests a reason why the majority of the particles remain intact on the surface or are released into the electrolyte. Following alkaline etching and water rinsing, the surface is exposed to an acid pickling in HNO_3. When the electrolyte is in contact with the sample, the dissolution of Cu, Mg and Al occurs. Cu signals rises continuously to reach a steady state (106 µg $s^{-1}cm^{-2}$) after 250 s until the water is introduced into the flow cell.

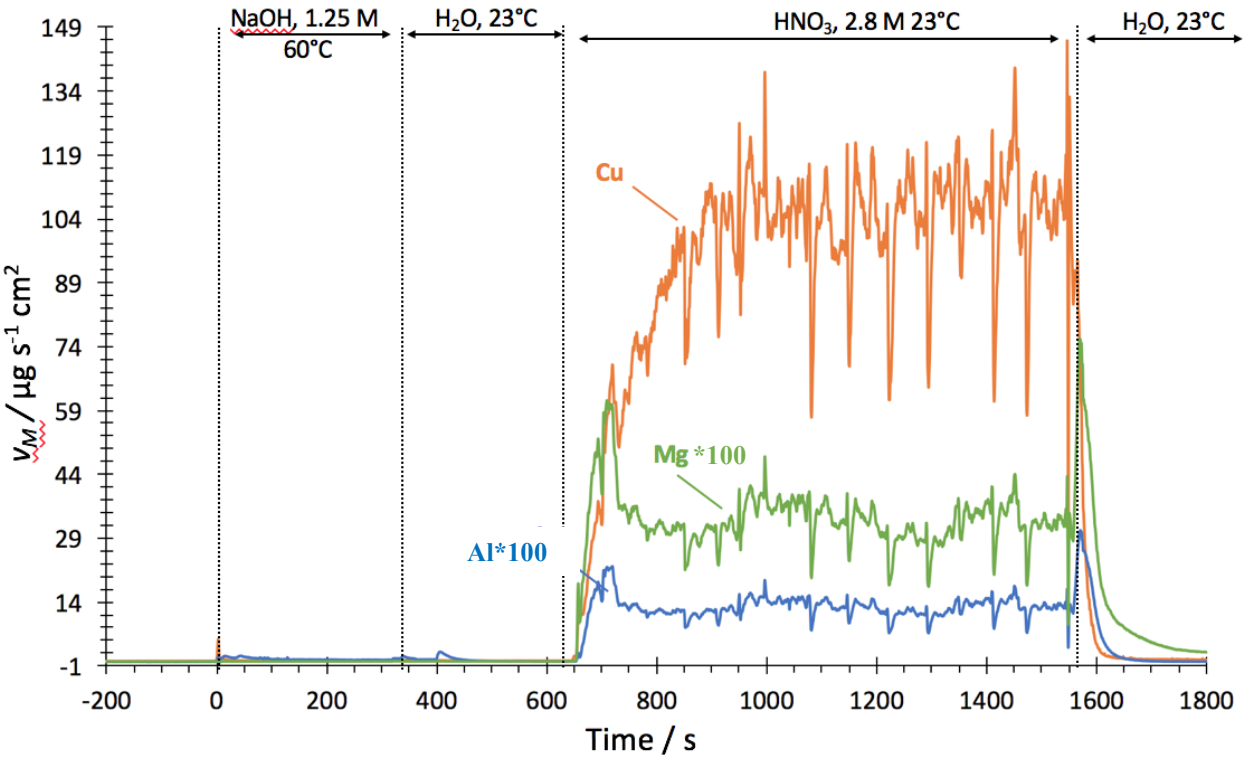

Figure 53 : Dissolution profile of S-phase particle during a pretreatment sequence. The first step corresponds to the exposure to 1.25 M NaOH, followed by water rinse at 23°C and an acid pickling in HNO_3 during 15 min at 23°C. Note the multiplicative factors for Al and Mg demonstrating that Cu is the major element dissolving during this experiment.

SEM observations, illustrated in **Fig. 54**, were performed following the experiment to get additional information on the effect of this treatment. The SEM micrograph, taken in backscattering mode, indicates the presence of Cu nanoparticles on the surface. Interestingly, these nanoparticles were observed during the anodic polarization of AA2024-T3 after pretreatment and implies that this phase is the "reservoir" for Cu nanoparticulates formation.

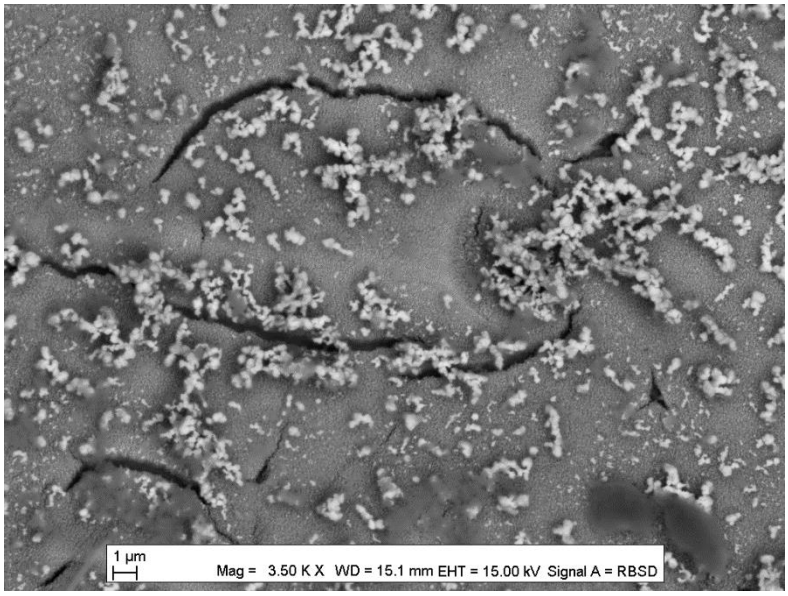

Figure 54 : SEM micrograph in backscattering mode of the S-phase after the pretreatment sequence. The chemical contrast shows the presence of remnant nanoparticulates that could be attributed to Cu.

1.2. The statistical analysis of particle detachment: establishment of relationships between elements, signal intensities and particle nature.

Intermetallic particle behavior was conspicuously one of the main interest of this PhD work, as their removal defines the ambition of every pretreatment. The results presented previously demonstrated that particle removal could be seen as a dissolution or detachment process. One of the specificity of this methodology is the ability to follow simultaneously dissolution reactions and intermetallic removal. Preliminary observations pertaining to particle detachment were presented in chapter III and IV, in which a certain correlation between the elements was qualitatively observed suggesting that particles of a specific phase would lead to a characteristic elemental composition in the ICP-AES analysis, or at least a correlation between the elements. Therefore, to fully exploit this lead, a detailed analysis of the data was conducted through a statistical approach using RStudio™. This software is a programming language for statistical computing and graphics. Two different files were loaded into the RStudio™software: the first one contains a series of data which are representing the intensity value of Cu, Mg, Fe and Mn as a function of time. These data were collected during the exposition of an AA2024-T3 to 1.25 M NaOH at 60°C during 5 min, corresponding to the first step of the pretreatment sequence. To ensure a high peak definition, the data collection time during the experiment was of 10 Hz (10 points

per second). The second file contains the average value of the background of the corresponding elements for this experiment. Before starting the data analysis, it was important to select only the data frame corresponding to the time of the experiment and subtract the backgrounds of their corresponding signals. In the context of this study, the time scale was not relevant as we were only interested in the interactions between the elements. Consequently, to have a first overview of the interactions between each element, we plotted a "scatter view" (**Fig. 55**). Each axis was labelled and represents the intensity of one element, and each element is plotted as a function of another. Moreover, it was important to note that the measurement also shows whether a linear relationship of the intensities between two elements was present or not. For example, the Mn and Fe graphs highlighted a possible linear relationship between both elements. The corresponding correlation factor diagram was also shown in **Fig. 55** and from this, it is possible to make two important observations: the Cu signal has a positive correlation value with the three other elements. It is commonly accepted that a correlation factor value higher than 0.5 is significant. On the other hand, this figure confirms the strong relationship between Fe and Mn signals (0.89). Hence, from this, it is possible to assume that the Mg, Mn and Fe detachment process mainly hinges on copper's behavior. This idea is also consistent with the particle stochiometries reported in the literature, and consequently, it was assumed that two different families of peak relationship that we call "population" were found: Cu-Mg peaks and the Cu-Mn-Fe peaks. It is important to remind that Al was not measurable because of its high solubility in alkaline conditions.

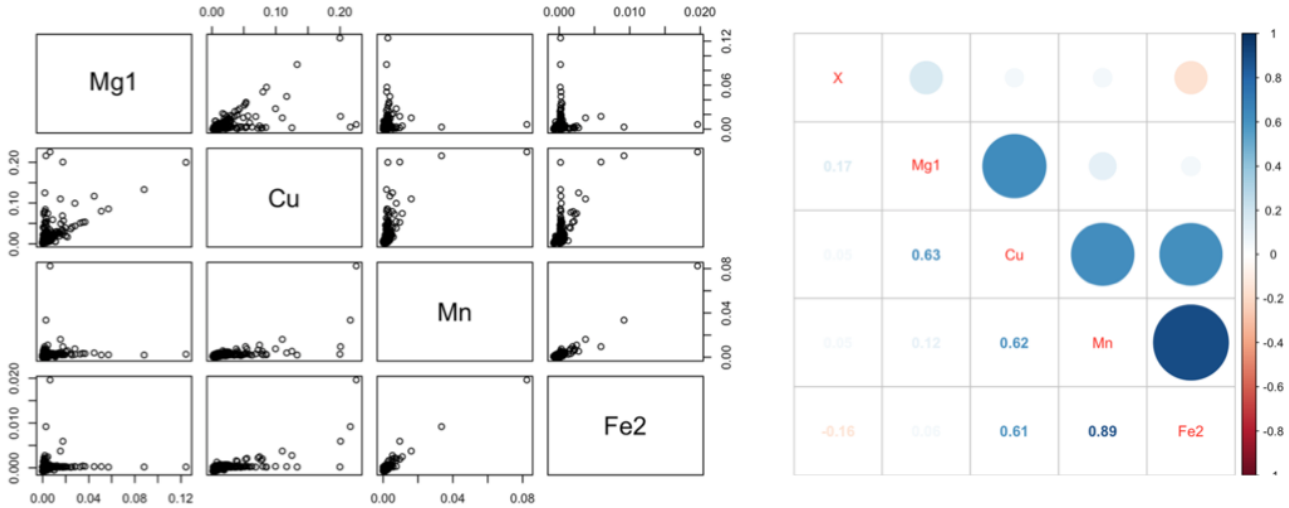

Figure 55: Correlation factor diagram representing the relationship between the elements.

The second step was dedicated to select the data points corresponding to peaks and only select them. Consequently, for a signal X_t where t is the time, we defined a signal data point as a peak, X_p, when its value was higher than the sum of the average signal and two times the standard deviation:

$$X_p \in \{s \in X_t \,|\, s \geq \mu_{X_t} + 2\sigma_{X_t}\}$$

where μ_X is the average value of the Cu signal, σ_{X_t} is the standard deviation of the X_t signal. Firstly, these values are selected from the file and each value for all the elements are flagged "yes" when a peak

is found and “no” when a peak was absent. The resulting chart highlighted also a possible relation between the intensity of the peak and the nature of the particle as the highest intensities of Cu seem to be mainly correlated with Mn or Fe. This hypothesis will be also verified and discussed hereafter. Secondly, from the data set we determined the proportion of Cu peaks relative to all peaks and found that 72 % of the peaks are involve a Cu detachment process whether the latter detaches alone or involves other elements. (**Fig. 55)**. These results could be easily explained by the alloy microstructure composition of the AA2024-T3 as the presence of Cu in the intermetallic composition and especially in the large constituent particle and in the precipitates has been demonstrated. These peaks most probably correspond to the S phase (Al_2CuMg), theta phase (Al_2Cu), the Al_7Cu_2Fe or even the Al-Cu-Me-Fe intermetallic particles. On the other hand, the remaining 28 % peaks, which are not involving Cu, correspond to:

- Single peak of Fe (5 %)
- Mg and Mn peaks (5%)
- Single Mg peaks (90%)

This result clearly demonstrates Mg is the major element detaching without Cu. This phenomenon could be explained by the detachment of an Mg_2Si intermetallic particle. However, it is important to note that if there is a link between the intensity of Cu peak and the nature of the particle, then, the particles with the lowest Cu intensity might not be taken into account in our calculations. Indeed, a peak is defined as the sum of the signal and two times the standard deviation. Interestingly, the average value of the intensity of the Cu peaks involved with Mg is 1.5 lower than the intensity of Cu peaks involved with Mn-Fe. If we assume that the intensity of the Cu in the Mg-Cu particles is lower than the Cu peaks involved in the Mn-Fe particles, thus it could be interesting to redefine the baseline by removing the peaks involving Cu-Mn and Fe. This will thus decrease the detection limit defined earlier, and take into account lower intensity Cu peaks. Nonetheless, it is essential to verify that this assumption is true by realizing a statistical test.

The Mann-Whitney-Wilcoxon test is used to demonstrate the effective relationship between the intensity of Cu peak and the nature of the particle analyzed. This non-parametric statistical test allows to compare two different data set with the null hypothesis, H_0, that two samples come from the same population or the alternative hypothesis where one population tends to have higher values.

In this case, if the null hypothesis was verified, this meant the two Cu-Mg and the Cu-Mn-Fe dataset came from the same population, hence they have the same order of magnitude. However, if this hypothesis was not verified, it will be possible to assume that the datasets were independent, and hence suppose there was a relationship between particle type and Cu intensity. The null hypothesis H_0 was rejected, thus it was possible to assume that Cu intensity from Mg particles and Cu from Mn-Fe particles do not have the same order of magnitude. Consequently, the detection limit was redefined after removing from the calculations the Cu values involving Mn and Fe and the proportion of Cu peaks was

recalculated. The results showed that the proportion of Cu peaks increased from 72 % to 85%, and the remaining 15 % showed the same distribution as described earlier.

Fig. 56 represents the distribution of the Cu peaks as a result of the statistical approach and calculations described previously. Each node corresponded to an element with its corresponding color and the thickness of its link represented the co-occurrence between the element and another. Concerning Cu behavior, the results showed that 44.3 % of the total peaks were involved with Mg, 18.6 % with Fe and 17.1 % were involved with Mn, the remaining corresponded to single Cu detachment. On the other hand, Mg seemed to have only a strong link with Cu as 73.8 % of the peaks were occurring with Cu detachment as the percentage of Mg detaching with Mn or Fe were respectively of 9.5 % and 14.3%. Fe and Mn, seemed to follow the same trend as 92.3% of the Mn and 92.9 % of the Fe were involved with Cu. Moreover, the figure shows the strong co-occurrence between Mn and Fe and this could correspond to the Al-Cu-Mn-Fe particle detachment. Further calculations were realized to determine if Mn-Fe detachment was related to Cu and the results showed that Mn-Fe peak always implicated a Cu peak.

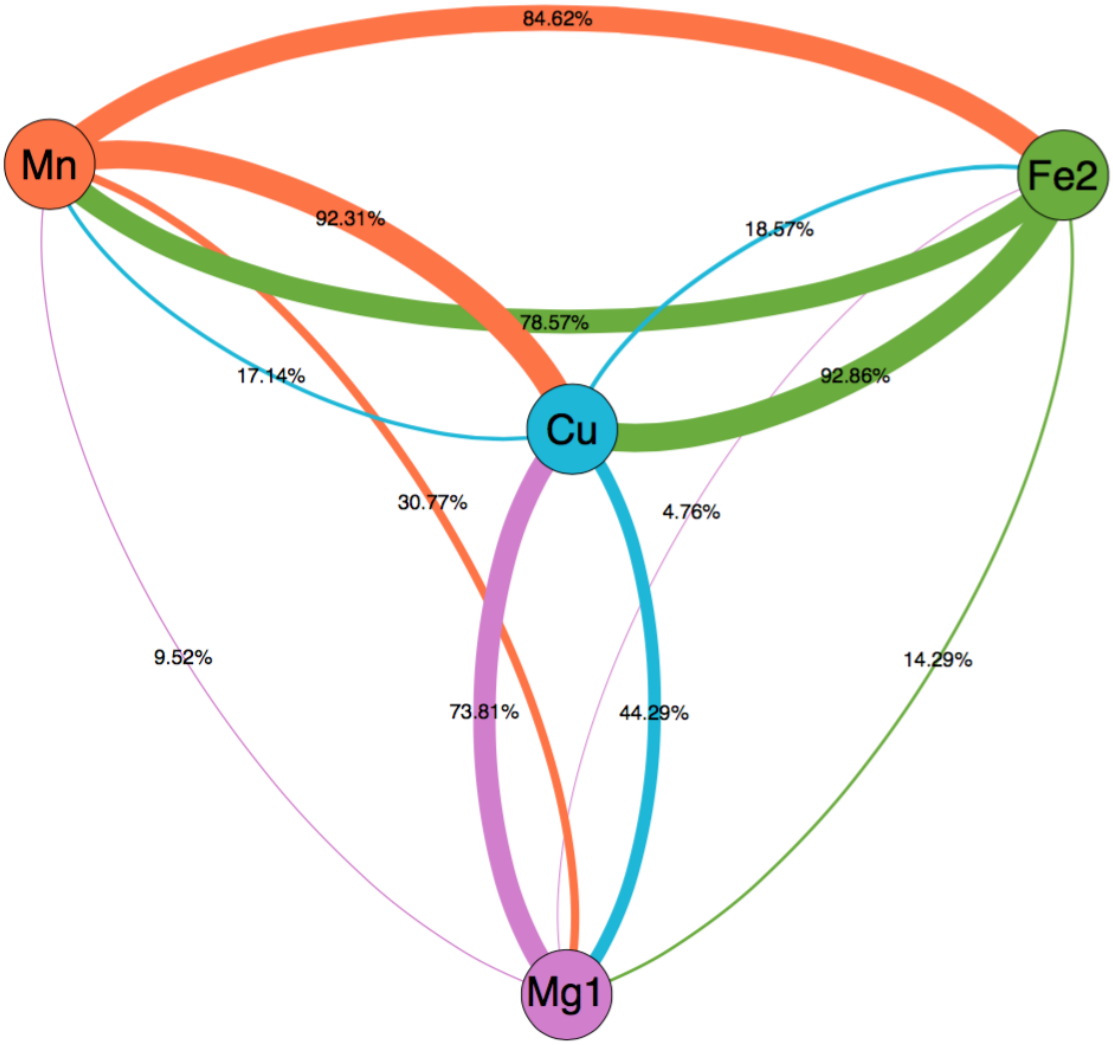

Figure 56: Distribution of Cu peaks as a result of the statistical calculations. Each node corresponds to an element with its corresponding color and the thickness of its link represents the co-occurrence between the element and another.

This novel approach emphasizes the possibilities offered by the AESEC techniques for the detection of particles released during the reaction of a material with an aggressive electrolyte. This type of mechanism has been proposed for many alloys and yet is not readily detectable by other methods. The statistical approach developed here reinforced our preliminary assumptions in chapter III by the accurate evaluation of the co-occurrence between one element and another in terms of particle detachment. This work could be extended to determine the effect of different operating parameters on the detachment/enrichment of alloying elements and eventually could be viewed as a predictive tool for surface treatment development. As a matter of fact, an ultimate goal of every Al pretreatment is to remove these particles.

2. CONCLUSIONS

2.1. General conclusions

The main objective of this work was to develop a novel methodology, able to give an accurate measurement of the reactivity of complex Al-based alloys during a sophisticated surface treatment process. Although the AESEC methodology has been previously used for single step surface treatments, these developments herein have permitted the extension of the technique to multiple step treatments under much more severe conditions. This is an important step closer to working under industrial conditions and should prove valuable for the development of new treatment formulations.

The initial set-up, the atomic emission spectroelectrochemistry was modified to adapt it to our "extreme" conditions: the corrosion reactions occur within a relatively short time with very large rates; they often involve massive precipitation, and sometimes particles release. Numerous difficulties were encountered during the first part of this work such as high corrosion rates and detector saturation, introduction system blockage induced by particle detachment and precipitation yielding to several modifications of the original set up.

The second part of this work (chapter III) was devoted to the implementation and validation of our methodology. This was achieved through the study of AA2024-T3 during a surface treatment sequence. This alloy AA2024-T3 Al alloy was chosen for the important amount of data available in the literature, mainly collected by *ex situ* methods. The AESEC results pertaining to the effect of the pretreatment of AA2024-T3 provided new insights on its reactivity. It was shown that during the alkaline etching, Al undergoes an important dissolution, accompanied with a very low amount of Cu, Mg, Mn and Fe particle detachment. Moreover, this first part demonstrated that the majority of the alloying elements remain on the surface. When the surface was exposed to HNO_3, the alloy instantly reacted and sharp and intense peaks of Cu, Mg, Al, Fe, and Mn were observed. By determining the residence time distribution of our flow cell, we were able to distinguish the instantaneous dissolution of what we attributed to hydroxides and the slower dissolution rate of what we ascribed to intermetallic particles. Moreover, by integrating the dissolution profiles of Al and Cu, and from the bulk composition, we were able to follow the Al mass loss and Cu dissolution/enrichment as a function of the pretreatment step. The calculations indicated that an enrichment of Cu resulted from the surface treatment. This was correlated with *ex situ* analysis such as SEM, to have access to the surface topography along with the chemical distribution after pretreatment. Furthermore, the etch rate was determined by profilometry which is a conventional technique and AESEC to correlate our results. The comparison highlighted the power of AESEC in terms of element by element dissolution kinetics as a function of the step which is not possible to determine with profilometry. Further investigations were conducted by performing potentiodynamic polarization curves on the samples before and after pretreatment. The conventional polarization curves highlighted the beneficial effect of the pretreatment, as the cathodic current decreased by approximately

one order of magnitude. The corresponding AESEC polarization curves, however, indicated the presence of Cu nanoparticles, which were only detectable during anodic polarization when the matrix was dissolving. Thus, these particles did not contribute to the electrochemical behavior of the alloy, suggesting that they were not in electrical contact with the surface. This study provided a complete survey of the reactivity of a complex alloy in industrial conditions. It demonstrated the potential of this technique to redefine the qualification process of surface treatments.

The third part of this work (chapter IV) focused on the reactivity of a new Al-Li alloy, AA2050. This alloy is already in service, nevertheless, very little is known about its reactivity, particularly the behavior of Li, during a surface treatment. Consequently, an identical pretreatment procedure was performed on this alloy and the dissolution rate of its elements was monitored using the optimized AESEC set-up. The results provided by chapter IV clearly indicated that this alloy reacted very differently from the previous AA2024-T3. Indeed, when exposed to NaOH, Al and Li dissolve (it is worth noting that Al dissolution rate was significantly lower than what was measured for AA2024), with a preferential dissolution of Li (according to the bulk composition). When exposed to HNO_3, the surface immediately reacts and intense peaks of Cu, Mg, Mn and less intense of Al, Fe, and Li were measured. Again, the alloy clearly behaves differently than the AA2024-T3, as the reaction is completed after 30 s compared to 200 s for AA2024-T3. The difference in the time scale of the experiment was explained by the microstructure of the alloy, particularly by the smaller size of the intermetallic particles. The SEM observations showed that the AA2050-T3 surface exhibited less particles on the surface: thus, the higher the number of constituent particles we have on the surface, the longer their dissolution will last. The last part of this chapter was devoted to the electrochemical characterization of the surface prior and after pretreatment. The results demonstrated again the beneficial effect of the pretreatment, as the cathodic and anodic current decreased significantly by one order of magnitude. Unexpectedly, the AESEC evidenced the formation of Al-based oxide film during the anodic polarization of the pretreated AA2050-T3 in 0.5 M NaCl. This film formation occurred only on this alloy AA2050-T3 and if a pretreatment was performed prior the corrosion test. Additional GDOES experiments were conducted to analyze the nature of the film. The erosion profiles strongly suggested the presence of an Al oxide based film enriched with Li. In order to isolate the effect of Li, an AA2024-T3 was anodically polarized in 0.5 NaCl with 1 ppm of Li. Surprisingly, the alloy exhibited the same behavior as the pretreated AA2050-T3, demonstrating significant role of Li on the film formation. The preliminary assumption for the film composition was the formation of an Al/Li hydrotalcite product, as the formation of this corrosion film has been mentioned in the literature. However, our specific conditions were not *a priori* favorable for this film precipitation, making the circumstances of its formation unclear.

The last chapter (chapter V) dealt with the characterization of this Al-based oxide film, in order to be able to enlighten the mechanism behind its formation. To achieve this goal, several analytical techniques were used, such as GDOES to have access to the elemental composition, X-ray diffraction to determine the degree of crystallinity, and vibrational spectroscopies to access to the composition of amorphous

products. The GDOES demonstrated that the film was Al, C, O and H rich, and suggested a certain enrichment of Li, which might be encapsulated into the Al rich layer. XRD, was able to give insights on the crystallinity of the corrosion product, and indicated the possible formation of a lithium aluminate phase, as well as the presence of an amorphous corrosion product acting as a mask. Complementary experiments using Raman and Infrared spectroscopies allowed the identification of carbonate species that could be incorporated into a layered double hydroxide (LDH). The presence of at least two different film natures in the corrosion product were suggested from these analyses: an amorphous Al hydroxide, $Al(OH)_3$, as well as the possible Al/Li, in the form of an Al/Li layered double hydroxide.

This work emphasizes how complex is the reactivity of these alloys and demonstrates that the AESEC could provide significant information; for example, when a better targeting of specific intermetallic particles is needed.

2.2. Perspectives

As a perspective of this work, further investigations could be conducted to clearly identify the nature of the corrosion product evidenced in this work. Additional XPS analysis, such as depth profiling, could "lift the veil" on the composition of this film. In addition, GDOES analysis on the pretreated and polarized AA2024-T3 in NaCl and Li solution could be useful to determine if Li is incorporated in the Al oxide film.

These preliminary studies on pure intermetallic phase and particle detachment analysis were shown to be very powerful, especially as these particles react very differently from the matrix. Those tools are able to collect a large amount of data, and could be used as a basis for analysis of trends or to predict the particle reactivity as a function of the surface treatment.

Beyond this PhD work, the perspectives of this methodology could be extended to a multitude of alloys and applications. As an example, the reactivity of complex Mg alloys attracts increasingly the interest for automotive or biomedical applications and the prospects of using these light alloys remains a challenging work.

REFERENCES

[1] C. Vargel, Corrosion of aluminium, Elsevier Ltd, 2004.

[2] M.J.N. Pourbaix, Atlas D'équilibres Électrochimiques, 1963.

[3] E.A. Starke, J.T. Staley, Application of modern aluminum alloys to aircraft, Prog. Aerosp. Sci. 32 (1996) 131–172. doi:10.1016/0376-0421(95)00004-6.

[4] J.G. Kaufman, E.L. Rooy, Aluminum Alloy Castings: Properties , Processes, and Applications, 2004.

[5] J.E. Hatch, Aluminum Properties and Physical Metallurgy, Ohio, 1984.

[6] I.J. Polmear, Light Alloys : Metallurgy of the light metals, Third, 1995.

[7] a. Boag, a. E. Hughes, N.C. Wilson, a. Torpy, C.M. MacRae, a. M. Glenn, et al., How complex is the microstructure of AA2024-T3?, Corros. Sci. 51 (2009) 1565–1568. doi:10.1016/j.corsci.2009.05.001.

[8] V. Guillaumin, G. Mankowski, Localized corrosion of 2024 T351 aluminium alloy in chloride media, Corros. Sci. 41 (1999) 421–438.

[9] C. Liao, J.M. Olive, M. Gao, R.P. Wei, In-Situ Monitoring of Pitting Corrosion in Aluminum Alloy 2024, Corros. Sci. 54 (1998) 451–458.

[10] C. Liao, R.P. Wei, Galvanic coupling of model alloys to aluminum — a foundation for understanding particle-induced pitting in aluminum alloys, Electrochim. Acta. 45 (1999) 881–888.

[11] G.M. Scamans, N. Birbilis, R.G. Buchheit, Corrosion of Aluminum and its Alloys, in: Tony Richardson (Ed.), Shreir's Corros., 2010: pp. 1975–2008.

[12] A. Afseth, J.H. Nordlien, G.M. Scamans, K. Nisancioglu, Effect of heat treatment on filiform corrosion of aluminium alloy AA3005, Corros. Sci. 43 (2001) 2093–2109.

[13] M.U. Fishkis, J.C. Lin, Formation and evolution of a subsurface layer in a metalworking process, Wear 206. 206 (1997) 156–170.

[14] T.H. Muster, A.E. Hughes, G.E. Thompson, Copper Distributions in Aluminium Alloys, Nova Science Publishers Inc., New York, 2009.

[15] H. Leth-Olsen, J.H. Nordlien, K. Nisancioglu, Filiform corrosion of aluminium sheet. III. Microstructure of reactive surfaces, Corros. Sci. 40 (1998) 2051–2063. doi:10.1016/S0010-938X(98)00094-8.

[16] O. Lunder, K. Nisancioglu, The effect of alkaline-etch pretreatment on the pitting corrosion of wrought aluminum, Corrosion. 44 (1988) 414–422.

[17] M. Textor, M. Amstutz, Surface analysis of thin films and interfaces in commercial aluminium products, Anal. Chim. Acta. 2670 (1994) 15–26.

[18] N. Birbilis, R.G. Buchheit, Electrochemical Characteristics of Intermetallic Phases in Aluminum Alloys: An Experimental Survey and Discussion, J. Electrochem. Soc. 152 (2005) B140–B151.

doi:10.1149/1.1869984.

[19] R.G. Buchheit, A Compilation of Corrosion Potentials Reported for Intermetallic Phases in Aluminum Alloys, J. Electrochem. Soc. 142 (1995) 3994–3996. doi:10.1149/1.2048447.

[20] K.S. Ghosh, S. Mukhopadhyay, B. Konar, B. Mishra, Study of aging and electrochemical behaviour of Al-Li-Cu-Mg alloys, Mater. Corros. (2012) n/a-n/a. doi:10.1002/maco.201106409.

[21] J.R. Scully, T.O. Knight, R.G. Buchheit, D.E. Peebles, Electrochemical characteristics of the Al2Cu, Al3Ta and Al3Zr intermetallic phases and their relevancy to the localized corrosion of Al alloys, Corros. Sci. 35 (1993) 185–195.

[22] F. Eckermann, T. Suter, P.J. Uggowitzer, A. Afseth, P. Schmutz, Electrochimica Acta The influence of MgSi particle reactivity and dissolution processes on corrosion in Al – Mg – Si alloys, Electrochim. Acta. 54 (2008) 844–855. doi:10.1016/j.electacta.2008.05.078.

[23] P. Schmutz, G.S. Frankel, Characterization of AA2024-T3 by Scanning Kelvin Probe Force Microscopy, J. Electrochem. Soc. 145 (1998) 2285–2295.

[24] P. Leblanc, G.S. Frankel, A Study of Corrosion and Pitting Initiation of AA2024-T3 Using Atomic Force Microscopy, J. Electrochem. Soc. 149 (2002) 239–247. doi:10.1149/1.1471546.

[25] J. Idrac, G. Mankowski, G. Thompson, P. Skeldon, Y. Kihn, C. Blanc, Galvanic corrosion of aluminium–copper model alloys, Electrochim. Acta. 52 (2007) 7626–7633. doi:10.1016/j.electacta.2007.05.056.

[26] C. Blanc, N. Pébère, B. Tribollet, V. Vivier, Galvanic coupling between copper and aluminium in a thin-layer cell, Corros. Sci. 52 (2010) 991–995. doi:10.1016/j.corsci.2009.11.023.

[27] J.-B. Jorcin, C. Blanc, N. Pébère, B. Tribollet, V. Vivier, Galvanic Coupling Between Pure Copper and Pure Aluminum, J. Electrochem. Soc. 155 (2008) C46. doi:10.1149/1.2803506.

[28] L. Lacroix, C. Blanc, N. Pébère, G.E. Thompson, B. Tribollet, V. Vivier, Simulating the galvanic coupling between S-Al2CuMg phase particles and the matrix of 2024 aerospace aluminium alloy, Corros. Sci. 64 (2012) 213–221. doi:10.1016/j.corsci.2012.07.020.

[29] Z. Szklarska-Smialowska, Pitting corrosion of aluminum, Corros. Sci. 41 (1999) 1743–1767.

[30] G.S. Frankel, Pitting Corrosion, in: S.D.C. and B.S. Covino (Ed.), Met. Handb., ASM Intern, 2003: pp. 1–6.

[31] E. Mccafferty, The electrode kinetics of pit initiation on aluminum, Corros. Sci. 37 (1995) 481–492.

[32] N. Murer, R.G. Buchheit, Stochastic modeling of pitting corrosion in aluminum alloys, Corros. Sci. 69 (2013) 139–148. doi:10.1016/j.corsci.2012.11.034.

[33] N.D. Greene, M.G. Fontana, A Critical Analysis of Pitting Corrosion., Corrosion. 15 (1959) pp.25-31. doi:10.5006/0010-9312-15.1.41.

[34] R.T. Foley, Localized Corrosion of Aluminum Alloys—A Review, Corrosion. 42 (1986) 277–288. doi:10.5006/1.3584905.

[35] M.G. Fontana, N.D. Greene, Corrosion engineering, 1967.

[36] N. Birbilis, R.G. Buchheit, Investigation and Discussion of Characteristics for Intermetallic Phases Common to Aluminum Alloys as a Function of Solution pH, J. Electrochem. Soc. 155 (2008) C117–C126. doi:10.1149/1.2829897.

[37] T. Suter, R.C. Alkire, Microelectrochemical Studies of Pit Initiation at Single Inclusions in Al 2024-T3, J. Electrochem. Soc. 148 (2001) 36–42.

[38] O. Schneider, G.O. Ilevbare, J.R. Scully, R.G. Kelly, In Situ Confocal Laser Scanning Microscopy of AA 2024-T3 Corrosion Metrology, J. Electrochem. Soc. 151 (2004) B453–B464. doi:10.1149/1.1764781.

[39] R. Ambat, A.J. Davenport, G.M. Scamans, A. Afseth, Effect of iron-containing intermetallic particles on the corrosion behaviour of aluminium, Corro. 48 (2006) 3455–3471. doi:10.1016/j.corsci.2006.01.005.

[40] L. Speckert, G.T. Burstein, Combined anodic / cathodic transient currents within nucleating pits on Al – Fe alloy surfaces, Corros. Sci. 53 (2011) 534–539. doi:10.1016/j.corsci.2010.11.008.

[41] O. Seri, The Effect of NaCl Concentration On The Corrosion Behavior of Aluminum Containing Iron, Corros. Sci. 36 (1994) 1789–1803.

[42] G.S. Chen, M. Gao, R.P. Wei, Microconstituent-Induced Pitting Corrosion in Aluminum Alloy 2024-T3, Corros. Sci. 52 (1996) 8–15.

[43] O. Schneider, G.O. Ilevbare, J.R. Scully, R.G. Kelly, *In Situ Confocal Laser Scanning Microscopy of AA 2024-T3 Corrosion Metrology II . Trench Formation around Particles, J. Electrochem. Soc. 151 (2004) B465–B472. doi:10.1149/1.1764781.

[44] W. Zhang, G.S. Frankel, Transitions between pitting and intergranular corrosion in AA2024, Electrochim. Acta. 48 (2003) 1193–1210. doi:10.1016/S0013-4686(02)00828-9.

[45] J.R. Galvele, S.M.D.E.D.E. Micheli, B. Aires, Mechanism of intergranular corrosion of F Al-Cu alloys *, 10 (1970) 7–14.

[46] R.G. Buchheit, Local Dissolution Phenomena Associated with S Phase (Al[sub 2]CuMg) Particles in Aluminum Alloy 2024-T3, J. Electrochem. Soc. 144 (1997) 2621–2628.

[47] R. Buchheit, R. Boger, Cu redistribution and surface enrichment due to dissolution of Al-Cu alloys, 2001.

[48] R.G. Buchheit, R.P. Grant, P.F. Hlava, B. Mckenzie, G.L. Zender, Local Dissolution Phenomena Associated With S Phase (Al 2 CuMg) Particles in Aluminum Alloy 2024-T3, Albuquerque, New Mexico, n.d.

[49] N. Dimitrov, Copper Redistribution during Corrosion of Aluminum Alloys, J. Electrochem. Soc. 146 (1999) 98–102. doi:10.1149/1.1391570.

[50] L. Lacroix, L. Ressier, C. Blanc, G. Mankowski, Combination of AFM, SKPFM, and SIMS to Study the Corrosion Behavior of S-phase particles in AA2024-T351, J. Electrochem. Soc. 155 (2008) C131. doi:10.1149/1.2833315.

[51] M.B. Vukmirovic, N. Dimitrov, K. Sieradzki, J.E. Soc, P. B-b, M.B. Vukmirovic, et al.,

Dealloying and Corrosion of Al Alloy 2024-T3, J. Electrochem. Soc. 149 (2002) B428–B439. doi:10.1149/1.1498258.

[52] D. Zhu, W.J. van Ooij, Corrosion protection of AA 2024-T3 by bis-[3-(triethoxysilyl)propyl]tetrasulfide in neutral sodium chloride solution. Part 1: corrosion of AA 2024-T3, Corros. Sci. 45 (2003) 2163–2175. doi:10.1016/S0010-938X(03)00060-X.

[53] S. Lebouil, J. Tardelli, E. Rocca, P. Volovitch, K. Ogle, Dealloying of Al 2 Cu, Al 7 Cu 2 Fe, and Al 2 CuMg intermetallic phases to form nanoparticulate copper films, Mater. Corros. (2014) n/a-n/a. doi:10.1002/maco.201307550.

[54] K. Nisancioglu, Electrochemical Behavior of Aluminum-Base Intermetallics Containing Iron, J. Electrochem. Soc. 137 (1990) 69–77.

[55] G.O. Ilevbare, J.R. Scully, J. Yuan, R.G. Kelly, Inhibition of Pitting Corrosion on Aluminum Alloy 2024-T3: Effect of Soluble Chromate Additions vs Chromate Conversion Coating, Corrosion. 56 (2000) 227–242. doi:10.5006/1.3287648.

[56] N. Birbilis, M.K. Cavanaugh, R.G. Buchheit, Electrochemical behavior and localized corrosion associated with Al7Cu2Fe particles in aluminum alloy 7075-T651, Corros. Sci. 48 (2006) 4202–4215.

[57] J.W. Martin, Aluminum-Lithium Alloys, in: Annu. Rev. Mater. Sci., 1988: pp. 101–119.

[58] C. Meriç, Physical and mechanical properties of cast under vacuum aluminum alloy 2024 containing lithium additions, Mater. Res. Bull. 35 (2000) 1479–1494. doi:10.1016/S0025-5408(00)00348-2.

[59] R.J. Rioja, J. Liu, The evolution of Al-Li base products for aerospace and space applications, Metall. Mater. Trans. A Phys. Metall. Mater. Sci. 43 (2012) 3325–3337.

[60] J.E. Kertz, P.I. Gouma, R.G. Buchheit, Localized Corrosion Susceptibility of Al-Li-Cu-Mg-Zn Alloy AF / C458 Due to Interrupted Quenching from Solutionizing Temperatures, Metall. Mater. Trans. A Phys. Metall. Mater. Sci. 32 (2001) 2561–2573.

[61] R.J. Rioja, A. Cho, P.E. Bretz, Aluminum-Lithium Alloys Having Improved Corrosion Resistance Containing Mg and Zn, 1990.

[62] K. Kobayashi, S. Ohsaki, A. Kamio, T. Sayo, Y. Tsuji, Corrosion resistance of Al-Li alloys containing small amount Zn, J. Japan Inst. Mater. 42 (1992) 211–216.

[63] D.L. Gilmore, E.A. Starke, Trace Element Effects on Precipitation Processes and Mechanical Properties in an Al-Cu-Li Alloy, Metall. Mater. Trans. A Phys. Metall. Mater. Sci. 28 (1997) 1399–1415.

[64] F. Viejo, a. E. Coy, F.J. Garcia-Garcia, Z. Liu, P. Skeldon, G.E. Thompson, Relationship between microstructure and corrosion performance of AA2050-T8 aluminium alloy after excimer laser surface melting, Corros. Sci. 52 (2010) 2179–2187. doi:10.1016/j.corsci.2010.03.003.

[65] R.E. Crooks, E.A. Starke, The Microstructure and Tensile Properties of a Splat-Quenched AI-

Cu-Li-Mg-Zr Alloy, Metall. Mater. Trans. A Phys. Metall. Mater. Sci. 15 (1984) 1367–1377.

[66] P. Niskanen, T.H. Sanders, J.G. Rinker, M. Marek, Corrosion of Aluminum Alloys Containing Lithium*, Corros. Sci. 22 (1982) 283–304.

[67] W. Miller, J. White, D. Lloyd, The Physical Metallurgy of Aluminium Alloys 8090 and 8091, J. Phys. Colloq. 48 (1987) C3-139-C3149.

[68] E. Di Russo, Microstructures, tensile properties, fatigue crack growth behaviour of the zirconium modified 2024 alloys processed by liquid dynamic compaction., Allum. E Nuova Met. 33 (1964) 505.

[69] R.G. Buchheit, J.P. Moran, G.E. Stoner, Localized Corrosion Behavior of AIIoy 2090- The Role of Microstructural Heterogeneity, Corrosion. (1990) 610–617.

[70] K.S. Prasad, N.E. Prasad, A.A. Gokhale, Microstructure and Precipitate Characteristics of Aluminum-Lithium Alloys, Elsevier Inc., 2013. doi:10.1016/B978-0-12-401698-9.00004-5.

[71] J.G. Rinker, M. Marek, T.H.J. Sanders, Microstructure, Toughness and Stress Corrosion Cracking Behavior of Aluminum Alloy 2020, Mater. Sci. Eng. 64 (1984) 203–221.

[72] R.G. Buchheit, J.P. Moran, G.E. Stoner, Electrochemical Behavior of the T1 (Al2CuLi) Intermetallic Compound and its Role in Localized Corrosion of Al-2%Li-3%Cu Alloys, Corros. Sci. 50 (1994) 120–130.

[73] C. Luo, S.P. Albu, X. Zhou, Z. Sun, X. Zhang, Z. Tang, et al., Continuous and discontinuous localized corrosion of a 2xxx aluminium e copper e lithium alloy in sodium chloride solution, J. Alloys Compd. 658 (2016) 61–70. doi:10.1016/j.jallcom.2015.10.185.

[74] C. Kumai, J. Kusinski, G. Thomas, T.M. Devine, Influence of Aging at 200 C on the Corrosion Resistance of AI-Li and Al-Li-Cu Alloys *, Corrosion. 45 (1989) 294–302.

[75] J.F. Li, Z.Q. Zheng, N. Jiang, S.C. Li, Study on localized corrosion mechanism of 2195 Al-Li alloy in 4 . 0 % NaCl solution (pH 6 . 5) using a three-electrode coupling system, 410083 (2005) 192–196. doi:10.1002/maco.200403824.

[76] E.I. Meletis, Microstructure and Stress-Corrosion Cracking Relationshipin an AI-Li-Cu-Zr Alloy, in: Mater. Sci. Eng., 1987: pp. 235–245.

[77] E.I. Meletis, W. Huang, The role of the T1 phase in the pre-exposure and hydrogen embrittlement of A1-Li-Cu alloys, in: Mater. Sci. Engineeering, 1991: pp. 197–209.

[78] V. Proton, J. Alexis, E. Andrieu, J. Delfosse, A. Deschamps, F. De Geuser, et al., The influence of artificial ageing on the corrosion behaviour of a 2050 aluminium-copper-lithium alloy, Corros. Sci. 80 (2014) 494–502. doi:10.1016/j.corsci.2013.11.060.

[79] C. Hénon, S. Rouault, Comparison of corrosion performance and Mechanisms of AlCu alloys with and without Li addition, in: 13th Int. Conf. Alum. Alloy., 2012.

[80] B.J. Connolly, J.R. Scully, Corrosion cracking susceptibility in Al-Li-Cu alloys 2090 and 2096 as a function of isothermal aging time., Scr. Mater. 42 (2000) 1039–1045.

[81] R. Wernick, S. Sheasby, P.G. Pinner, The Surface Treatment and Finishing of Aluminium and

its alloys, 5th ed., ASM International, Ohio, 1987.

[82] R.G. King, Cleaning, in: Surf. Treat. Finish. Alum., 1988: pp. 13–25. doi:10.1016/B978-0-08-031138-8.50008-2.

[83] Z. Feng, Y. Liu, T. Hashimoto, G.E. Thompson, X. Zhou, P. Skeldon, Influence of surface pretreatments on the corrosion protection of sol-gel coated AA2024-T3 aluminium alloy, Surf. Interface Anal. 45 (2013) 1452–1456. doi:10.1002/sia.5216.

[84] I. V. Gordovskaya, M. Curioni, T. Hashimoto, J. Walton, G.E. Thompson, P. Skeldon, Characterization of 2024 T3 Aluminum Alloy after Rare Earth Desmutting, J. Electrochem. Soc. 163 (2016) C253–C259. doi:10.1149/2.0201606jes.

[85] L. Juffs, A.E. Hughes, S. Furman, P.J.K. Paterson, The use of macroscopic modelling of intermetallic phases in aluminium alloys in the study of ferricyanide accelerated chromate conversion coatings, Corros. Sci. 44 (2002) 1755–1781.

[86] J. Vander Kloet, A.W. Hassel, M. Stratmann, Effect of Pretreatment on the Intermetallics in Aluminum Alloy 2024-T3, Zeitschrift Für Phys. Chemie. 219 (2005) 1505–1518.

[87] D. Chidambaram, G.P. Halada, Infrared microspectroscopic studies on the pitting of AA2024-T3 induced by acetone degreasing, Surf. Interface Anal. 6375 (2001) 1056–1059.

[88] S. V Kagwade, C.R. Clayton, D. Chidambaram, G.P. Halada, Photochemical breakdown of acetone on copper Photochemical breakdown of acetone on copper, Electrochim. Acta. 46 (2001) 2337–2342. doi:10.1016/S0013-4686(01)00359-0.

[89] A.E. Hughes, R.J. Taylor, K.J.H. Nelson, B.R.W. Hinton, L. Wilson, Characterisation of surface preparation of alloy for conversion coating, Mater. Sci. Technol. 12 (1996) 928–936.

[90] S. Joshi, W.G. Fahrenholtz, M.J. O'Keefe, Electrochemical Characterization of Al 7075-T6 Surface Oxide After Alkaline Treatments, J. Electrochem. Soc. 158 (2011) C296–C301. doi:10.1149/1.3610404.

[91] S. Joshi, W.G. Fahrenholtz, M.J. OKeefe, Effect of alkaline cleaning and activation on aluminum alloy 7075-T6, Appl. Surf. Sci. 257 (2011) 1859–1863.

[92] E.V. Koroleva, G.E. Thompson, G. Hollrigl, M. Bloeck, Surface morphological changes of aluminium alloys in alkaline solution:, Corros. Sci. 41 (1999) 1475–1495. doi:10.1016/S0010-938X(98)00188-7.

[93] Y. Liu, M.A. Arenas, P. Skeldon, G.E. Thompson, H. Habazaki, K. Shimizu, et al., Generation of copper nanoparticles during alkaline etching of an Al–30at.%Cu alloy, Corros. Sci. 48 (2006) 1874–1884. doi:10.1016/j.corsci.2005.07.011.

[94] Y. Liu, M. a. Arenas, S.J. Garcia-Vergara, T. Hashimoto, P. Skeldon, G.E. Thompson, et al., Behaviour of copper during alkaline corrosion of Al–Cu alloys, Corros. Sci. 50 (2008) 1475–1480. doi:10.1016/j.corsci.2008.01.021.

[95] N. Dimitrov, J. a. Mann, M. Vukmirovic, K. Sieradzki, Dealloying of Al[sub 2]CuMg in Alkaline Media, J. Electrochem. Soc. 147 (2000) 3283. doi:10.1149/1.1393896.

[96] S. Joshi, W.G. Fahrenholtz, M.J. O'Keefe, Alkaline activation of Al 7075-T6 for deposition of cerium-based conversion coatings, Surf. Coatings Technol. 205 (2011) 4312–4319. doi:10.1016/j.surfcoat.2011.03.073.

[97] C.E. Moffitt, D.M. Wieliczka, H.K. Yasuda, An XPS study of the elemental enrichment on aluminum alloy surfaces from chemical cleaning, Surf. Coatings Technol. 137 (2001) 188–196. doi:10.1016/S0257-8972(00)01121-X.

[98] S.K. Toh, A.E. Hughes, D.G. Mcculloch, J. DuPlessis, A. Stonham, Characterization of non-Cr-based deoxidizers on Al alloy 7475-T7651, Surf. Interface Anal. 36 (2004) 1523–1532. doi:10.1002/sia.1938.

[99] K.J.H. Nelson, A.E. Hughes, R.J. Taylor, B.R.W. Hinton, L. Wilson, M. Henderson, Characterisation of aluminium alloys after HNO3/HF-NaOH-HNO3/HF pretreatment, Mater. Sci. Technol. 17 (2001) 1211–1221.

[100] J.D. Gorman, A.E. Hughes, D. Jamieson, P.J.K. Paterson, Oxide formation on aluminium alloys in boiling deionised water and NaCl , CeCl 3 and CrCl 3 solutions, Corros. Sci. 45 (2003) 1103–1124.

[101] F.J. Monteiro, M.A. Barbosa, D.H. Ross, D.R. Gabe, Pretreatments to Improve the Adhesion of Electrodeposits on Aluminium, Surf. Interface Anal. 17 (1991) 519–528.

[102] F.J. Monteiro, M.A. Barbosa, D.R. Gabe, D.H. Ross, Surface Pretreatments of Aluminium for Electroplating., Surf. Coat. Technol. 35 (1988) 321–331.

[103] A.E. Hughes, G. Theodossiou, S. Elliott, T.G. Harvey, P.R. Miller, J.D. Gorman, et al., Study of deoxidation of 2024-T3 with various acids, Mater. Sci. Technol. 17 (2001) 1642–1652.

[104] Y. Liu, M. a. Arenas, A. de Frutos, J. de Damborenea, A. Conde, P. Skeldon, et al., Influence of nitric acid pre-treatment on Al–Cu alloys, Electrochim. Acta. 53 (2008) 4454–4460. doi:10.1016/j.electacta.2008.01.026.

[105] B. Chambers, Etching of aluminum alloys by ferric ion, Met. Finish. 98 (2000) 26–29. doi:10.1016/S0026-0576(00)81492-0.

[106] A.E. Hughes, T.G. Harvey, T. Nikpour, T.H. Muster, S.G. Hardin, Non-chromate deoxidation of AA2024-T3 using Fe(III)– HF – HNO3, Surf. Interface Anal. 36 (2004) 15–23. doi:10.1002/sia.1998.

[107] a. E. Hughes, J.D. Gorman, P.R. Miller, B. a. Sexton, P.J.K. Paterson, R.J. Taylor, Development of cerium-based conversion coatings on 2024-T3 Al alloy after rare-earth desmutting, Surf. Interface Anal. 36 (2004) 290–303. doi:10.1002/sia.1652.

[108] P. Campestrini, H. Terryn, A. Hovestad, J.H.W. de Wit, Formation of a cerium-based conversion coating on AA2024 : relationship with the microstructure, Surf. Coat. Technol. 176 (2004) 365–381. doi:10.1016/S0257-8972.

[109] A.E. Hughes, K.J.H. Nelson, P.R. Miller, Desmutting of aluminium alloy 2024-T3 using rare earth electrolyte, Mater. Sci. Technol. 15 (1999) 1124–1132.

doi:10.1179/026708399101505167.

[110] D. Landolt, Corrosion and surface chemistry of metals, 1st ed. vo, EPFL Press, 2007. doi:10.1016/S1369-7021(07)70081-0.

[111] K. Ogle, Atomic emission spectroelectrochemistry: A new look at the corrosion, dissolution and passivation of complex materials, Corros. Mater. 37 (2012) 58–65.

[112] P. Marcus, Corrosion Mechanisms in Theory and Practice, Third Edition, 3rd ed., 2011. https://books.google.com/books?id=8Kq7xVUpYuUC&pgis=1.

[113] C. Gabrielli, M. Keddam, F. Minouflet-Laurent, K. Ogle, H. Perrot, Investigation of zinc chromatation. I - Application of QCM-ICP coupling, Electrochim. Acta. 48 (2003) 965–976. doi:10.1016/S0013-4686(02)00809-5.

[114] A.J. Bard, L.R. Faulkner, Electrochemical Methods : Fundamentals and Applications, 2nd ed., John Wiley & Sons, Inc., 2001.

[115] K. Ogle, J. Baeyens, J. Swiatowska, P. Volovitch, Atomic emission spectroelectrochemistry applied to dealloying phenomena: I. The formation and dissolution of residual copper films on stainless steel, Electrochim. Acta. 54 (2009) 5163–5170. doi:10.1016/j.electacta.2009.01.037.

[116] K. Ogle, S. Weber, Anodic Dissolution of 304 Stainless Steel Using Atomic Emission Spectroelectrochemistry, J. Electrochem. Soc. 147 (2000) 1770–1780. doi:10.1149/1.1393433.

[117] M. Serdechnova, P. Volovitch, K. Ogle, Surface & Coatings Technology Atomic emission spectroelectrochemistry study of the degradation mechanism of model high-temperature paint containing sacri fi cial aluminum particles, Surf. Coat. Technol. 206 (2012) 2133–2139. doi:10.1016/j.surfcoat.2011.09.044.

[118] M. Mokaddem, J. Tardelli, K. Ogle, E. Rocca, P. Volovitch, Atomic emission spectroelectrochemical investigation of the anodization of AA7050T74 aluminum alloy, Electrochem. Commun. 13 (2011) 42–45. doi:10.1016/j.elecom.2010.11.008.

[119] D. Mercier, Q. Van Overmeere, R. Santoro, J. Proost, In-situ optical emission spectrometry during galvanostatic aluminum anodising, Electrochim. Acta. 56 (2011) 1329–1336. doi:10.1016/j.electacta.2010.10.092.

[120] Q. Van Overmeere, D. Mercier, R. Santoro, J. Proost, In Situ Optical Emission Spectrometry during Porous Anodic Alumina Initiation and Growth in Phosphoric Acid, Electrochem. Solid-State Lett. 15 (2012) C1. doi:10.1149/2.009201esl.

[121] L. Rossrucker, A. Samaniego, J.-P. Grote, A.M. Mingers, C.A. Laska, N. Birbilis, et al., The pH Dependence of Magnesium Dissolution and Hydrogen Evolution during Anodic Polarization, J. Electrochem. Soc. 162 (2015) C333–C339. doi:10.1149/2.0621507jes.

[122] L. Hou, M. Raveggi, X.-B. Chen, W. Xu, K.J. Laws, Y. Wei, et al., Investigating the Passivity and Dissolution of a Corrosion Resistant Mg-33at.%Li Alloy in Aqueous Chloride Using Online ICP-MS, J. Electrochem. Soc. 163 (2016) C324–C329. doi:10.1149/2.0871606jes.

[123] C. Boss, K. Fredeen, Concepts, Instrumentation and Techniques in Inductively Coupled Plasma

Optical Emission Spectrometry, Third Edit, PerkinElmer, 2004. http://www.perkinelmer.co.uk/CMSResources/Images/44-159043GDE_Concepts-of-ICP-OES-Booklet.pdf.

[124] S. Lebouil, Etude et réalisation d'un couplage instrumental pour la mesure du dégagement d'hydrogène ne temps réel: apports des outils microfluidiques, Université Pierre et Marie Curie, 2013.

[125] M. Thompson, Handbook of Inductively Coupled Plasma Spectrometry, Second Edition, 1st ed., Springer US, 1989.

[126] V. Shkirskiy, P. Maciel, J. Deconinck, K. Ogle, On the time resolution of the atomic emission spectroelectrochemistry method, J. Electrochem. Soc. 163 (2016) 1–8.

[127] V. Shkirskiy, Corrosion Inhibition Of Galvanized Steel by LDH-inhibitor hybrids: Mechanism of Inhibitor Release and Corrosion Reactions, Pierre et Marie Curie, 2015.

[128] O. Gharbi, N. Birbilis, K. Ogle, In-Situ Monitoring of Alloy Dissolution and Residual Film Formation during the Pretreatment of Al-Alloy AA2024-T3, J. Electrochem. Soc. 163 (2016) C240–C251. doi:10.1149/2.1121605jes.

[129] B.C.R. Troconis, G.S. Frankel, Surface & Coatings Technology Effect of Roughness and Surface Topography on Adhesion of PVB to AA2024-T3 using the Blister Test, Surf. Coat. Technol. 236 (2013) 531–539. doi:10.1016/j.surfcoat.2013.10.046.

[130] S.J. Ketchum, S.R. Brown, Chromate conversion coatings of Aluminum Alloys, Met. Finish. 74 (1975) 37–41.

[131] C. Blanc, B. Lavelle, G. Mankowski, The role of precipitates enriched with copper on the susceptibility to pitting corrosion of the 2024 aluminium alloy, Corros. Sci. 39 (1997) 495–510. doi:10.1016/S0010-938X(97)86099-4.

[132] R.G. Buchheit, N. Birbilis, Electrochemical microscopy: An approach for understanding localized corrosion in microstructurally complex metallic alloys, Electrochim. Acta. 55 (2010) 7853–7859. doi:10.1016/j.electacta.2010.04.046.

[133] N. Birbilis, R.G. Buchheit, Electrochemical Characteristics of Intermetallic Phases in Aluminum Alloys, J. Electrochem. Soc. 152 (2005) B140–B151. doi:10.1149/1.1869984.

[134] M. Büchler, T. Watari, W.. Smyrl, Investigation of the initiation of localized corrosion on aluminum alloys by using fluorescence microscopy, Corros. Sci. 42 (2000) 1661–1668. doi:10.1016/S0010-938X(00)00020-2.

[135] L.C. Marsland, G.T. Burstein, Electroluminescence of aluminium during electropolishing in nitric acid, Electrochem. Commun. 2 (2000) 591–594. doi:10.1016/S1388-2481(00)00084-9.

[136] C.M. Rangel, T.I. Paiva, P.P. Da Luz, Conversion coating growth on 2024-T3 Al alloy. The effect of pre-treatments, Surf. Coatings Technol. 202 (2008) 3396–3402. doi:10.1016/j.surfcoat.2007.12.017.

[137] D. Chidambaram, C.R. Clayton, M.W. Kendig, G.P. Halada, Surface Pretreatments of

Aluminum Alloy AA2024-T3 and Formation of Chromate Conversion Coatings, J. Electrochem. Soc. 151 (2004) B605–B612. doi:10.1149/1.1806393.

[138] L. Li, A.L. Desouza, G.M. Swain, Effect of Deoxidation Pretreatment on the Corrosion Inhibition Provided by a Trivalent Chromium Process (TCP) Conversion Coating on AA2024-T3, J. Electrochem. Soc. 161 (2014) 246–253. doi:10.1149/2.031405jes.

[139] H. Habazaki, X. Zhou, K. Shimizu, P. Skeldon, G.E. Thompson, G.C. Wood, Mobility of copper ions in anodic alumina films, Electrochim. Acta. 42 (1997) 2627–2635. doi:10.1016/S0013-4686(96)00454-9.

[140] L. Jiang, P. Volovitch, M. Wolpers, K. Ogle, Activation and inhibition of Zn–Al and Zn–Al–Mg coatings on steel by nitrate in phosphoric acid solution, Corros. Sci. 60 (2012) 256–264.

[141] L. Jiang, M. Wolpers, P. Volovitch, K. Ogle, The degradation of phosphate conversion coatings by electrochemically generated hydroxide, Corros. Sci. 55 (2012) 76–89. doi:10.1016/j.corsci.2011.10.004.

[142] K. Ogle, A. Tomandl, N. Meddahi, M. Wolpers, The alkaline stability of phosphate coatings I: ICP atomic emission spectroelectrochemistry, Corros. Sci. 46 (2004) 979–995. doi:10.1016/S0010-938X(03)00182-3.

[143] F.H. Scholes, S.A. Furman, A.E. Hughes, T.A. Markley, Corrosion in artificial defects. I: Development of corrosion, Corros. Sci. 48 (2006) 1812–1826. doi:10.1016/j.corsci.2005.05.050.

[144] R.D. Armstrong, V.J. Braham, The mechanism of aluminium corrosion in alkaline solutions, Corros. Sci. 38 (1996) 1463–1471. doi:10.1016/0010-938X(96)00037-6.

[145] M. Mokaddem, P. Volovitch, F. Rechou, R. Oltra, K. Ogle, The anodic and cathodic dissolution of Al and Al–Cu–Mg alloy, Electrochim. Acta. 55 (2010) 3779–3786. doi:10.1016/j.electacta.2010.01.079.

[146] B.C.R. Troconis, G.S. Frankel, Effects of Pretreatments on the Adhesion of Acetoacetate to AA2024-T3 Using the Blister Test, Corrosion. 70 (2014) 483–495.

[147] T. Dursun, C. Soutis, Recent developments in advanced aircraft aluminium alloys, Mater. Des. 56 (2014) 862–871. doi:10.1016/j.matdes.2013.12.002.

[148] P. Lequeu, K.P. Smith, a. Daniélou, Aluminum-copper-lithium alloy 2050 developed for medium to thick plate, J. Mater. Eng. Perform. 19 (2010) 841–847. doi:10.1007/s11665-009-9554-z.

[149] R.J.H. Wanhill, Aerospace Applications of Aluminum-Lithium Alloys, Elsevier Inc., 2013. doi:10.1016/B978-0-12-401698-9.00015-X.

[150] N.L. Sukiman, X. Zhou, N. Birbilis, A.E. Hughes, J.M.C. Mol, S.J. Garcia, et al., Durability and Corrosion of Aluminium and Its Alloys: Overview, Property Space, Techniques and Developments, in: Alum. Alloy. - New Trends Fabr. Appl., 2012: pp. 47–97. doi:10.5772/3354.

[151] M. Guérin, E. Andrieu, G. Odemer, J. Alexis, C. Blanc, Effect of varying conditions of exposure to an aggressive medium on the corrosion behavior of the 2050 Al-Cu-Li alloy, Corros. Sci. 85

(2014) 455–470. doi:10.1016/j.corsci.2014.04.042.

[152] A. Buis, J. Schijve, Stress corrosion cracking behavior of Al-Li 2090-T83 in artificial seawater, Corrosion. 48 (1992) 898–909.

[153] J. Zhang, X. Zhao, Y. Zuo, J. Xiong, X. Zhang, Effect of Surface Pretreatment on Adhesive Properties of Aluminum Alloys, J. Mater. Sci. Technol. 24 (2008) 236–240.

[154] O. Lunder, B. Olsen, K. Nisancioglu, Pre-treatment of AA6060 aluminium alloy for adhesive bonding, Int. J. Adhes. Adhes. 22 (2002) 143–150. doi:10.1016/S0143-7496(01)00049-5.

[155] R.G. Buchheit, F.D. Wall, G.E. Stoner, J.P. Moran, Anodic dissolution-based mechanism for the rapid cracking, preexposure phenomenon demonstrated by aluminum-lithium-copper alloys, Corrosion. 51 (1995) 417–428. doi:10.5006/1.3293607.

[156] C.F. Baes, R.F. Mesmer, The thermodynamics of cation hydrolysis., Am. J. Sci. 281 (1981) 935–962. doi:10.2475/ajs.281.7.935.

[157] W. Zhang, G.S. Frankel, Localized Corrosion Growth Kinetics in AA2024 Alloys, (2002) 510–519. doi:10.1149/1.1513984.

[158] G. Critchlow, D. Brewis, Review of surface pretreatments for aluminium alloys, Int. J. Adhes. Adhes. 16 (1996) 255–275. http://www.sciencedirect.com/science/article/pii/S0143749696000140 (accessed February 14, 2014).

[159] N. Birbilis, R.G. Buchheit, D.L. Ho, M. Forsyth, Inhibition of AA2024-T3 on a Phase-by-Phase Basis Using an Environmentally Benign Inhibitor, Cerium Dibutyl Phosphate, Electrochem. Solid-State Lett. 8 (2005) C180–C183. doi:10.1149/1.2073672.

[160] H. Guan, R.G. Buchheit, Corrosion protection of aluminum alloy 2024-T3 by vanadate conversion coatings, Corrosion. 60 (2004) 284–296. doi:10.5006/1.3287733.

[161] J. Li, B. Hurley, R. Buchheit, Inhibition Performance Study of Vanadate on AA2024-T3 at High Temperature by SEM, FIB, Raman and XPS, J. Electrochem. Soc. 162 (2015) C219–C227. doi:10.1149/2.0371506jes.

[162] V. Moutarlier, M.P. Gigandet, B. Normand, J. Pagetti, EIS characterisation of anodic films formed on 2024 aluminium alloy, in sulphuric acid containing molybdate or permanganate species, Corros. Sci. 47 (2005) 937–951. doi:10.1016/j.corsci.2004.06.019.

[163] R.G. Buchheit, M.D. Bode, G.E. Stoner, Corrosion-Resistant, Chromate-Free Talc Coatings for Aluminum*, Corros. Sci. 50 (1993) 205–214.

[164] P. Visser, Y. Liu, X. Zhou, T. Hashimoto, G.E. Thompson, S.B. Lyon, et al., The Corrosion Protection of AA2024-T3 Aluminium Alloy by Leaching of Lithium-Containing Salts from Organic Coatings, Faraday Discuss. 180 (2015) 1–16. doi:10.1039/C4FD00237G.

[165] P. Visser, Y. Liu, H. Terryn, J.M.C. Mol, Lithium salts as leachable corrosion inhibitors and potential replacement for hexavalent chromium in organic coatings for the protection of aluminum alloys, J. Coatings Technol. Res. 13 (2016) 557–566. doi:10.1007/s11998-016-9784-

6.

[166] Y. Liu, P. Visser, X. Zhou, S.B. Lyon, T. Hashimoto, M. Curioni, et al., Protective Film Formation on AA2024-T3 Aluminum Alloy by Leaching of Lithium Carbonate from an Organic Coating, J. Electrochem. Soc. 163 (2016) C45–C53. doi:10.1149/2.0021603jes.

[167] C.A. Drewien, M.O. Eatough, D.R. Tallant, C.R. Hills, R.G. Buchheit, Lithium-aluminum-carbonate-hydroxide hydrate coatings on aluminum alloys : Composition , structure , and processing bath chemistry, J. Mater. Res. 11 (1996) 1507–1513.

[168] C.M. Rangel, M.A. Travassos, Li-based conversion coatings on aluminium: An electrochemical study of coating formation and growth, Surf. Coatings Technol. 200 (2006) 5823–5828. doi:10.1016/j.surfcoat.2005.08.145.

[169] C.M. Rangel, M.A. Travassos, the Passivation of Aluminium in Lithium Carbonate / Bicarbonate Solutions, Corros. Sci. 33 (1992) 327–343.

[170] J. Gui, T.M. Devine, Influence of lithium on the corrosion of aluminum, Scr. Metall. 21 (1987) 853–857. doi:10.1016/0036-9748(87)90336-X.

[171] G.R. Williams, D. O'Hare, A kinetic study of the intercalation of lithium salts into Al(OH)3., J. Phys. Chem. B. 110 (2006) 10619–29. doi:10.1021/jp057130k.

[172] V.P. Isupov, Intercalation Compounds Of Aluminum Hydroxide, J. Struct. Chem. 40 (1999) 672–685.

[173] S.H. Hyun, H.J. Cho, J.J. Lee, Manufacturing Method Of Highly Pure Alpha-LiAlO2, 2008. doi:US 2010/0311130 Al.

[174] J.T. Huneke, R.E. Cramer, R. Alvarez, S.A. El-Swaify, The Identification of Gibbsite and Bayerite by Laser Raman Spectroscopy, Soil Sci. Soc. Am. J. 44 (1980) 131–134. doi:10.2136/sssaj1980.03615995004400010027x.

[175] M. Smirnov, R. Baddour-Hadjean, Li intercalation in TiO2 anatase: Raman spectroscopy and lattice dynamic studies, J. Chem. Phys. 121 (2004) 2348–2355. doi:10.1063/1.1767993.

[176] T. Kloprogge, R.L. Frost, M. Al-, Infrared and Raman study of interlayer Mg / Alhydrotalcite, Am. Mineral. 87 (2002) 623–629.

[177] J.L. White, Role of Carbonate in Aluminum Hydroxide Gel Established by Raman and Ir Analysis, J. Pharm. Sci. 64 (1975) 468–469.

[178] S.F. Parker, K. Refson, R.I. Bewley, G. Dent, Assignment of the vibrational spectra of lithium hydroxide monohydrate, LiOH.H 2O, J. Chem. Phys. 134 (2011) 1–8. doi:10.1063/1.3553812.

[179] S.D. Ross, Inorganic Infrared and Raman Spectra, McGraw-Hill Book Company, London, 1972.

[180] P.K. Dutta, M. Puri, Anlon Exchange in Lithium Aluminate Hydroxides, J. Phys. Chem. 93 (1989) 376–381. doi:10.1021/j100338a072.

[181] S.. Gupta, D.D.. Agarwal, S.. Banerjee, Lithium aluminium layered double hydroxides: Synthesis and application in poly (vinyl chloride), Int. J. Polym. Mater. Polym. Biomater. 61 (2012) 985–998. doi:10.1080/00914037.2011.610067.

[182] J.C.S. Fernandes, M.G.S. Ferreira, Effect of carbonate and lithium ions on the corrosion performance of pure aluminium, Electrochim. Acta. 37 (1992) 2659–2661. doi:10.1016/0013-4686(92)87066-9.

APPENDIX

X-ray pattern of pure Al

PDF Card No.: 00-004-0787 Quality:S

Sub-File Name:	Inorganic, Mineral, Alloy&Metal, Common Phase, Educational Pattern, Explosive...				
Formula:	Al				
Name:	Aluminum, syn				I/Ic (RIR)= 3.62
Crystal System:	Cubic	Space Group:	Fm-3m(225)	Dmeas:	
Cell Parameters:	a= 4.0490	b=	4.0490	c=	4.0490
	Alpha= 90.000	Beta=	90.000	Gamma=	90.000
	Volume= 66.381	Z=	4		
Reference:	Swanson, Tatge., I(1953)11.				
Radiation:	CuKa1	Wavelength=	1.54056		
2Theta range:	38.47 - 137.46				

Database comments: Color: Light gray metallic. Temperature of data collection: Pattern taken at 25 C. Sample source or locality: The material used for the NBS sample was a melting point standardsample of aluminum prepared at NBS, Gaithersburg, Maryland, USA. General Comments: Mineral species of doubtful validity, ¥ITAm. Mineral.¥RG, ¥BF65¥RG205 (1980).

Relative Intensity

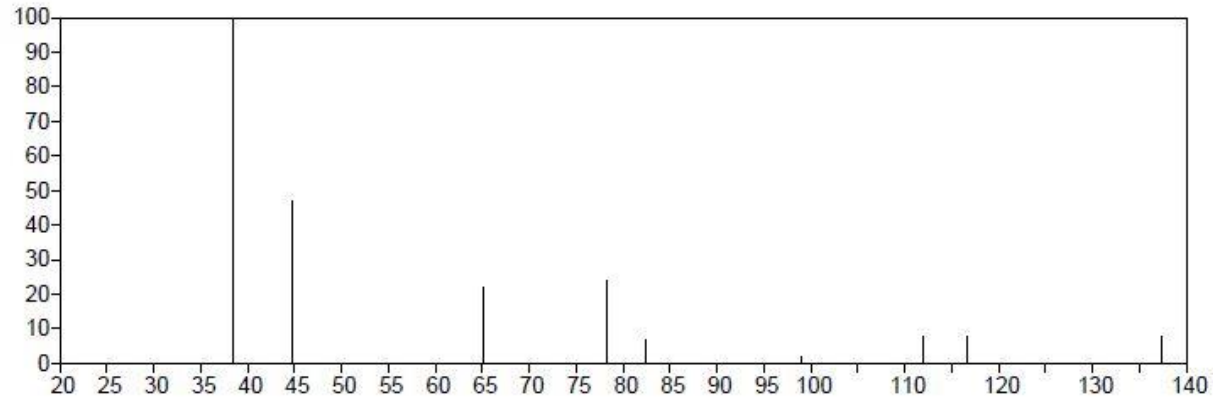

No.	2Theta	d-Value	Intensity	h	k	l	No.	2Theta	d-Value	Intensity	h	k	l
1	38.47	2.338	100.0	1	1	1							
2	44.74	2.024	47.0	2	0	0							
3	65.13	1.431	22.0	2	2	0							
4	78.23	1.221	24.0	3	1	1							
5	82.44	1.169	7.0	2	2	2							
6	99.08	1.012	2.0	4	0	0							
7	112.04	0.929	8.0	3	3	1							
8	116.57	0.905	8.0	4	2	0							
9	137.46	0.827	8.0	4	2	2							

Note: 2theta are calculated with wavelength = 1.54059

2016-oct.-14 20:07:37 Page-1/1

X –ray pattern of Al_2O_3

PDF Card No.: 00-009-0440 Quality:O

Sub-File Name:	Inorganic, Alloy&Metal,				
Formula:	Al2 O3				
Name:	Aluminum Oxide				I/Ic (RIR)= ---
Crystal System:	Monoclinic	Space Group:	A2/m(12)	Dmeas:	
Cell Parameters:	a= 5.7000	b=	2.9200	c=	11.8998
	Alpha= 90.000	Beta=	104.496	Gamma=	90.000
	Volume= 191.755	Z=	4		
Reference:	Stumpf et al., 42(1950)1398.				
Radiation:	CuKa1	Wavelength=	1.5405		
2Theta range:	16.87 - 128.01				

Database comments: Sample source or locality: $GB alumina trihydrate heated 1 hour at 1100 C in moving dry air.

Relative Intensity

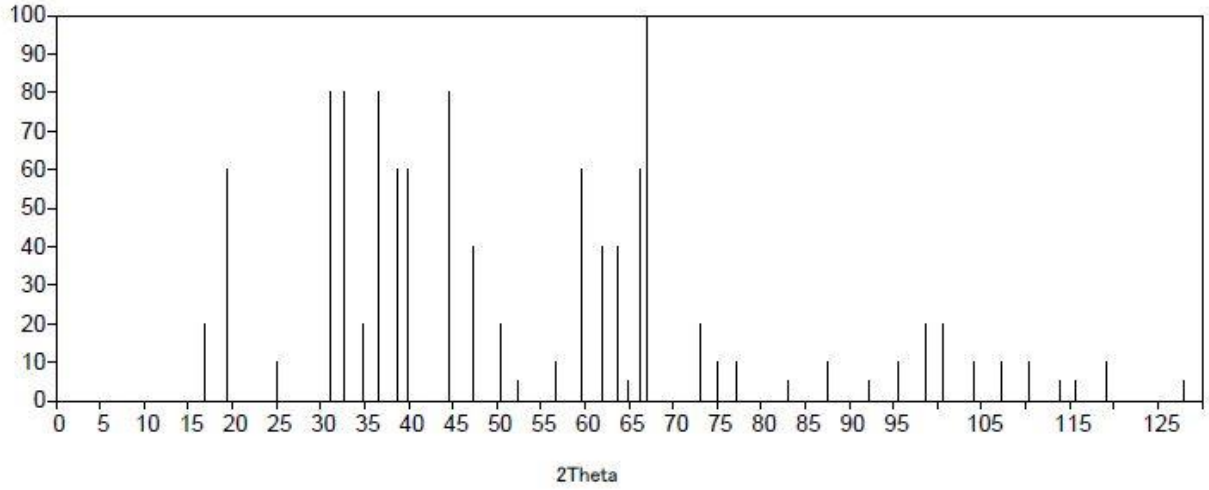

No.	2Theta	d-Value	Intensity	h	k	l	No.	2Theta	d-Value	Intensity	h	k	l
1	16.87	5.250	20.0				21	73.13	1.293	20.0	-2	2	2
2	19.49	4.550	60.0	-1	0	2	22	75.02	1.265	10.0	-4	1	1
3	24.99	3.560	10.0	1	0	2	23	77.18	1.235	10.0	1	2	4
4	31.14	2.870	80.0	-1	0	4	24	83.13	1.161	5.0	0	2	6
5	32.66	2.740	80.0	2	0	0	25	87.59	1.113	10.0	4	1	3
6	34.74	2.580	20.0	-1	1	1	26	92.20	1.069	5.0	4	1	
7	36.65	2.450	80.0	1	1	1	27	95.46	1.041	10.0	-1	2	8
8	38.70	2.325	60.0	0	1	3	28	98.74	1.015	20.0	-4	1	9
9	39.86	2.260	60.0	-1	1	3	29	100.62	1.001	20.0	2	1	9
10	44.60	2.030	80.0	1	1	3	30	104.08	0.977	10.0	1	2	8
11	47.31	1.920	40.0	0	0	6	31	107.20	0.957	10.0	-1	3	1
12	50.37	1.810	20.0	0	1	5	32	110.41	0.938	10.0	-1	3	3
13	52.39	1.745	5.0	0	1		33	113.90	0.919	5.0	6	0	0
14	56.59	1.625	10.0	1	1	5	34	115.66	0.910	5.0	-2	3	3
15	59.60	1.550	60.0	1	1		35	119.22	0.893	10.0	-5	2	4
16	62.03	1.495	40.0	3	1	1	36	128.01	0.857	5.0	-5	2	
17	63.64	1.461	40.0	0	2	0							
18	64.93	1.435	5.0	0	1	7							
19	66.23	1.410	60.0	1	2	0							
20	67.03	1.395	100.0	2	1	5							

Note: 2theta are calculated with wavelength = 1.54059

2016-oct.-14 20:08:42 Page-1/1

Original X-ray pattern of figure 49

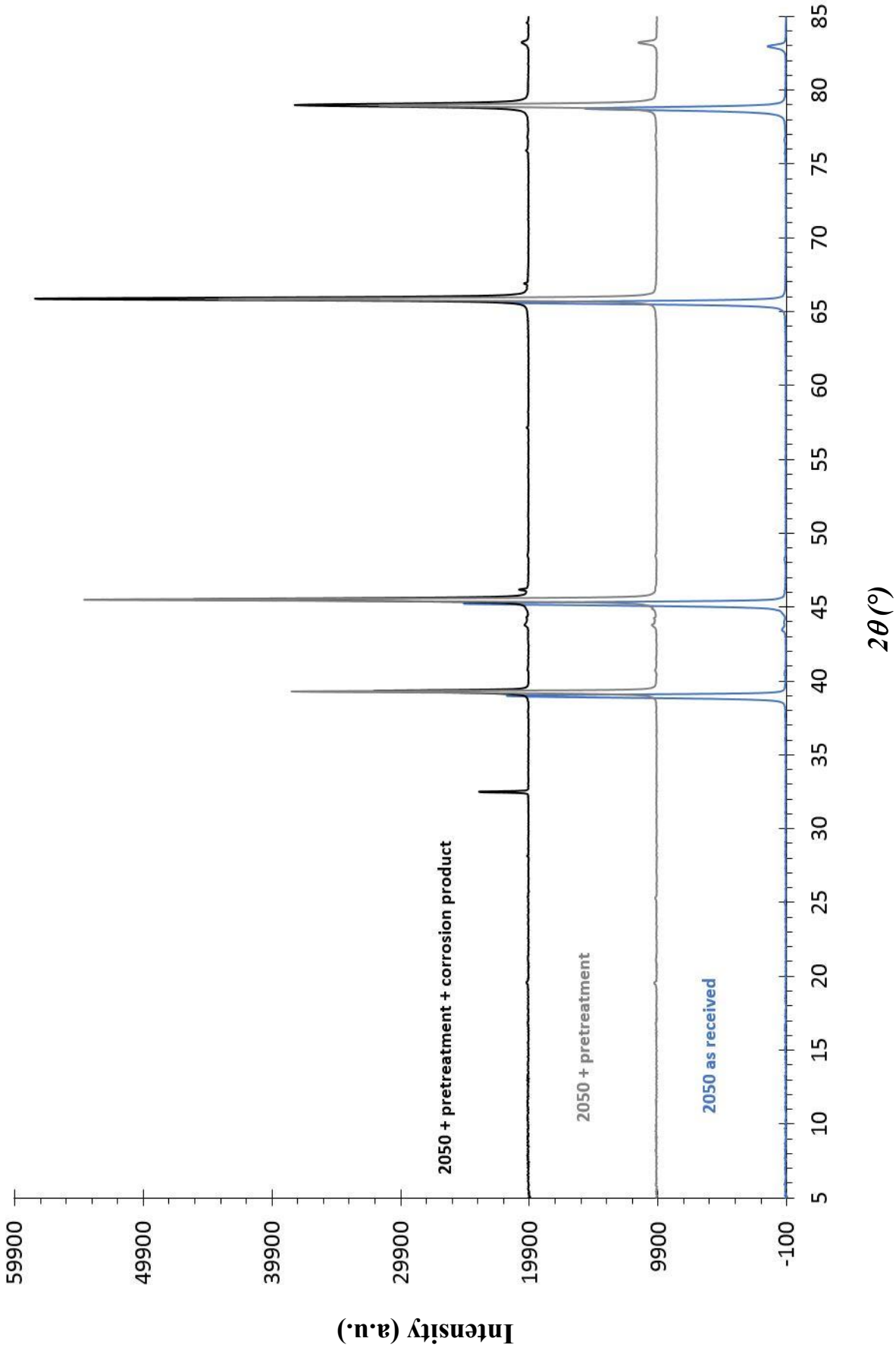

LIST OF PUBLICATIONS & CONFERENCES

List of publications

- **O. Gharbi**, N. Birbilis, K. Ogle, "*In-situ* monitoring of alloy dissolution and residual film formation during the pretreatment of Al-alloy AA2024-T3" J. Electrochem. Soc. 2016 volume 163, issue 5, C240-C251
- V. Shkirskiy, A.D. King, **O. Gharbi**, P. Volovitch, J.R. Scully, K. Ogle, and N. Birbilis – « Revisiting the Electrochemical Impedance Spectroscopy of Magnesium with Online Inductively Coupled Plasma Atomic Emission Spectroscopy », ChemPhysChem, 16(3), 2015, p. 536-539
- S. Lebouil, **O. Gharbi**, P. Volovitch, K. Ogle – « Mg Dissolution in Phosphate and Chloride Electrolytes: Insight into the Mechanism of the Negative Difference Effect », Corrosion, 71, 2015, p. 234-241
- S. Thomas, **O. Gharbi,** S.H. Salleh, P. Volovitch, K. Ogle, K. Vankatesan, N. Birbilis « On the effect of Fe concentration on Mg dissolution and activation studied using atomic emission spectroelectrochemistry and scanning electrochemical microscopy », Electrochimica Acta, 210, 2016, P. 271-284
- **O. Gharbi**, N. Birbilis, K. Ogle, "On-line reactivity measurement of Al-Li alloy AA2050-T3 during a surface pretreatment sequence using atomic emission spectroelectrochemistry" submitted to Electrochimica Acta

Conferences

Oral presentations:

- CEFRACOR **O. Gharbi,** K. Ogle « Analyse *in-situ* de la réactivité de l'alliage 2024-T3 durant les prétraitements » **Paris, France - June 2014**
- ECS Meeting**:** K. Ogle**, O. Gharbi** (presented by K. Ogle) **(Keynote) «** The Pretreatment of 2000 Series Al Alloy: *In Situ* Measurement of the Selective Dissolution & Film Formation » **Phoenix, Arizona, USA - October 2015**
- NACE CORROSION 2016: **O. Gharbi**, K. Ogle, N. Birbilis "*In situ* monitoring of dissolution and residual film formation during the pretreatment of Al alloys", **Vancouver, Canada - March 2016**
- Gordon Research Seminar 2016: **O. Gharbi**, K. Ogle, N. Birbilis - **New London, New Hampshire, USA - July 2016**

Poster sessions

- ASST 2015 (Aluminum Surface Science and Technology)**: O. Gharbi**, K. Ogle, « *In-situ* monitoring of alloy dissolution and residual film formation during the pretreatment of Al-alloy **» Madeira, Portugal - May 2015.**
- Gordon Research Seminar & Gordon Research Conference 2016: **O. Gharbi**, K. Ogle, N. Birbilis - **New London, New Hampshire, USA - July 2016**
- GD-days 2016: **O. Gharbi**, K. Ogle, N. Birbilis "On-line measurement of the reactivity of Al-Li alloy during a surface pretreatment sequence », **Synchroton Soleil, Orsay, France – September 2016.**